2017

Redox-Active Solid State Materials and its Biomedical and Biosensing Applications

Ankur Gupta
University of Central Florida

REDOX-ACTIVE SOLID STATE MATERIALS AND ITS BIOMEDICAL AND BIOSENSING APPLICATION

by

ANKUR GUPTA
Bachelor of Technology, Malaviya National Institute of Technology Jaipur, India, 2009
Master of Technology, Indian Institute of Technology Kanpur, India, 2011

A dissertation submitted in partial fulfillment of the requirements
for the degree of Doctor of Philosophy in Materials Science and Engineering
in the Department of Materials Science and Engineering
in the College of Engineering and Computer Science
at the University of Central Florida
Orlando, Florida, USA

Spring Term
2017

Major Professor: Sudipta Seal

ABSTRACT

Reactive oxygen species (ROS) are byproducts of physiological processes in human body, and strengthened production of ROS is known to cause acute conditions such as inflammation, aging, Alzheimer's disease, melanoma and ovarian cancer, fibrosis and multiple sclerosis. Therefore, early detection of ROS at nanomolar concentration (at cellular level) and developing more potent antioxidants is essential for regular health monitoring. As an example, ROS are also responsible for inflammation reactions at orthopedic implants-tissue interface triggered by wear debris. Inflammation induced by ROS results in revision surgery. Coatings of redox-active materials exhibiting antioxidant properties on implants have potential to mitigate the inflammation and delay the need of revision surgery. This dissertation focus on developing advanced functional nanomaterials by tailoring the surface chemistry of existing materials. Surface chemistry of materials can be altered by introducing surface and edge defects in the lattice structure Three materials system doped cerium oxide nanoparticles (d-CNPs), cerium oxide thin films (CeO_x) and molybdenum disulfide (MoS_2) nanoparticles, have been studied for its surface and edge contributions in potential biomedical and biosensing applications. Surface (d-CNPs and CeO_x thin films) and edge chemistry (MoS_2) have been tailored to understand its role and specific response.

Surface Ce^{3+}/Ce^{4+} oxidation state in CNPs controls the bio-catalytic activity. Higher superoxide dismutase (SOD) is demonstrated by high Ce^{3+}/Ce^{4+} oxidation state. On the other hand, improved catalase mimetic activity is observed for low Ce^{3+}/Ce^{4+} CNPs. Different CNPs preparation results in different Ce^{3+} to Ce^{4+} ratio, particle size, surface coating, and agglomeration, thus significantly varying the antioxidant properties of CNPs.

In the first section of the dissertation, sustainable one-step room temperature synthesis of rare earth element (La, Sm, and Er) d-CNPs have been developed to effectively control the Ce^{3+} to Ce^{4+} ratio for specific biological application. Substitution of Ce^{4+} ions by trivalent dopants from ceria lattice increases the oxygen vacancies and density of catalytic sites. Uniform distribution of trivalent dopant in ceria lattice confirmed by EFTEM is attributed to enhanced SOD mimetic activity, ROS scavenging and tuning surface Ce^{3+}/Ce^{4+} oxidation state in CNPs. Surface chemistry of redox-active cerium oxide coating on orthopedic implants also plays a vital role in scavenging ROS and mitigating inflammation. Thus, surface chemistry of CeOx thin films deposited by atomic layer deposited (ALD), have also been tailored by controlling the film thickness. CeO_x film of 2 nm thickness has high Ce^{3+}/Ce^{4+} (ratio 1) whereas higher thickness films (6-33 nm) have lower Ce^{3+}/Ce^{4+} (ratio 0.30-0.37). These films have been further tested for catalase mimetic activity and hydrogen peroxide (H_2O_2) detection. Sensor selectivity is always a key issue. Most often, ascorbic acid found in the biological system, interfere in the electrochemical detection of H_2O_2 resulting in selectivity issue, thus protective Nafion layer is required to prevent cerium oxide-ascorbic acid interaction.

To improve the selectivity of electrochemical sensors, Sulfur-deficient redox-active MoS_2 have been utilized for electrochemical detection of pharmaceutically relevant chemical species. S-deficient MoS_2 nanoparticles have been prepared by liquid exfoliation method to increase Mo-edge density and tested as sensing materials for detection of pharmaceutically relevant H_2O_2, hypochlorous acid (HOCl) and reactive nitrogen (NO*) species. The addition of ascorbic acid and uric acid have shown no interference during H_2O_2 detection. Change in S to Mo ratio have been studied using x-

ray photoelectron spectroscopy. Density functional theory (DFT) have been employed to understand the detection mechanism and size-dependent sensitivity of MoS_2. DFT study further reveals the role of S-deficiency and Mo- and S-edges in the higher catalytic activity of 5-7 nm MoS_2 particles.

Through these studies, the importance of defects in nanomaterials and their exotic properties at the nanoscale have been demonstrated. Understanding developed from these studies have provided the framework to develop more advanced functional nanomaterials for biomedical and biosensing applications.

Dedicated to…..

My ever loving Parents for support

Rahul - brother and my best friend for countless smiling moments

Dr. Kantesh Balani and Dr. A.K. Bhargava for pushing me into the unknown territory of research.

ACKNOWLEDGMENTS

It gives me immense pleasure to express my profound gratitude to my dissertation supervisor, Prof. Sudipta Seal, for his motivation, support and excellent supervision with absolute appreciations throughout the course of doctoral studies at UCF. His confidence in me was a constant source of inspiration for all the success I have made. His hardworking nature, multiple tasking capabilities has amazed me and gave the meaningful ways to deal with the life.

I am also thankful to the dissertation committee members, Dr. Lei Zhai, Dr. Alfons Schulte, Dr. Yajie Dong and Dr. Hyoung Jin Cho for valuable and constructive discussion and providing their valuable time to this dissertation.

I am thankful to Dr. Soumen Das, Dr. Tamil Selvan Sakthival, Dr. Shashank Saraf and Swetha Barkam for the conceptual discussions and instrumentation. It was a pleasure working with Craig J. Neal, Takat B. Rawal, Dr. Talat Rahman, Dr. Seetha Raghvan, Dr. Gregory Freihofer, David ward, Dr. Cheng Zhang, Dr. Arvind Agarwal, Pranjal Nautiyal, Richard J. Murdock, Dr. Shawn A. Putnam, Dr. Ramandeep Rattan, Dr. Peter Brenneisen, Aadithya Jayaranjan and Nileshi Saraf.

I express my sincere appreciation to Materials Characterization Facility (MCF) at UCF and it’s research engineer Kirk Scammon, Mikhail Klimov and Matthew Schneider for offering the characterization facilities required and helping at different stage of instrument handling, respectively. I also owe my thanks to Dr. Yajie Dong for extending ALD system usage for my dissertation work. This dissertation work was not possible without the administrative support provided by Karen, Angie, Kari, Sandra and Pamela from AMPAC, MSE.

I convey my thanks to the Journal of Materials Chemistry B (Royal Society of Chemistry) and 2D Materials (Institute of Physics) for publishing research work carried out during this dissertation and granting the permission to use them in this dissertation.

This research has been supported by National Science Foundation (NSF), National Institutes of Health (NIH), National Aeronautics and Space Administration (NASA). Florida High Tech Corridor (FHTC), Garmor, Inc., Air Products and Sanofi Pasteur-Vaxdesign. I am thankful for the financial support through the award, fellowship and travel grants during my doctoral studies from University of Central Florida (Graduate Presentation Fellowship, Graduate Student Research Scholarship) and societies (ASM-TSS Student Board Member, AVS Dorothy M. and Earl S. Hoffman Travel Grant).

I am thankful to Rohit, Haider, Ashish, Sheethal, Abhishek, Nileshi, Anna and Addithya for being there as a family and giving me lots of cheerable moments. I enjoyed a fantastic and vibrant campus life throughout my stay. Thanks to Saumen Da and Tamil for being there like elder brother and guided me throughout my stay and helped me whenever I needed.

Most of all, I want to covey my greatest gratitude, respect and appreciation to my parents, brother (Rahul), and previous advisors (Dr. Kantesh Balani and Dr. A.K. Bhargava) who always supported me through all the ups and downs in my life and made it possible for me to pursue this career. I give them a glowing tribute.

TABLE OF CONTENT

LIST OF FIGURES

LIST OF TABLES

LIST OF ABBREVIATIONS

ALD	Atomic layer deposition
CA	Chronoamperometry
$Ce(iPrCp)_3$	Tris(i-propylcyclopentadienyl)cerium
CNPs	Cerium oxide nanoparticles
CV	Cyclic voltammetry
DFT	Density functional theory
DLS	Dynamic light scattering
DMF	Dimethylformamide
EELS	Electron energy loss spectroscopy
EFTEM	Energy filtered transmission electron microscopy
FTIR	Fourier transform infrared spectroscopy
H2DCFDA	2',7'-dichlorodihydrofluorescein diacetate
HRTEM	High resolution transmission electron microscope
LVPD	Low vapor pressure delivery
MTT	Thiazoyl blue tetrazolium bromide
PAN	Polyacrylonitrile
RBS	Rutherford back scattering
ROS	Reactive oxygen species
SEM	Scanning electron microscope
SOD	Superoxide dismutase
TGC	Thin glassy carbon
UV-Vis	Ultraviolet visible spectroscopy

XPS	X-ray photoelectron spectroscopy
XRD	X-ray diffraction
XRR	X-ray reflectivity

CHAPTER ONE: INTRODUCTION AND LITERATURE REVIEW

1.1 Free radicals in biological system

Reactive oxygen species (ROS) or pro-oxidants are by-products of biochemical reaction mainly in mitochondria, a powerhouse of the human body. In common, ROS have been divided into two parts classes, i.e. oxygen-derived free radicals (superoxide, hydroxyl radical, nitric oxide) and non-radical oxygen derivatives of high reactivity such as singlet oxygen, hydrogen peroxide, peroxynitrite, hypochlorite [1, 2], where free radicals being more reactive due to their paramagnetic behavior. Figure 1 shows the formation and transaction of various ROS in a biological system. These ROS play both, positive and negative role in the body. ROS act as a signal transducer at low concentrations, whereas at high concentration leads to a variety of disorders such as Alzheimer's disease, ageing, fibrosis, inflammation, cardiovascular diseases, infertility, diabetes, multiple sclerosis etc.[3]. Reactive nitrogen species cause mitochondrial fragmentation and neuronal cell death [4]. Concentrations of these ROS are maintained by antioxidants to prevent it exceeding the beneficial level in the human body (Figure 2). The main source of antioxidants to the human body are fruits and vegetables rich in vitamins, necessary to produce enzymes [5]. Thus, constant production and supply of antioxidants are essential for the good health. When oxygen atom loses electrons from its outer shell, free radicals generate which are very reactive in nature. To complete its electronic configuration, it acquires electron from the cell membrane/molecules. This process initiates the chain reaction and leads to the erosion of the cell membrane, thus creates physiological conditions. To circumvent such conditions, antioxidants donate their electrons to free radicals to achieve stable configuration (Figure 2). In most of the cases,

free radical-antioxidant equilibrium is maintained. However, when this equilibrium is disturbed, production of free radicals strengthen and result in various disorders mentioned above. In such cases, antioxidants are supplied externally in the form of medication to reestablish the equilibrium.

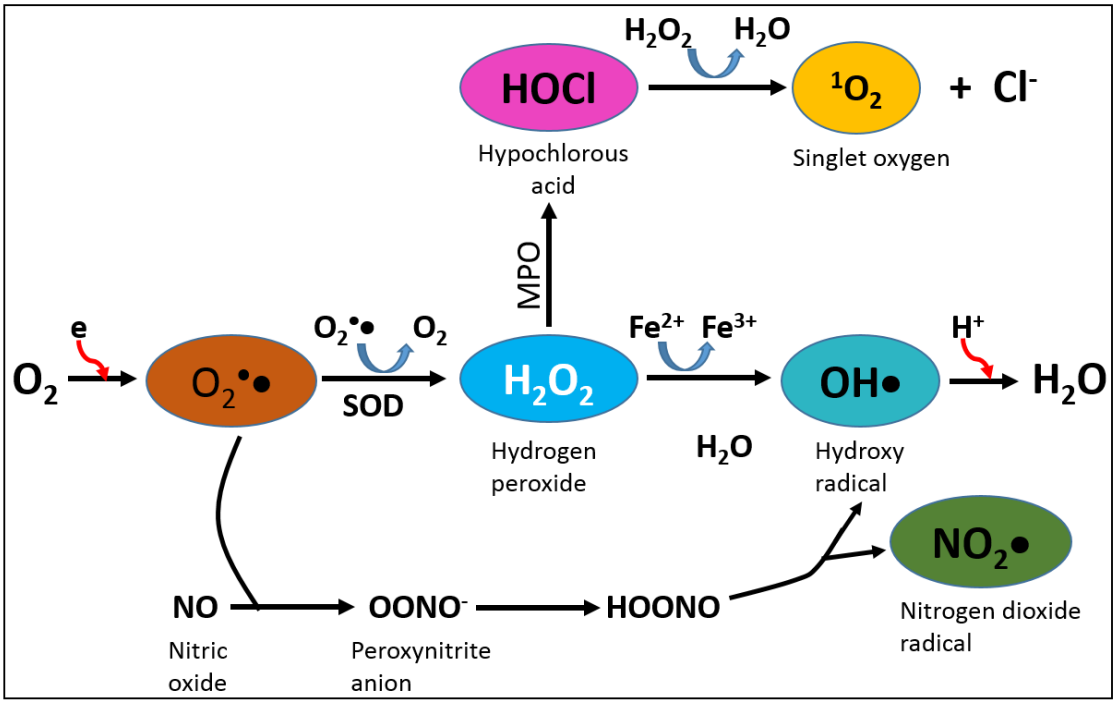

Figure 1: Production mechanism of free radicals in human cells.

Antioxidants supplied to female mice from green tea reduced the breast tumor size by 60% [5]. Another study has reported the use of flavonoid-mediated presenilin-1 phosphorylation as an antioxidant to decreases β-amyloid production, responsible for Alzheimer's disease [6]. Large scale human participant study on 87245 females nurses has resulted in a reduction of coronary disease.[7]. Participants were given vitamin E regularly and their health was monstered over right years. This study further emphasizes the role of supplement antioxidants to suppress the detrimental role of reactive oxygen species.

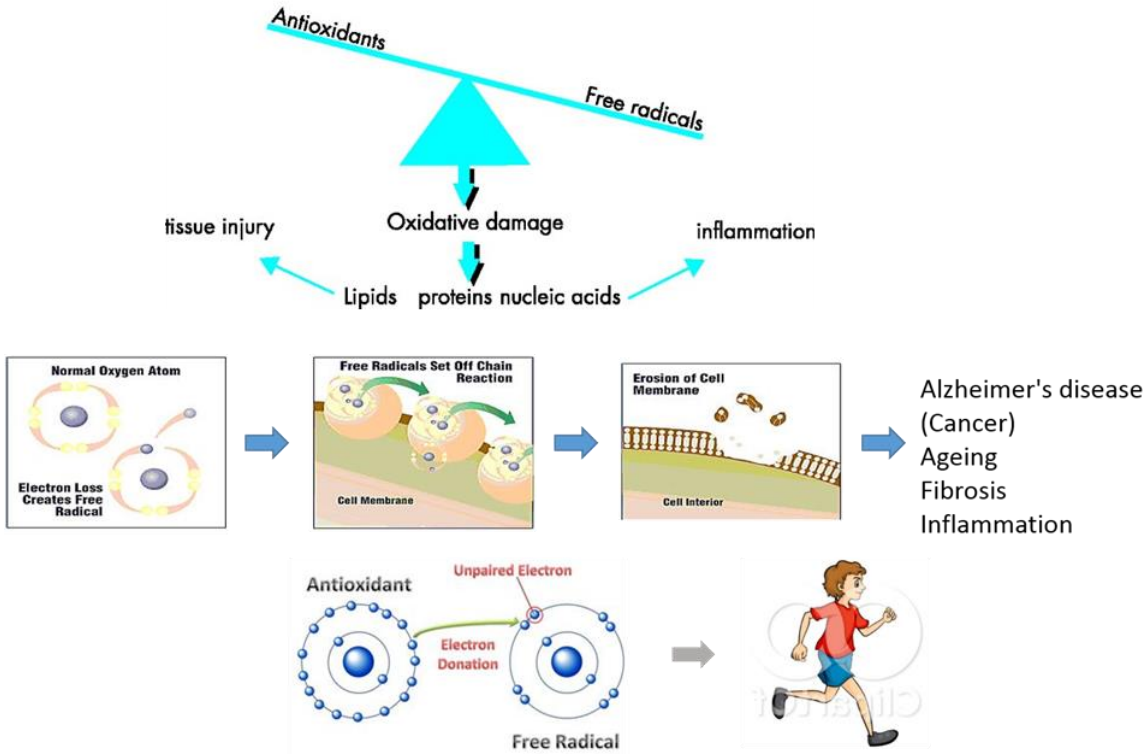

Figure 2: Effect of antioxidants-free radicals equilibrium disruption on cells and mechanism of addressing these challenges by antioxidants.

1.2 Generation of ROS

Ionizing radiation is the most important reason for the formation of ROS. Upon the interaction of ionizing radiation, water molecule ionizes and form H_2O^+. Ionized water molecule further reacts with H_2O and form hydroxyl radicals (OH*) and H_3O^+. Excited water molecules also dissociate into H*and OH*. These water radiolysis products (H*, OH* and e^-) react with oxygen and form hydrogen peroxide (H_2O_2), $O_2^{\bullet}$ and $HO_2^{\bullet}$ [1].

$$H_2O \xrightarrow{radiation} H_2O^{\bullet} \quad (1)$$

$$H_2O \rightarrow H_2O^+ + e^- \quad (2)$$

$$H_2O^{\bullet} \rightarrow H^{\bullet} + OH^{\bullet} \quad (3)$$

$$H_2O^+ + H_2O \rightarrow H_3O^+ + OH^{\bullet} \quad (4)$$

H_2O_2 formed as reaction product reacts with chloride ion (Cl^-). The reaction product of H_2O_2 and Cl^- form hypochlorous acid (HOCl) (equation 5). HOCl is a powerful oxidant and strong oxidizer and reacts with O^{2-} to produce hydroxyl radicals (OH^*).

$$H2O2 + Cl^- \xrightarrow{MPO} HOCl + OH^- \quad (5)$$

It is well known that under ultraviolet (UV) radiation exposure, an oxygen molecule (O_2) dissociate and produce ozone (O_3) (equation 6). Exposure of UV to H_2O_2 also produce OH* (equation 7).

$$O_2 \xrightarrow{UV} 2O \xrightarrow{O2} O_3 \quad (6)$$

$$H_2O_2 \xrightarrow{UV} 2OH^{\bullet} \quad (7)$$

The formed ROS also react with each other and form new species. Examples of few reaction are shown in equation (8-11).

$$O_2^{\cdot-} + O_2^{\cdot-} + 2H^+ \rightarrow O_2 + H_2O_2 \quad (8)$$

$$O_2^{\cdot-} + NO^{\bullet} \rightarrow ONOO^- \quad (9)$$

$$H_2O_2 + Fe^{2+} \rightarrow Fe^{3+} + OH^* + OH^- \quad (10)$$

$$Fe^{3+} + O_2^{\cdot-} \rightarrow Fe^{2+} + O_2 \quad (11)$$

Several enzymes and coenzymes also react with O2 and form superoxide radicals. Name of the few enzymes is: aldehyde oxidase, galactose oxidase, peroxidase, xanthine oxidase, NADPH: cytochrome c oxidase, anthranilate hydroxylase, diamine oxidase, nitric oxide synthase. The reaction between NADPH and O_2 is shown in equation 12.

$$NADPH + 2O_2 \rightarrow NADP^+ + H^+ + O_2^{\cdot-} \quad (12)$$

Free radicals are also generated in the medicines from over exposure to the light and other chemicals reactions. As a result, drugs have limited shelf life and kept in under strict storage conditions.

1.3 Methods of monitoring ROS

It is clearly evident from the discussion (section 1.1) that excess concentration of ROS is harmful to the human body and lead to numerous disorders. Various methods such as mass spectrometry, fluorescence measurement [8-10], colorimetric assays [11, 12], electrochemical methods [13-18], spectrometry [19], and cell imaging coupled with Raman spectroscopy [20] etc. have been developed to study the generation, evolution, and quantification of ROS. These methods are specific to the product as a result of oxidation of DNA, proteins, biomolecules and lipids, and destructive [21-23].

The electrochemical methods have utilized both, inorganic and enzyme based materials like novel metal (Au, Pt, Ag) nanoparticles [13, 24, 25], carbon nanotubes (CNTs), MoS_2 [26], nanoCeO_2-Pt-RGO layered composite [18], Ag-CNT composites, glucose oxidase and horseradish peroxidase [18] for detection of ROS. However, enzyme free inorganic sensors are preferred choice for the scientist because of ease of handling and storage condition. Scientists have successfully detected nanomolar concentration of H_2O_2 *in-vitro* in living cells using N-formylmethionyl-leucyl-phenylalanine (fMLP) to stimulate H_2O_2 production [26]. Kodera *et al.* [27] HOCl concentration in the range of 0.2-6.0 mg.dm^{-3} using reduction wave based on anodic cyclic voltammetry method at 1350 mV vs AG/AgCl. Gold deposited Si chip has been used as a transducer layer to detect free chlorine and understand the relative concentration of HOCl/ClO^- in pH range of 5-8 by amperometry [28]. This chip provides good free data independent of solution pH while oxygen is dissolved in the solution, whereas Pt electrode has shown a strong dependence on pH. Olivé-Monllau *et al.* [29] have developed flow injection system the continuous monitoring of the free chlorine detection in concentrations range from 0.2 to 5 mg l^{-1}.

However, these methods lack in sensitivity, specificity, the location of ROS generation and specific production rate [2].

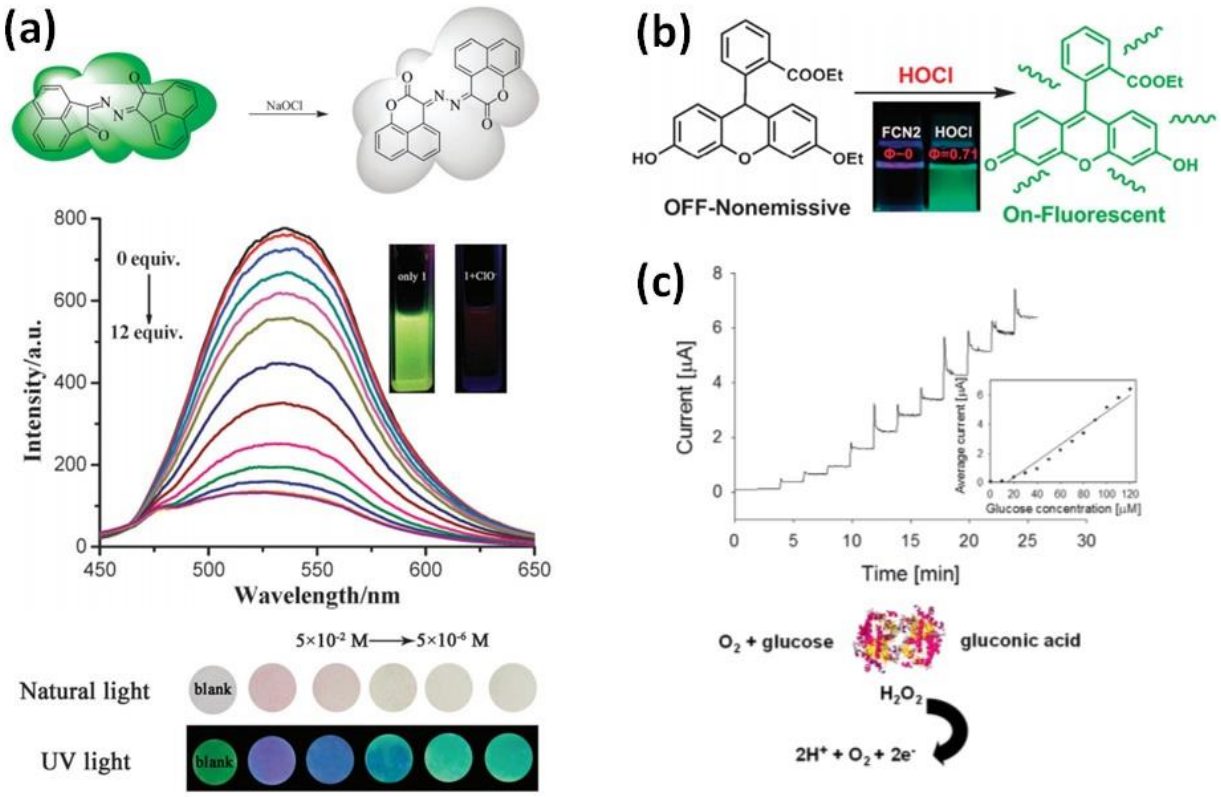

Figure 3: Methods developed for the detection and qualification of free radicals. (a) and (b) fluorescent probes exhibiting the HOCl detection. Reproduced from [30] and [31] with permission of The Royal Society of Chemistry. (c) Nanoceria-Pt-RGO nanocomposite for glucose sensor and H_2O_2 detection. Reprinted from [32] with permission from Elsevier.

Advancement in microscopy and imaging techniques have turned the attention towards noninvasive and destructive tools such as fluorescent probes [2]. These probes provide high specificity and sensitivity in vitro and on paper slips [31]. Use of fluorescent probes has also allowed the evolution and monitoring of ROS in vivo. Raman and confocal imaging with superior spatial and temporal resolution have further enable the site specific

production of ROS during physiological processes and provide information of contribution of ROS in physiological processes [2]. Probes developed for in vivo studies should be nontoxic, easy to internalized by cells/ organelles, and most importantly should not start other metabolism processes.

Two type of fluorescent probes are common in use in vivo and in-vitro which activate in the presence of a specific analyte, (i) off/on type fluorogenic probes and (ii) masked fluorophore type probes. The shift in emission wavelength or change in fluorescence upon activation defines the off/on characteristic. Zhao et al. [31] developed acenaphthenequinone based probe for HOCl detection and tested in solution and on a paper strip. A linear relationship was observed for 0-50 μM concentration of NaOCl at 538 nm wavelength at pH 7.4 in the presence of PBS/THF (Figure 3a). The lower detection limit of this probe is 0.38 μM HOCl. Figure 3a shows the change in fluorescence emission under UV exposure (365 nm) where the concentration of OCl^- decreasing from $5x10^{-2}$ M to $5x10^{-6}$ M. Confocal imaging of BEL-7402 cells incubated with these probes show decease in fluorescent intensity after HOCl addition exhibiting excellent spatial resolution and specificity. Figure 3b show the fluorescent emission from water soluble turn ON dihydrofluorescein-ether probe when activated with HOCl.[30] Mechanism of activation of this probes is oxidation by HOCl. These probes retain their emission for ~10 minute. No activation of probes was observed when titrated with other ROS and RNS.

Masked type probes activate by the attack of oxidants on masked group releasing fluorophore compound [2]. Photo-induced electron transfer act as a switch for fluorescence emission. Fluorescent probes can be used for labeling therapeutic drug loaded organic and inorganic nanoparticle to track their delivery route, internalization in

tissues/cells and effect of therapeutic drug release. Thus, fluorescent probes have been a useful tool in pharmaceutical research.

1.4 ROS scavenging and antioxidants properties of cerium oxide nanoparticles (CNPs)

As discussed in the previous section that antioxidants help in regulating the ROS concentration. In particular cases, antioxidants need to be supplied to the body to control the anomalous production of ROS. Oxalic acid, phytic acid, tannins, eugenol, lipoic acid, ascorbic acid (vitamin C), ubiquinone (coenzyme Q), α-tocopherol (vitamin E), melatonin etc. are common organic antioxidants. These antioxidants are delivered to the body by food or in the form of medication. However, these antioxidants are not effective enough in acute conditions such as melanoma cancer, ovarian cancer, and Alzheimer's disease. The inefficiency of above-mentioned antioxidants has allowed researchers and scientists to look beyond the conventional antioxidants/chemotherapeutics.

Researchers have studied several inorganic nanomaterials with/out a combination of conventional antioxidants for downregulating effect of strengthened production of ROS. CeO_2 [33, 34], TiO_2 [35] and V_2O_5 [36] have shown biocatalytic activity in physiological process owing to their multiple redox states. Cerium oxide nanoparticles (CNPs) are of particular interest because of it low reduction potential which allows its surface to regenerate. CeO_2 is an oxide of lanthanide series metal cerium. It has much technological application in the catalytic converter, solid oxide fuel cells, chemical mechanical planarization (CMP), corrosion resistance etc. [37-40]. In nature, cerium exists in dual oxidation state i.e. Ce^{3+} and Ce^{4+}. At the nanoscale, CNPs surface coexists as Ce^{3+} and Ce^{4+} oxidation state making their surface very dynamic. The presence of oxygen

vacancies in the cerium oxide lattice due to the existence of Ce^{3+} ions provide oxygen buffering capacity [41, 42]. The low redox potential of Ce^{3+} to Ce^{4+} conversion and vice versa has led to unique antioxidant and radical scavenging properties in CNPs. Therefore, CNPs have originated potential application in health care research [43-48]. Oxygen vacancies in ceria lattice, where $Ce^{3+} \leftrightarrow Ce^{4+}$ occur, act as catalytic sites for scavenging scavenge superoxide, hydrogen peroxide radicals, and reactive nitrogen species (RNS). Several factors like nanoparticle size, method of nanoparticle preparation, microenvironment (pH, polymer, ionic strength) and storage conditions affect defects concentration (oxygen vacancies) and surface chemistry (Ce^{3+} to Ce^{4+} ratio) in CNPs, thus their antioxidant properties. Therefore, numerous synthesis method has been reported in the literature to regulate Ce^{3+}/Ce^{4+} ratio in CNPs. Research articles also indicate that antioxidant/scavenging properties of CNPs vastly varies with Ce^{3+} to Ce^{4+} ratio. CNPs having high Ce^{3+}/Ce^{4+} are more effective in scavenging superoxide and hydroxyl radicals. Whereas, CNPs of low Ce^{3+}/Ce^{4+} have more affection towards H_2O_2 and NO* radicals (table 1) [3]. Thus, specific ROS have been targeted with CNPs by controlling its surface chemistry and their efficacy has been tested in various oxidative stress conditions [3].

Table 1: Dependence of radical scavenging property of cerium oxide nanoparticles on surface oxidation state. Reproduced with permission from [3]. © Future Medicine Ltd

Catalytic activity	**↑ Ce^{3+}/Ce^{4+}**	**↓ Ce^{3+}/Ce^{4+}**	**Size (nm)**
SOD mimetic	Yes	No	3-5
OH* scavenger	Yes	No	5-10
Catalase mimetic	No	Yes	8-16
NO* scavenger	No	Yes	3-10

SOD: superoxide dismutase, OH: Hydroxyl, NO Nitric oxide

The fenton-type reaction has been hypothesized (equation 13-16) by Karakoti et al. [33] for the regeneration of CNPs surface. Oxidation of Ce ion takes place through intermediate compound cerium oxy-peroxo complex [$CeO_2(OH)_2$] formation and internal charge distribution. Complete regeneration of 5 mM 20vol% PEG-coated CNPs solution have been seen in 21 days. Recently, Lee at al. [49] has synthesized 3-8 nm size polymer (oleic acid, PEI, PAA-OA, PMAO) coated CNPs to understand the regenerative behavior. The fenton-type reaction has been supported by GC-MS studies. For Ce^{4+} to Ce^{3+} reduction, oxygen evolution takes place when treated with H_2O_2. Reaction ratio Ce^{3+}:H_2O_2:O_2 is 1:2:1 which is in good agreement for Fenton reaction [49]. Antioxidant activity of synthesized CNPs is 9 times higher than commercial antioxidant Trolex. Furthermore, oleic acid coated CNPs have shown regeneration of CNPs surface for 18 times over a period of 6 months at 10 μM H_2O_2 injection each cycle [49].

$$CeO_{2-x} + H_2O_2 \rightarrow CeO_2 + 2OH^- \quad (13)$$

$$CeO_2 + 2OH^- \rightarrow CeO_2(OH)_2 \quad (14)$$

$$CeO_2(OH)_2 \rightarrow CeO_2 + \frac{1}{2}O_2 + H_2O\ (in\ air) \quad (15)$$

$$2Ce^{IV}O_2(OH)_2 + 2H^+(aq.) \rightarrow 2CeO_{2-x} + 3H_2O + \left(\frac{1}{2} + x\right)O_2(in\ aqueous\ medium) \quad (16)$$

Surface modification of inorganic nanoparticles also facilitates the size and shape modulation, long-term stability, and functionalization with specific molecules [50, 51]. Dextran [34], chitosan [52], citrates [53, 54], carboxy–PEG4–amine [55], polyethylene glycol (PEG) [33, 56], polyacrylic acid [57] are commonly used polymers for surface modification. Synthesis of polymer-coated nanoparticles is effectively internalized by cells with the minimum unintentional reaction between nanoparticles and human body and toxicity, due to uniform size distribution and spherical shape.

Polymer coating is also required to synthesize uniformly distributed CNPs in basic conditions and long-term stability. Solid solubility of cerium ions is very low at basic pH. Precipitation of cerium hydroxide occurs immediately after NH_4OH addition because ionic product crosses the solubility limit [58]. Ce ions form a complex with a hydroxyl group-containing polymers and do not precipitate in basic solutions because of a decrease in free Ce ion concentration. Therefore, the concentration of polymer molecules should be equal or higher than Ce ions to avoid precipitation. CNPs have been synthesized in a basic medium using dextran and glucose for Ce ion complexation [58]. Precipitation behavior of Ce^{4+} ions under oxidizing conditions with increasing pH is shown in figure 4. Ce^{4+} ions are stable under pH 2.0. Cerium oxide forms stable colloidal suspension (CeO_2) at pH 2-3.5. When pH is maintained in acidic conditions but above 3.5, CeO_2•$2H_2O$/$Ce(OH)_4$ exists together and mild precipitation is observed because some Ce^{4+} reduces into Ce^{3+} in the presence of H_2O_2. This is attributed to the low redox potential of Ce ions. Cerium hydroxide [$Ce(OH)_4$] precipitates heavily above pH 6.

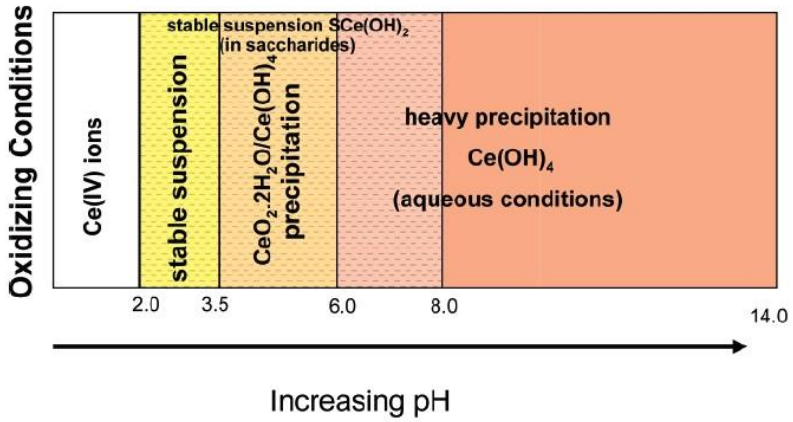

Figure 4: Change in Ce(IV) stability vs pH in oxidizing conditions. Reprinted with permission from [58]. ©2007 American Chemical Society.

Though polymer coated nanoparticles are becoming popular, one should be careful during polymer selection. High molecular weight (M_w) polymer interfere in the catalytic activity of nanoparticles and make it difficult for ROS to reach to the NPs surface. Thus the scavenging activity of NPs decreases and more ROS will be present in the cells/organelles which interfere in physiological processes. Karakoti et al. [33] have reported that low molecular weight (M_w 600) PEG does not adversely affect the superoxide dismutase (SOD) activity as visible from figure 5a. Increasing concentration of PEG has no interference in SOD activity. Figure 5b show the change in color when an equal amount of H_2O_2 was added in the CNP prepared in 0-80 vol% PEG. Intensified color change represent the scavenging of H_2O_2 as Ce^{3+} convert into Ce^{4+}. In UV/Visible spectroscopy this change in color appears in the form of a red shift in peak positions.

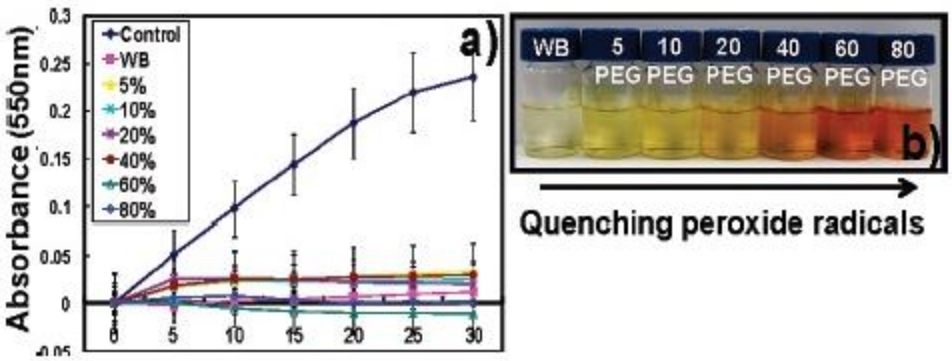

Figure 5: (a) Superoxide dismutase (SOD) activity of PEGlyted CNPs. (b) Change in color of PEGlyted CNPs with H_2O_2 addition showing oxidation of Ce^{3+} to Ce^{4+}. Reprinted with permission from [33]. ©2009 American Chemical Society.

CNPs have been found effective against pathologies associated with chronic oxidative stress and inflammation in both, in vitro and in vivo models. It shows the potential application of CNPs in nanomedicine and regenerative medicine [33, 50, 57-60].

To study the potential of CNPs in fighting Melanoma cancer, in vitro and in vivo experiments were conducted by Alili et al. [61]. Dextran coated and uncoated CNPs were utilized in the study. Particle size of dextran coated CNPs was 3-5 nm. UV/Visible spectrum indicate the higher Ce3+/Ce4+ ratio in coated CNPs because the peak at 254 nm (Ce^{3+} peak) has higher intensity than peak at ~296 nm (Ce^{4+} peak). Contrary to this, Ce^{4+} peak is more predominant in uncoated CNPs. SOD activity of dextran coated CNPs is higher than uncoated CNPs. In vitro cell viability study demonstrate the invasive property of CNPs towards cancerous cells than healthy stromal cells as lower cell viability was observed for melanoma cancerous cells whereas no adverse effect was seen in stromal cells. For in vivo studies, in the nude mice, A375 cells were injected into nude mice to introduce tumor [61]. Three groups each containing six mice were treated

differently. Group 1 mice were not treated with CNPs and acted as a control. Group 2 mice were started giving coated CNPs after 1 day of tumor injection and group 3 mice were given coated CNPs after 10 days of tumor injection [61]. CNPs were injected every alternate day and the tumor was removed after 30 days post tumor injection. Significantly lower tumor growth was detected in CNPs treated group 2 and 3 than group 1. Smaller tumor volume of about 75% (1day, group 2) and 85% (10 days, group 3) in contrast to mock-treated controls [61]. These findings indicate a positive effect on inhibition of malignant melanoma growth *in vivo* by coated CNPs.

1.5 Structure of the dissertation

The subsequent chapters of the dissertation are organized as explained below. Chapter 2 demonstrate the method of controlling the surface chemistry of cerium oxide nanoparticles by introducing defect and their effect on radical scavenging relevant to cancer therapeutics and biosensing applications. In chapter 3, an attempt has been made to control the surface oxidation state of cerium oxide in thin films grown by atomic layer deposition method. Chapter 4 discuss the method of collecting different size particles/nanosheets of MoS_2 and their edge-defect structure. Through electrochemical experiments and density functional theory, the standing of MoS_2 edges and defects have been developed for reactive oxygen species detection. Conclusions of the work are discussed in Chapter 5. Finally, future scope of work is presented for the advancement of the work.

CHAPTER TWO: DOPED CERIUM OXIDE NANOPARTICLES AND ITS BIOCATALYTIC BEHAVIOR

The work presented in this chapter has been published before in

Journal of Materials Chemistry B, 2016, 4, 3195-3202. DOI: 10.1039/C6TB00396F

2.1 Introduction

Cerium oxide is the most abundant material in the lanthanide metal oxides. It is widely used in oxygen sensors [41, 42], catalytic converters [38, 39] and solid oxide fuel cells [40]. The discovery of the redox-active nature (low redox potential) of cerium ions (Ce^{3+} and Ce^{4+}) present at the surface of cerium oxide nanoparticles (CNPs), has opened new avenues for biomedical application [43-48], electrochemical bio-sensors [18], radiation protection [62], corrosion-resistant coatings [37], etc. Researchers have also demonstrated the unique regenerative antioxidant properties of CNPs through in-vitro model systems; specifically, the particles' abilities to scavenge superoxide, hydrogen peroxide radicals, and reactive nitrogen species such as nitric oxide and peroxynitrite have been demonstrated [63-65]. Dowding *et al.* [4] have reported in a detailed study that CNPs ease endogenous peroxynitrite and Aβ-induced mitochondrial fragmentation and neuronal cell death by neuronal internalization. This is followed by CNPs accumulation at the proximity of the mitochondrial and plasma membranes. The concentration of protein tyrosine nitration and reactive nitrogen species in neurons exposed to peroxynitrite decreases with CNPs having higher Ce^{4+}; thus preventing mitochondrial dysfunction and neuronal cell death suggestive of a potential treatment of for neurodegeneration disease [4, 44]. Citrate/EDTA coated CNPs (size 3 nm) have also demonstrated their

effectiveness in targeting affected brain tissues in experimental autoimmune encephalomyelitis (EAE) induced rat model of multiple sclerosis by passing through the blood-brain barrier which results in a decrease of reactive oxygen species (ROS) [44, 66]. Results of in-vivo study of ischemic shock (caused by ROS) induced rats treated with 3-4 nm phospholipid PEGylated CNPs show an increased concentration of CNPs in the brain as compared to liver and kidneys; thus revealing the therapeutic protection towards ischemic brain tissue due to mixed oxidation state (Ce^{3+} and Ce^{4+}) [44, 67].

However, the antioxidant properties of CNPs are highly dependent on particle size as well as on surface coating [49]. It is clearly evident from the above-mentioned studies that the scavenging ability of CNPs and their enzyme-mimetic activities towards different radicals is dependent on their surface oxidation state. Radiation treatment [68], doping [69, 70] and high-temperature treatment [69] are common methods used to tune the surface oxidation state or catalytic activity of CNPs. Kumar *et al.* [68] irradiated (2MeV helium ions) single and polycrystalline cerium oxide film grown by molecular beam epitaxy and reported 13% and 19% increase in trivalent cerium concentrations, respectively. Another study by Kumar *et al.* [69] showed that Eu doping in cerium oxide lattice by co-precipitation method result in Ce^{3+} oxidation state (18.3% to 23.5% for 1 mole% Eu-CNPs and 30 mole% Eu-CNPs, respectively) and when subjected to high-temperature annealing treatment, Ce^{3+} oxidation state concentration decreased to 14.0%. Defect concentration of 1 mole% Eu-CNPs and 30 mole% Eu-CNPs increased from 1.61x1020 cm^{-3} to 4.03x1020 cm^{-3}, respectively [69]. However, large scale agglomeration was observed in the synthesized nanoparticles which make them unlikely to use for the biomedical application. Additionally, irradiation method for tuning the surface oxidation

state of CNPs require radiation facility and will be a challenge for scale up process. The surface oxidation state of CNPs also depends on the particle synthesis methods employed [3, 43]. Therefore, different preparations scavenge different radicals. However, it is very hard to control physical parameters while synthesizing different surface oxidation state CNPs. High temperature synthesis results in higher Ce^{4+} oxidation state and bigger particle size. Moreover, low temperature synthesis in basic medium without capping agents, also results in higher Ce^{4+} oxidation state with no control over particle size. The use of a capping agent solves the problem of agglomeration. It is clearly evident from discussion that doping is successful and relatively easy method to change surface chemistry of CNPs. In the present study, we establish a synthesis method by combining doping method with capping agent and room temperature synthesis to control the surface oxidation state of a stable CNP solution while controlling the size of the particles and prevent CNPs agglomeration. Doping of trivalent elements in the cerium oxide lattice is an ideal pathway to increase the Ce^{3+} oxidation state and the accompanying bio-catalytic properties of these CNPs. For therapeutic applications of nanomaterials, nanoparticles should be well-dispersed, biocompatible and have a narrow size distribution. Synthesis by the precipitation and micro-emulsion routes are commonly used for the synthesis of doped nanoparticles [70-73]. However, broad size distributions and agglomeration of nanoparticles limit the use of the precipitation method in biomedical applications. Additionally, the use of surfactants (AOT, Igpal etc.) and residue from organic phases increases the concern of potential toxicity.

2.2 Experimental

2.2.1 Materials

Cerium(III) nitrate hexahydrate ($Ce(NO_3)_3 \cdot 6H_2O$, purity >99.999%), Samarium(III) nitrate hexahydrate ($Sm(NO_3)_3 \cdot 6H_2O$, purity >99.999%), Lanthanum(III) nitrate hexahydrate ($La(NO_3)_3 \cdot 6H_2O$, purity >99.999%), Erbium(III) nitrate pentahydrate ($Er(NO_3)_3 \cdot 5H_2O$, purity >99.999%) and dextran (Mw=1000 Da) were supplied by Aldrich Chemical Co. (Milwaukee, WI). Ammonium hydroxide (NH_4OH, 1N solution) was procured from Alfa Assar. All the chemicals were used without further purification.

2.2.2 Synthesis of doped cerium oxide nanoparticles (CNPs)

Rare earth element doped CNPs have been synthesized by a precipitation method under the protective environment of biocompatible polymer dextran. 125 mg of dextran were dissolved in 25 mL of deionized water (dH_2O) at room temperature. Aqueous solution of dextran was stirred for 30 minutes to completely dissolve/disperse the polymer. Stoichiometric amount of cerium and dopant precursor (nitrate) were added in the aqueous dextran solution and further allowed to stir for 30 minutes. In the next step, 100 µL 1N ammonium hydroxide was added to the solution which eventually convert the cerium and dopant precursors into the doped cerium oxide. To completely oxidize the precursors, solution was allowed to stir for 15 minutes. Reaction between precursors and ammonium hydroxide is shown in equation (18-19). The whole reaction was carried out at room temperature. Recent study have reported that exposure of dextran coated CNPs to light leads to the change in oxidation state of cerium oxide [34], therefore suspensions of doped CNPs were kept in the dark.

2.2.3 Characterization of doped nanoparticles

For X-ray diffraction (XRD) studies, as-synthesized samples were dialyzed against 750 mL dH_2O in 3500 MCO cellulose tube to remove the excess dextran. XRD spectrum from dialyzed samples were recorded using Rigaku D/Max diffractometer with monochromatic Cu K_α radiation (λ = 1.5418 A°) to check the phase separation between cerium oxide and dopant. Size, morphology and crystallinity of doped CNPs were evaluated using Philip (FEI Tecnai F30) high resolution transmission electron microscopy (HRTEM) operated at 300 keV. X-Ray photoelectron spectroscopy (XPS) studies were conducted to estimate the relative fraction of Ce^{3+} and Ce^{4+} oxidation states on the surface of nanoparticles, confirm the doping element and relative atom% of doping in mixed oxides. Perkin-Elmer 5400 ESCA system (Mg K_α X-ray irradiation (1253.6 eV) and 300 W power) was utilized for XPS studies. Zetasizer (Nano-ZS) from Malvern Instruments, Houston, TX was used to measure surface charge of the nanoparticles.

2.2.4 Catalytic activity

Quantitative determination of superoxide dismutase (SOD) and catalase activity of doped CNP nanoparticles were carried out with SOD assay kit [Sigma Aldrich, Kit #19160-1KTF] and Amplex® Red hydrogen peroxide assay kit [Invitrogen, Catalog Number # A22188], respectively. Both, SOD and catalase activity were measured at three different pH solution; (i) Acetic acid buffer, pH 4.45, (ii) water pH 7 and (iii) HEPES buffer, pH 8. Prepared doped CNPs solutions were diluted to 1 mM using buffer solutions and water. Three different pH solutions were chosen to demonstrate the effectiveness of CNP in acidic, neutral and basic condition. % SOD activity of doped and un-doped CNPs were calculated using equation (17).

$$\% \, SOD \; Activity = \left[\frac{(S1-S3)-(SS-S2)}{(Si-S3)}\right] * 100 \quad (17)$$

Where, S1: slope of blank 1, S2: slope of blank 2, S3: slope of blank 3, SS: slope of sample.

Where, Blank 1: Water (20µL) + WST working solution (200µL) + Enzyme working solution (20µL)

Blank 2: Sample solution (20µL) + WST working solution (200µL) + Dilution buffer (20µL)

Blank 3: Water (20µL) + WST working solution (200µL) + Dilution buffer (20µL)

Sample (SS): Sample solution (20µL) + WST working solution (200µL) + Enzyme working solution (20µL)

2.2.5 Cell culture

2.2.5.1 Toxicity assessment of doped CNPs.

Dextran-coated CNPs have demonstrated their non-toxic behavior for healthy cells [63]. However, it is necessary to evaluate the toxicity of doped CNPs. This study was conducted with primary HUVEC cell line for preliminary results. HUVEC cells were cultured in 96-well plates and exposed to CNPs for 48 hours [43]. Thiazoyl blue tetrazolium bromide (MTT, 1.2 mM) was added in each well at the end. Cell viability was analysed as ratio of the absorbance value of treated samples to untreated controls [43]. Cell viability was reported in percentage of control.

2.2.5.2 Intercellular ROS estimation.

Again, HUVEC cells were seeded with a density 3000-5000 cells/well in 96 well plates and incubated for 24 hrs for preliminary study. Later, a known amount of H_2O_2 with or without doped CNPs were added in each well and again incubated for 24 hrs. After incubation, growth media was removed and cells washed with PBS solution twice and

exposed to 50 µM DCFDA in PBS solution for 30 minutes. Plates were then analyzed using fluorescence spectrophotometry at 485 nm. The amount of fluorescence intensity is directly proportional to ROS.

2.2.5.3 Confocal microscopy.

30,000 HUVEC cells were seeded per cover slip and then incubated overnight. Cells were treated with different nanoparticles (CNPs, CNPs -10% La, CNPs-10% Sm, CNPs-10%-Er) at 1 µM and incubated for 3 hr. Next, H_2O_2 (final concentration 10 µM) was added to the wells with or without nanoparticles and incubated for 6 hr. Then cells were washed with sterile saline three times and 2',7'-dichlorodihydrofluorescein diacetate (H2DCFDA; final concentration 50 µM) was added to the wells, and incubated for 30 min. Finally, cells were washed with sterile saline and immediately, imaged under a confocal (Carl Zeiss confocal microscope with Volocity image processing software) microscope as described in our previous publication [74].

2.2.5.4 Fluorescence spectroscopy.

3,000-5,000 HUVEC cells were seeded in 96-well black or fluorescence plate and incubated overnight. Cells were treated with different nanoparticles (CNPs, CNPs -10% La, CNPs-10% Sm, CNPs-10%-Er) at 1 µM and incubated for 3 hr. Next, H_2O_2 (final concentration 10 µM) was added to wells with or without nanoparticles and incubated for 6 hr. Then cells were washed with sterile saline three times, and 2',7'-dichlorodihydrofluorescein diacetate (H2DCFDA; final concentration 50 µM) were added to the wells and incubated for 30 min. Finally, cells were washed with sterile saline and fluorescence intensities were measured using Fluostar Omega form BMG labtech.

2.3 Results and discussion

In this study, we synthesized CNPs doped with lanthanum (La), samarium (Sm) and erbium (Er) to alter the Ce^{3+}/Ce^{4+} oxidation state in a controlled way for different applications. These dopants were selected based on their ionic radius. The ionic radius of Sm^{3+} (0.96Å) lies between Ce^{3+} (1.03Å) and Ce^{4+} (0.92Å). The ionic radius of Er^{3+} (0.87 Å) is smaller than Ce^{4+}, whereas the La^{3+} (1.06 Å) ionic radius is bigger than Ce^{3+}. To demonstrate the tunability of surface Ce^{3+} to Ce^{4+} ratio, dopant concentration was varied as 5, 10 and 20 mole percent. Rare earth element-doped CNPs have been synthesized by a precipitation method in presence of 1000 molecular weight biocompatible polymer, dextran, at room temperature. Therein, Dextran was dissolved in 25 mL of deionized water (dH_2O) at room temperature. Then, a stoichiometric amount of cerium and dopant nitrate precursors were added to the aqueous dextran solution followed by addition of 1 N ammonium hydroxide. To completely oxidize the precursors, the solution was stirred for 15 minutes. A synthesis schematic of dextran-coated, doped CNPs is presented in figure 6. The reaction between precursors and ammonium hydroxide is shown in equation (18 and 19).

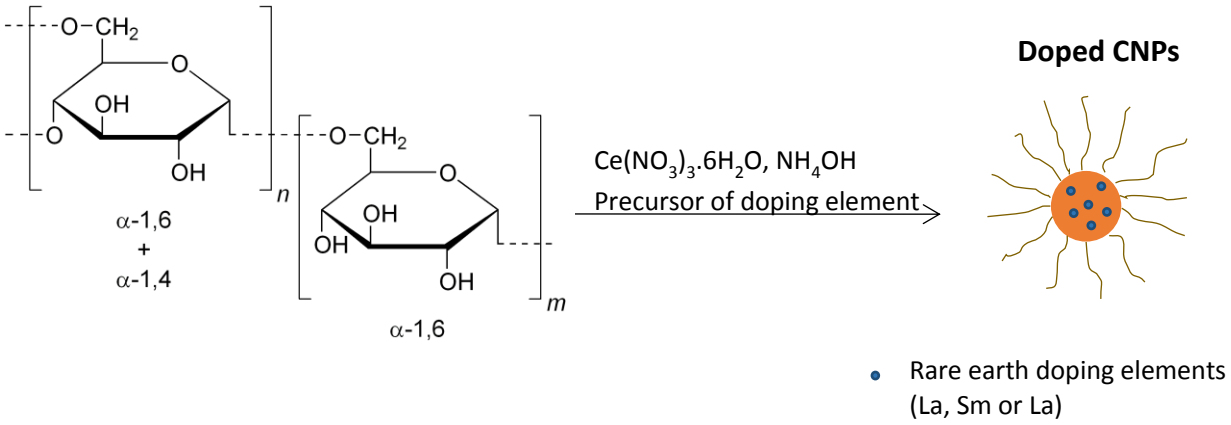

Figure 6: Schematic of synthesis of dextran coated doped cerium oxide nanoparticles.

$$Ce(NO_3)_3.6H_2O + xM(NO_3)_3 + NH_4OH \rightarrow Ce_{1-x}M_x(OH)_4 + NH_4NO_3 + H_2O \quad (18)$$

$$Ce_{1-x}M_x(OH)_4 \rightarrow Ce_{1-x}M_xO_{2-y} + 2H_2O \quad (19)$$

Where M is doping element (La, Sm and Er), x is mole fraction and y is a stoichiometric value of oxygen vacancies. Recently, a study has reported that exposure of dextran-coated CNPs to light leads to a change in the oxidation state of cerium oxide [34]; therefore, suspensions of doped CNPs were kept in dark. For X-ray diffraction (XRD) studies, as-synthesized samples were dialyzed against 750 mL dH_2O in 3500 MCO cellulose tubes to remove the excess dextran. The XRD spectra of dialyzed samples were recorded to check the phase separation between cerium oxide and the dopants. Size, morphology and crystallinity of doped CNPs were evaluated using HRTEM.

XRD spectra of dextran–coated, doped CNPs show a broad peak representative of the (111), (200) and (311) lattice planes (Figure 7). Peaks correspond to (200) and (222) were not clearly visible due to peak broadening (particle size 5-7 nm) and the presence of dextran on the nanoparticles' surfaces [34]. Doped CNPs have a particle size of 5-7 nm with a uniform size distribution [Figure 8(a, b)]. Presence of lattice fringes and the concentric ring pattern in SAED obtained from 20 mole% Sm-doped CNPs confirm the crystalline nature of the nanoparticles. The indexed SAED pattern shows the FCC lattice structure corresponding to cerium oxide: further suggesting the absence of phase separation between cerium oxide and dopants [Figure 8(c)]. The presence of rare earth elements in the cerium oxide matrix was also confirmed by EDAX [Figure 8(d)]. It is also important to mention here that doped CNP solutions maintain their colloidal stability for more than a year: indicating good shelf life. The particle size distribution for 10 mole%

Sm-doped CNPs shows only a single peak: demonstrating that particles are well-dispersed [Figure 9].

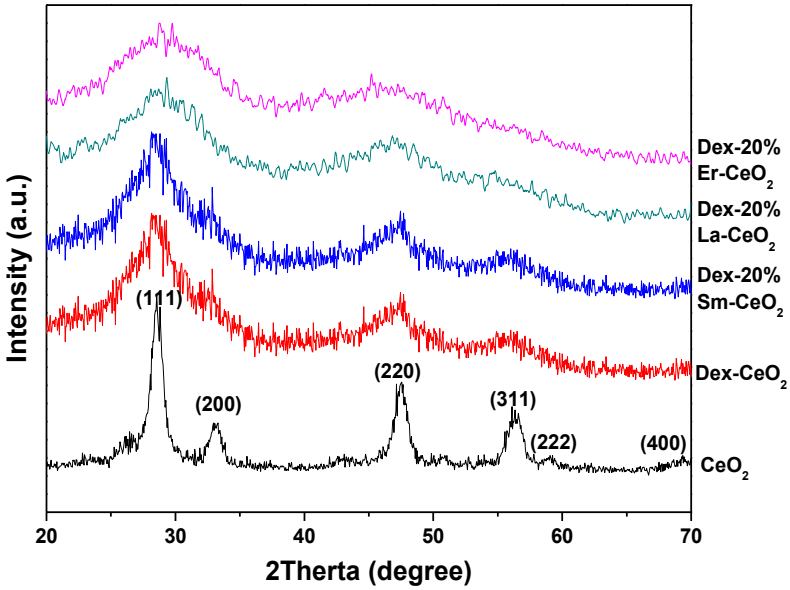

Figure 7: X-ray diffraction pattern of doped CNPs with dextran CNP exhibit the fluorite structure represent a fluorite structure correspond to commercially available CNP. Presence of dextran of CNPs surface and reduction in particle size are attributed to peak broadening. Absence of additional peaks suggests the formation of doped CNPs and dopants do not form additional oxide because of phase separation.

(a)

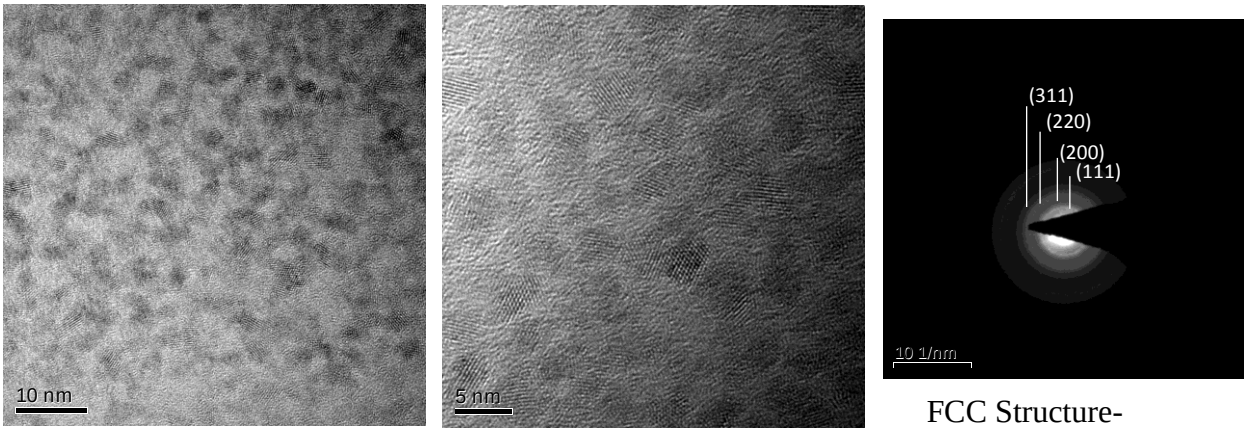

FCC Structure-

(b)

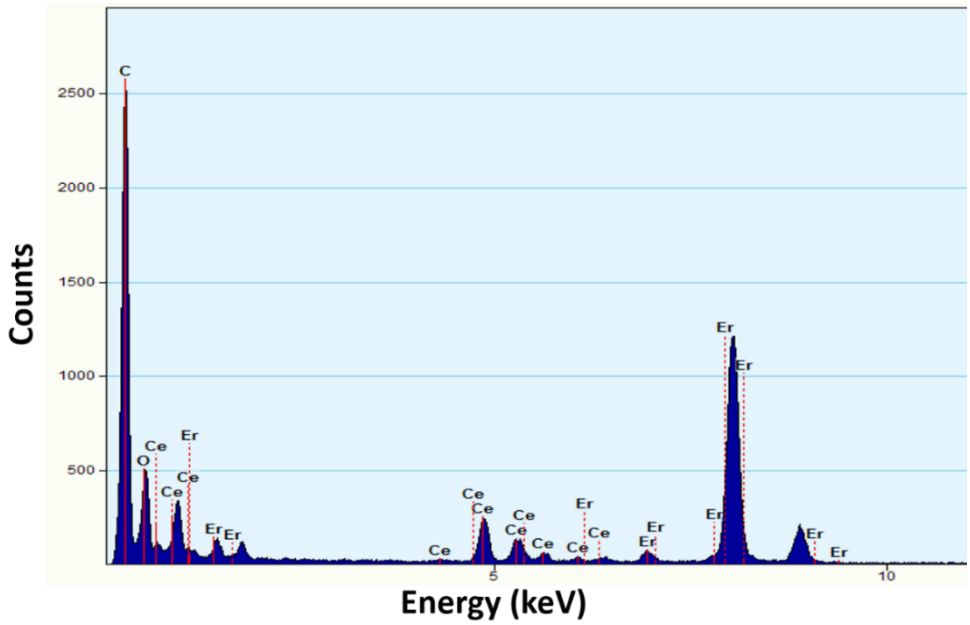

Figure 8: (a) HRTEM micrographs of 20 mole% Sm doped CNPs showing uniform distribution of nanoparticles of 2-7 nm size. Indexed selected area diffraction pattern belong to FCC fluorite crystal structure. (b) Energy dispersive X-ray analysis spectrum of 20 mole% Er doped CNPs shows the elemental composition corroborating the presence of Yb, Er, in cerium oxide. Presence of Cu is from copper TEM grid.

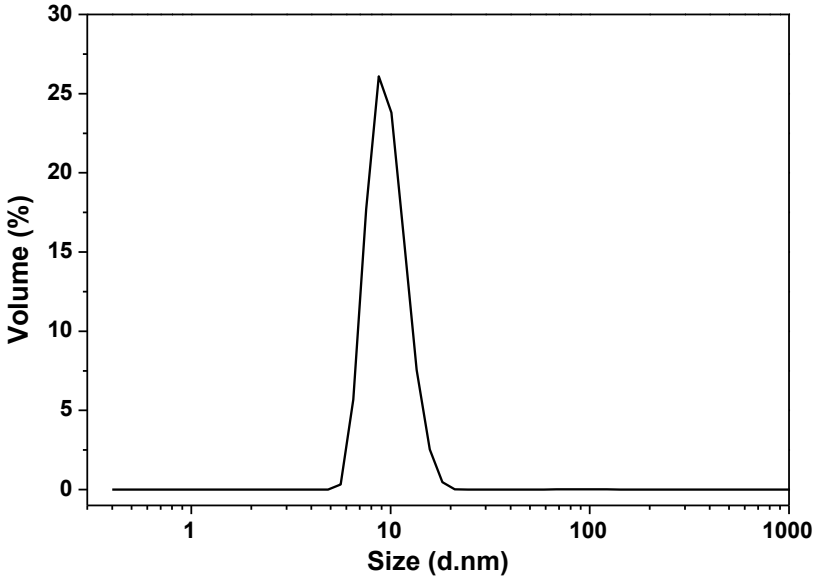

Figure 9: Particle size distribution of 10 mole% Sm doped CNP after one year of synthesis showing the colloidal stability and higher shelf life of nanoparticles.

Smaller size and presence of dextran on the surface of CNPs make it difficult to confirm doping of rare earth elements in the cerium oxide lattice. We have used energy-filtered transmission electron microscopy (EFTEM) and electron energy loss spectroscopy (EELS) to confirm the doping. EFTEM has emerged as a reliable technique to observe the distribution of doping elements in nanostructured and semiconductor materials in recent years [75-77]. Again, the presence of dextran on the surface of nanoparticles (size of 5-7 nm) possess extreme difficulty in obtaining the EELS and EFTEM spectra. To avoid these problems, a 20mole% Sm-doped CNPs were prepared without dextran at room temperature. This preparation leads to agglomeration of nanoparticles as seen in figure 10(a). A large area of Sm-doped CNPs were selected for EFTEM to provide evidence of uniform dopant distribution in the cerium oxide matrix. EELS spectrum collected from figure 10(a) shows the presence of Ce and Sm with M_5

(1086 eV) and M_4 (1110 eV) peaks of Sm and M_5 (885 eV), M_4 (903 eV) and M_3 (1196 eV) of Ce [Figure 10(b)]. 19.7 atom% of Sm was quantified from the analysis of EELS spectra which is close to the amount of precursor added during synthesis. Figures 10(c), 10(d), and 10(e) represent the Ce, Sm and Ce-Sm composite elemental map from the area shown in figure 10(a). The Ce-Sm composite map provides additional evidence of uniform Sm distribution in the cerium oxide matrix. It is also evident from figure 10(e) that Sm was slightly aggregated. This is due to the room temperature synthesis from which no extra energy was provided for the diffusion of dopant into the cerium oxide matrix.

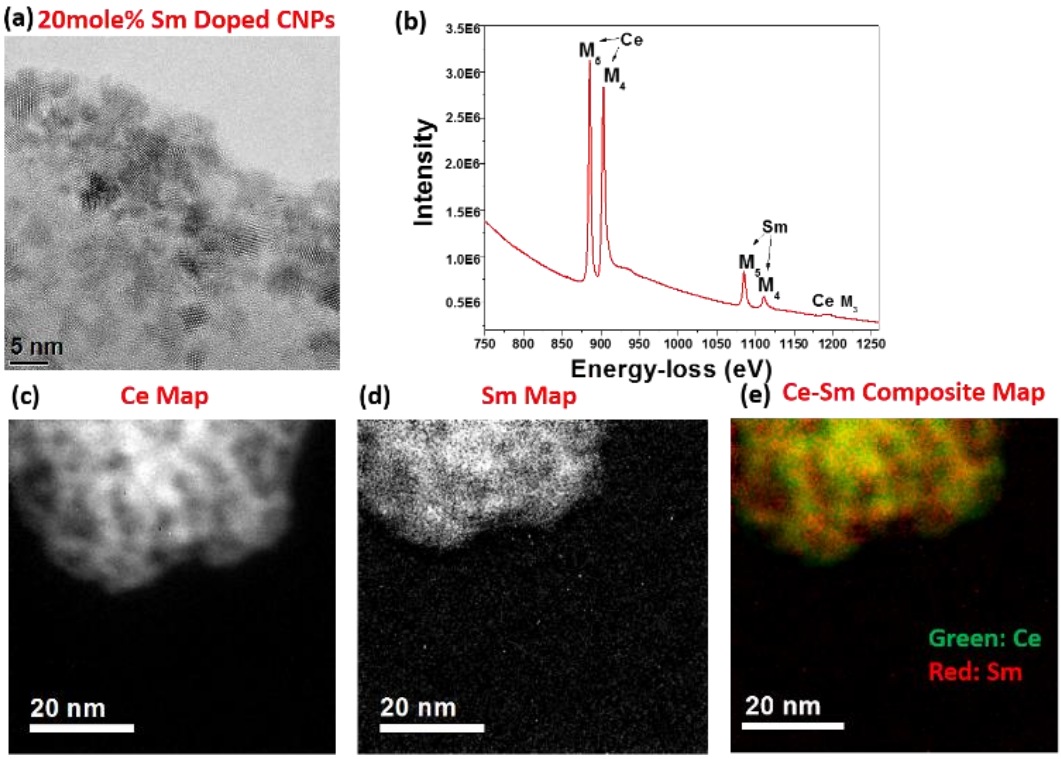

Figure 10: (a) HRTEM micrograph of 20mole% Sm-doped CNPs prepared without dextran at RT showing 5-7 nm crystalline particles. (b) Electron energy loss spectroscopy (EELS) spectrum of (a) confirming the presence of Ce and Sm in sample. (c)-(e) Elemental map of Ce, Sm and composite Ce-Sm map, respectively showing uniform distribution of Sm in Ce matrix.

An ab initio simulation study has suggested that a maximum of 50 mole% of dopants can be substituted into the cerium oxide lattice (for particles prepared by a micro-emulsion method, with AOT as a surfactant, in toluene with excess amount of H_2O_2) [70]. This arises from the exothermic dissociation of hydrogen peroxide which helps in the diffusion of the dopant uniformly in the lattice [70]. Since, in the current study, nanoparticles were prepared at room temperature distribution in the cerium oxide matrix. It is also evident from figure 10(e) that Sm was slightly aggregated. This is due to the room temperature synthesis from which no extra energy was provided for the diffusion of dopant into the cerium oxide matrix. Since, in the current study, nanoparticles were prepared at room temperature and with a minimal amount (100 µL) of NH_4OH used, achieving 20 mole% doping is encouraging. It appears that dextran coating decreases the activation energy required to facilitate doping into the cerium oxide matrix. Moreover, the valence state of Ce and the dopant precursor are the same; therefore, each have a similar probability of forming a complex/binding with dextran. Hence, this reaction proceeded at a high rate (only 15 mins to complete) after addition of NH_4OH to the solution disallowing sufficient time for dopant segregation. It is well known from the literature and classic diffusion experiment that diffusion (two element system) or self-diffusion (isotope system) that concentration of dopant varies along the reference frame to achieve lowest energy state with time at isothermal treatment as well as with increasing temperature. Kuo *et al.* [78] have studies the effect of doping concentration and annealing temperature on structural, optical and electrical properties of Al doped ZnO. This study reveal that electrical conductivity and crystallinity improves with increasing annealing temperature due to higher diffusion rate. Another classic study of hydrostatic pressure,

temperature and doping on tracer diffusion of ^{71}Ge in Ge single crystal is by Werner *et al.* [79]. They reported increase in diffusivity with doping due to vacancy mechanism. However, increasing reaction temperature or annealing temperature can improve the distribution of doping element in cerium oxide lattice, but at higher temperature Ce^{3+} will convert to Ce^{4+} to stabilize electronic configuration. Thus the purpose of tuning the surface chemistry of CNPs will be lost. Furthermore, increased dopant concentration (>20 mole%) will lead to high agglomeration of Sm, thus decreasing the potential catalytic properties.

To understand the effect of dopants on surface chemistry and determine the relative fractions of Ce^{3+} and Ce^{4+} oxidation states on the surface of doped CNPs, XPS studies were carried out. Deconvoluted XPS Ce (3d) spectrum of dextran CNPs and 20 mole% La, Sm and Er doped CNPs are shown in figure 11. Peaks v^0, v', u^0 and u' correspond to Ce^{3+}, whereas peaks v''', v'', v, u''', u'' and u are attributed to Ce^{4+} [80]. The ratio of the integrated area of Ce^{3+} peaks fitted with a Gaussian distribution to the total area under peaks provides semi-quantitative analysis of Ce^{3+} ions at the surface of CNPs. The relative fractions of Ce oxidation state in doped CNPs are presented in table 2. XPS analysis showed up to 40% increase in Ce^{3+} ion concentration in doped CNPs as compared to the control dextran CNPs (see Table 2) because trivalent dopants substitute Ce^{4+} ions in lattice. The presence of one Ce^{3+} oxidation state creates two oxygen vacancies in the cerium oxide lattice. Hence, increases in Ce^{3+} ion concentration also lead to higher oxygen vacancies.

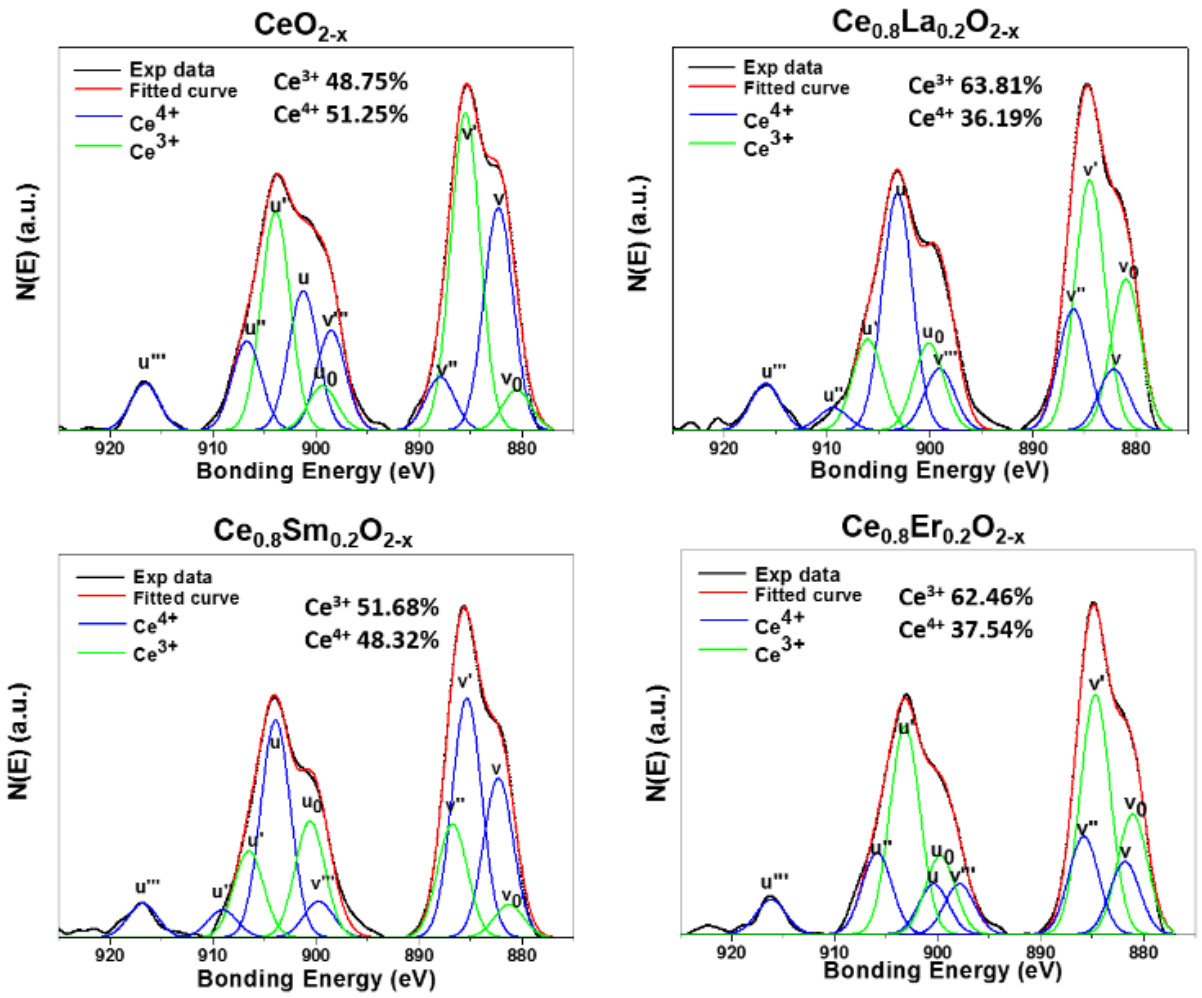

Figure 11: Deconvoluted peak-fitted XPS spectrum of Ce (3d) from (a) pure dextran CNPs, (b) 20 mole% La doped CNPs, (c) 20 mole% Sm doped CNPs, and (d) 20 mole% Er doped CNPs. Doping in CNPs lattice able to increase surface concentration of Ce^{3+} ions. Surface ions concentration on CNPs surface was measured from the integrated area under peaks corresponding to Ce^{3+} and Ce^{4+}.

It is also important to note that the relationship between dopant concentration and Ce^{3+} oxidation state is not linear. The reasons behind this non-linear relationship could be a combination of the imposed lattice strain and the competition between Ce^{3+} and M^{3+}-dopant ions to bind at C_2-, C_2-C_3 or C_3-C_4 hydroxyl group positions in the α-1,6 D-glucose

unit of dextran (because of equal probability and valence state) [81]. As mentioned above the ionic radius of Ce^{3+} is larger than Ce^{4+}; therefore, a larger lattice strain is developed in the nanoparticles. Therefore, the ionic radius of dopant atoms will play an important role in lattice stabilization and may influence the linearity between dopant concentration and Ce oxidation state. Changes in relative peak positions as compared to the dextran CNP control further confirm the change in electronic structure due to the presence of dopant in the cerium oxide lattice.

Table 2: Summary of surface oxidation state of Ce from XPS and zeta potential

Material	**Ce^{3+} (%)**	**Ce^{4+} (%)**	**Zeta Potential (mV)**
Dextran CNP	48.75	51.25	-15.33±0.98
5mole% La-CNP	67.95	32.05	-11.20±2.77
5mole% Sm-CNP	63.80	36.20	-3.89±0.65
5mole% Er-CNP	57.32	42.68	-22.73±0.31
10mole% La-CNP	55.12	44.88	-20.93±1.68
10mole% Sm-CNP	54.83	45.17	-10.9±0.46
10mole% Er-CNP	59.69	40.31	-21.33±0.95
20mole% La-CNP	63.81	36.19	-7.73±1.68
20mole% Sm-CNP	51.68	48.32	-7.90±0.46
20mole% Er-CNP	62.46	37.54	-18.23±0.23

Superoxide dismutase (SOD) and catalase mimetic activities of doped CNPs at pH 7 are shown in figure 12 along with %SOD activity with varying mole fraction of the dopant. The SOD activity of doped CNPs were also measured in acetic acid (pH 4.5) and HEPES

buffer (pH 8), and reported in figure 13. All doped CNPs exhibited higher SOD activity, over control CNPs, in acidic, basic and neutral conditions. The 10 mole% doped CNPs had the highest SOD activity as compared to 5 and 20 mole% doped CNPs of the same dopants [Figure 12(a, b, c)]. This behavior is also clearly visible from the plot of %SOD activity vs %Doping [Figure 12(d, e, f)]. Percentage improvements in SOD activity with reference to Dextran CNP for different doped CNPs are calculated using equation (20) and presented in figure 14. The bio-catalytic activities of these samples provides insight into the effective doping concentration at room temperature. It is evident from figure 12(d), (e), and (f) that Er quickly attained saturation for %SOD activity, whereas La and Sm did not. The SOD activity of La- and Sm- doped CNPs can be further improved with higher dopant concentration and temperature. The correlation between the catalytic activity of doped CNPs with specific dopants (Sm, La or Er) can be explained from their association energy with Ce. Sm and La have positive association energies with Ce [82-84]. As a result, Er repels O-vacancies while La and Sm trap O-vacancies and form complexes. Therefore, the Ce^{4+} to Ce^{3+} reduction decreases in the case of Er and increases for La and Sm. Hence, La and Sm bonding with Ce is stronger; thus, it is easier to substitute La and Sm ions into the cerium oxide lattice. On the other hand, more efforts/energy is required to substitute Er into the cerium oxide lattice. The improvement in SOD activity and Ce^{3+} ions for Er doped CNPs further strengthens our hypothesis that dextran lowers the doping activation energy, facilitating doping in the cerium oxide matrix, and binds ions together.

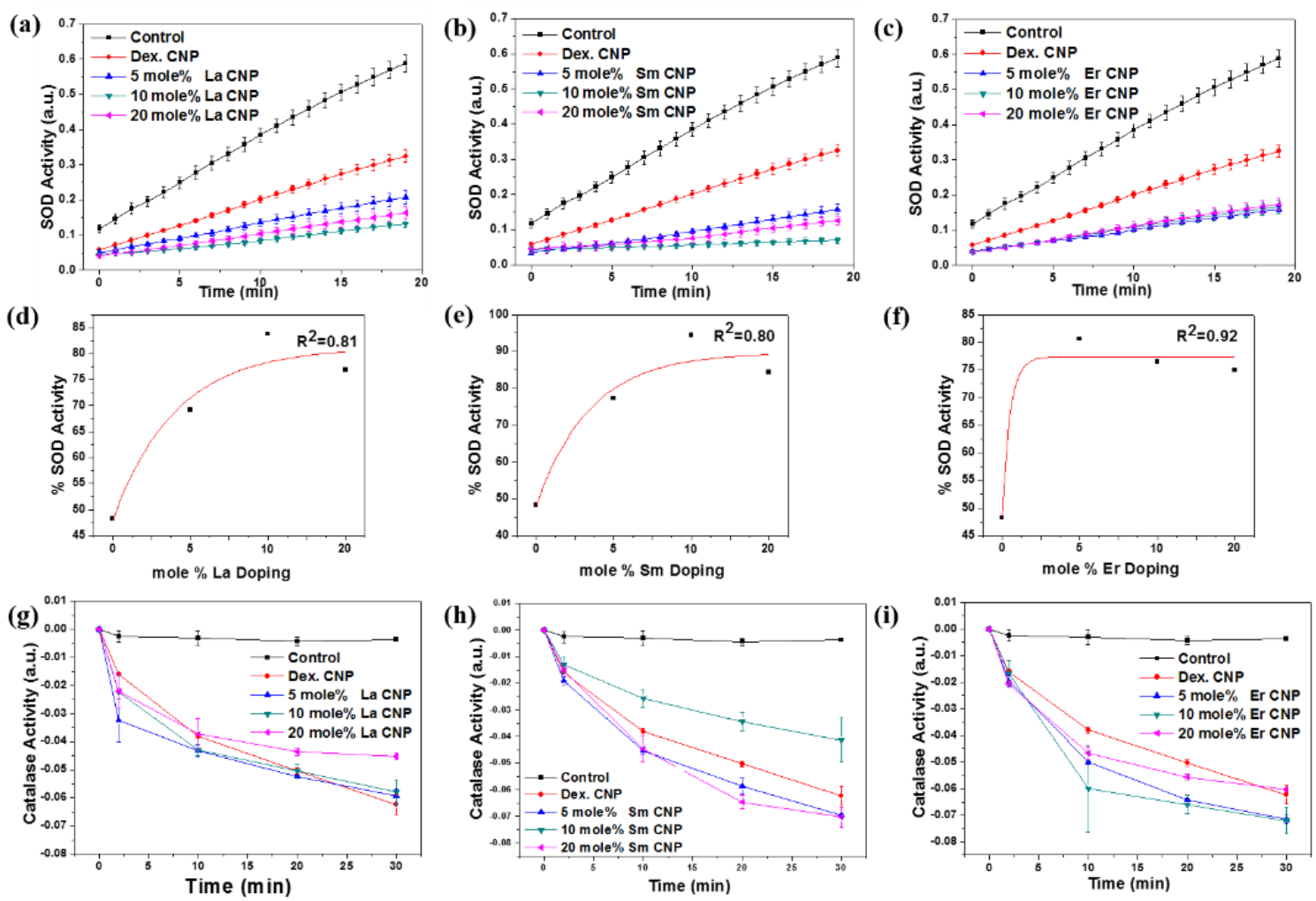

Figure 12: (a)-(c) Superoxide dismutase activity of La, Sm and Er doped CNPs, respectively at neutral pH 7. (d)-(f) %SOD activity of doped CNPs with variation in dopant concentration. (g)-(i) Catalase mimetic activity of La, Sm and Er doped CNPs, respectively at neutral pH 7.

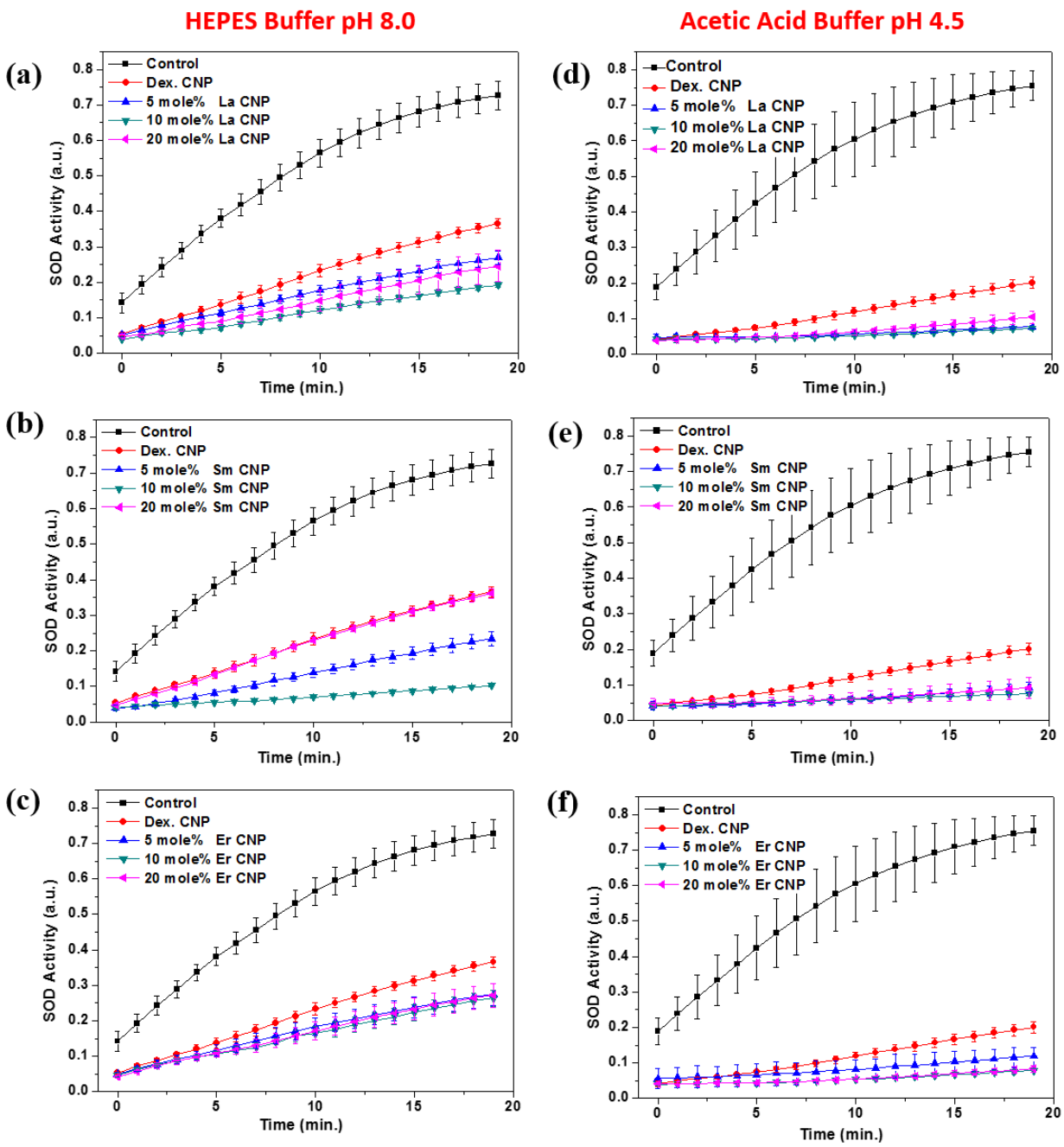

Figure 13: Superoxide dismutase activity (SOD) of doped CNPs. (a)-(c) at basic pH 8 and (d)-(e) at acidic pH 4.5. SOD activity represents the scavenging of super oxide radicals and measured at 565nm.

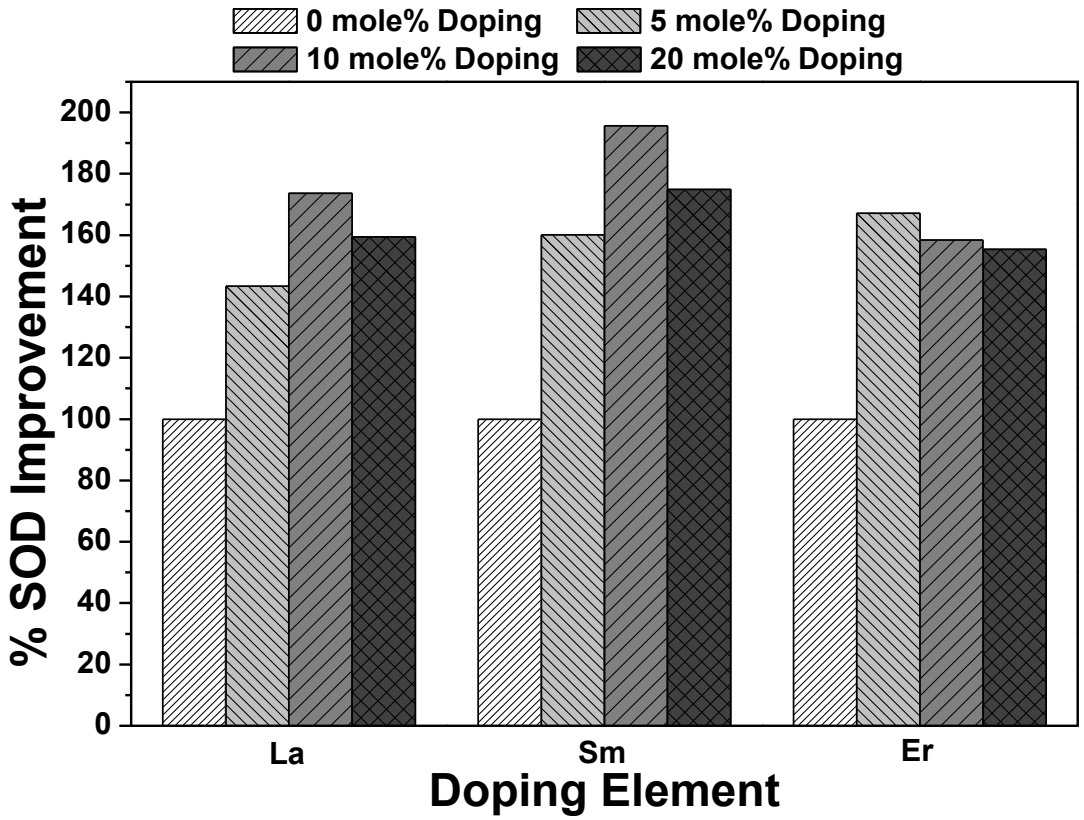

Figure 14: Percentage improvement in SOD activity with doping element and concentration with reference to dextran CNPs.

$$\%\, SOD\ Improvement = \left[\frac{\%\, SOD\ activity_{sample}}{\%\, SOD\ activity_{Dex\ CNPs}}\right] * 100 \qquad (20)$$

At acidic pH 4.5 doped CNPs showed an improved SOD activity over dextran CNPs. However, the effect of dopant concentration is unclear because at high acidic pH, surface ions equilibrate to such an extent that no significant change in SOD activity could be observed [85]. Therefore, these doped CNPs will demonstrate superior performance over dextran CNPs for therapeutic application in highly acidic conditions. It is also evident from figure 12(c) that all the Er-doped CNPs have improved SOD activity over pure dextran CNPs. Among all three dopants, the Sm doped CNPs showed the highest SOD activity followed by La and the lowest for Er-doped CNPs. This ordering was attributed to

the dopant atoms association energy with O-vacancies and the high surface Ce^{3+} concentration. CNPs with higher Ce^{3+} concentrations show increased SOD activity. On the other hand, CNPs with higher Ce^{4+} concentration demonstrate better catalase activity. Thus, SOD and catalase are complementary to each other. It is clear from figure 12(g)-(i) that the catalase activity of La-doped CNPs is greater than Er- and lowest for Sm- doped CNPs. Similar to SOD activity, the catalase activity of doped CNPs is also higher than dextran CNPs at pH 4.5 (see Figure 15).

Confocal microscopy revealed that all CNPs with or without doping were able to reduce intracellular ROS when induced with 10 µM H_2O_2 for 4 hr (Figure 16). However, it was difficult to compare the scavenging activities among the doped CNPs from the confocal image. Therefore, quantification of the intracellular ROS was carried out using fluorescence spectroscopy (Figure 17). Similar to confocal results, fluorescence data showed that, irrespective of doping, all CNPs were able to scavenge significant ($P<0.005$) amounts of intracellular ROS. CNPs and CNPs with 10% Er and 10% Sm doping showed a comparable amount of ROS scavenging, whereas 10% La doped CNPs showed maximum scavenging. This data is in accordance with the test tube catalase activity: where we have seen that CNPs with La doping possess the highest amount of H_2O_2 scavenging compared to other CNPs.

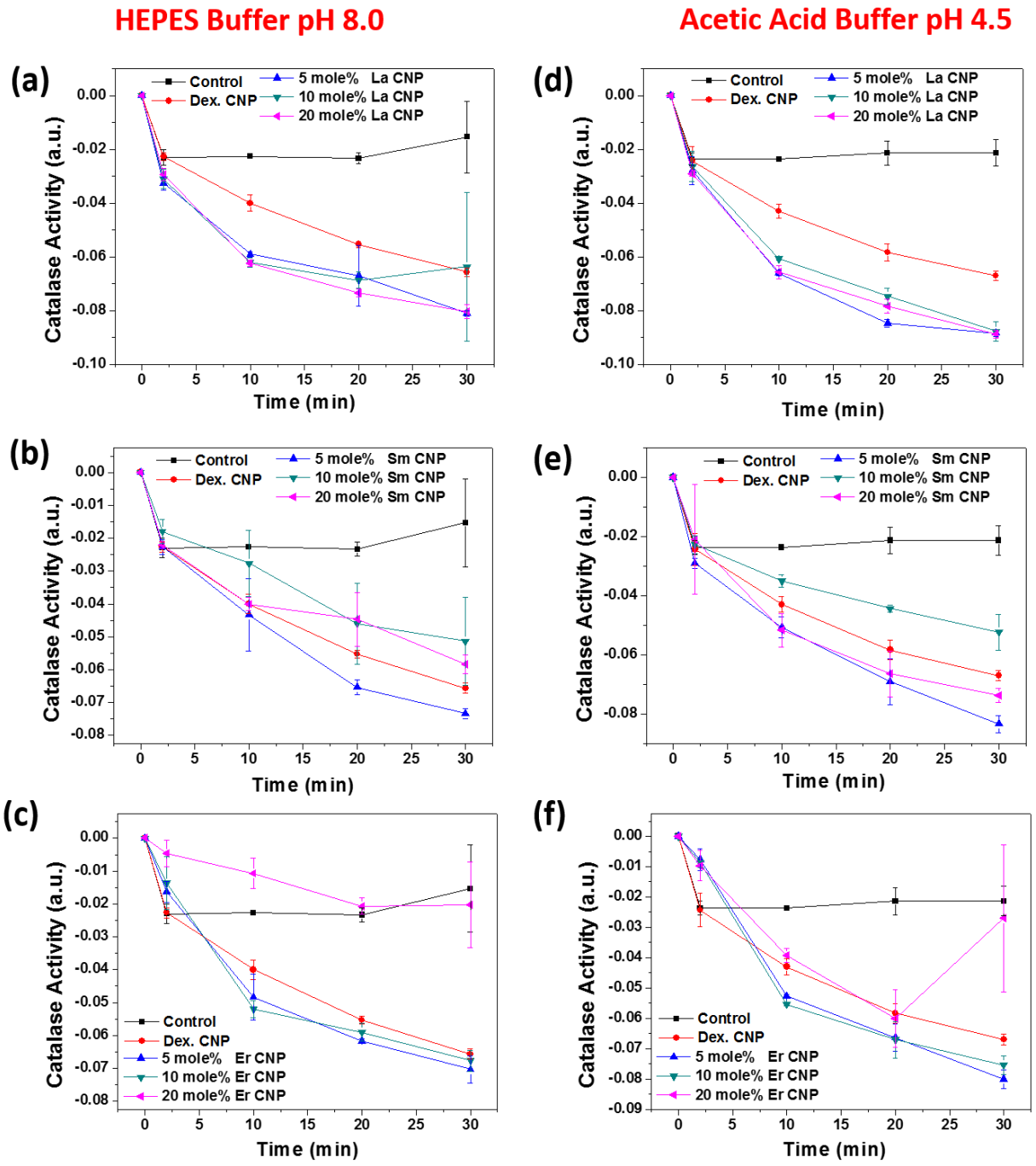

Figure 15: Catalase mimetic activity of doped CNPs. (a)-(c) at basic pH 8 and (d)-(e) at acidic pH 4.5. Catalase activity represents the conversion of hydrogen peroxide into oxygen with time and remaining hydrogen peroxide levels measured at 240nm.

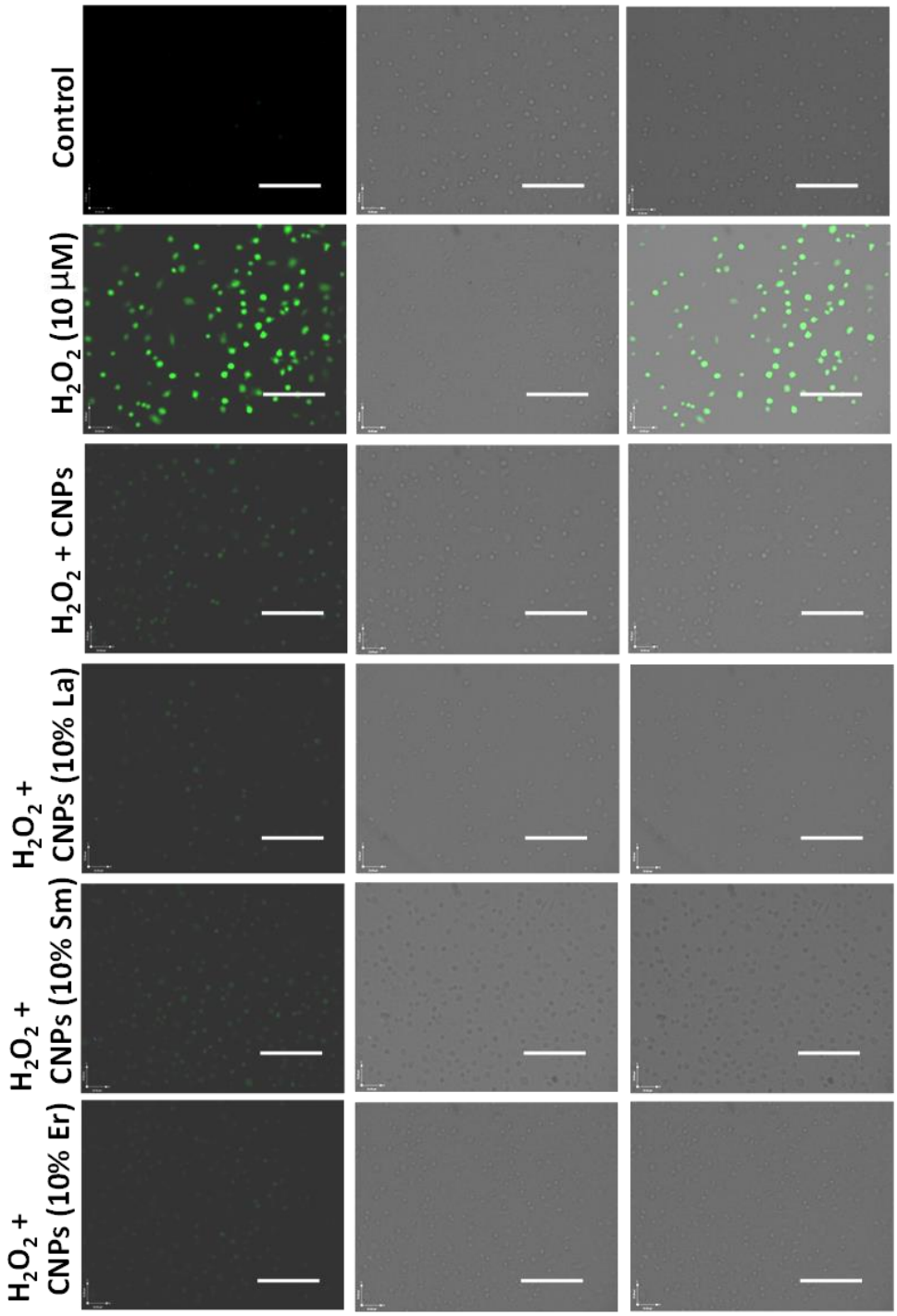

Figure 16: Intracellular ROS scavenging properties of CNPs using confocal microscopy. Pre-treatment with CNPs with or without doping (1 µM final concentration) able to decrease intracellular ROS induced by H_2O_2 (10 µM final concentration) for six hours. Scale bar 100 µm.

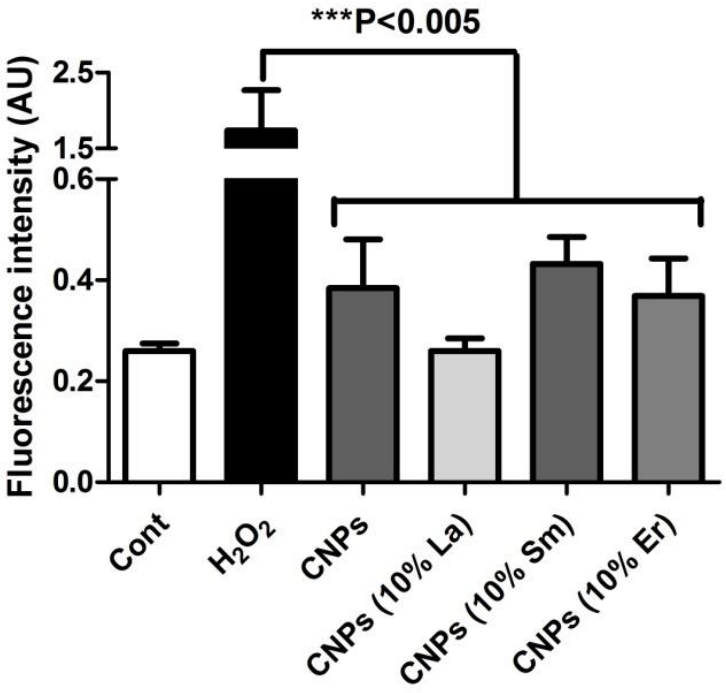

Figure 17: Quantification of intracellular ROS scavenging properties of CNPs with and without doping using fluorescence spectroscopy. Pre-treatment with CNPs with or without doping (1 µM final concentration) are able to decrease intracellular ROS induced by H_2O_2 (10 µM final concentration) for four hours and La doping showed maximum scavenging property.

As mentioned above, cerium oxide has been found useful for therapeutic applications such as Alzheimer's disease, cancer, multiple sclerosis etc. [44, 66, 86]. Despite this, it is always necessary to evaluate CNPs developed using new synthesis procedures for cell viability or biocompatibility. To assess the effect of doped CNPs in a biological model, a monolayer of HUVEC cells were cultured and exposed to different concentrations of doped CNPs. Since the highest catalytic activity in scavenging ROS was demonstrated by 10 mole% doped CNPs, these 10 mole % CNPs were tested for bio-compatibility. Figure 18 shows no adverse toxicity toward HUVEC cells in presence

of doped CNPs for the concentration range 1-50 μM. It is evident from figure 18 that cell viability does not vary significantly from the control.

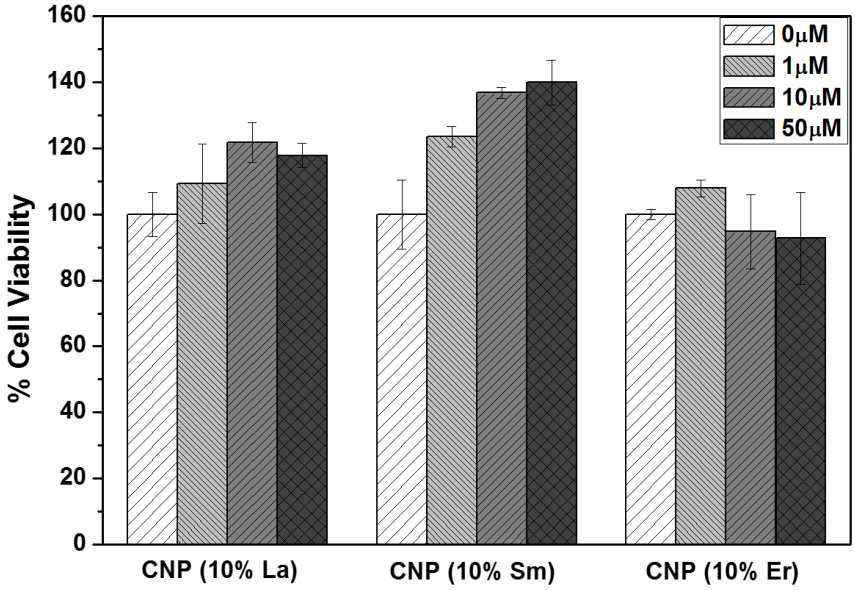

Figure 18: Cell viability of HUVEC cells at different concentration of 10mole% La doped CNPs, 10mole% Sm doped CNPs, and 10mole% Er doped CNPs.

2.4 Conclusions

In this study, we have demonstrated a one-step method to fine-tune the surface Ce^{3+}/Ce^{4+} ratio by appropriate selection and amount of rare earth element doping at room temperature. EFTEM study revealed successful doping and a uniform distribution in the CNP lattice. The doping of CNPs lattice with trivalent dopants significantly increased the surface Ce^{3+} ions concentration and produced superior SOD mimetic activities, as expected. These, higher Ce3+-containing CNPs were efficient scavengers of intracellular ROS. Therefore, using this synthesis method, properly-tuned CNPs can be tailored for specific biological application (higher Ce^{3+} to target inflammation or Ce^{4+} for anticancer/antibacterial activity).

CHAPTER THREE: MIMICKING THE CERIUM OXIDE NANOPARTICLES REDOX BEHAVIOR ON ATOMIC LAYER DEPOSITED THIN FILMS

3.1 Introduction

Cerium oxide has many technological (oxygen sensors [41, 42], solid oxide fuel cells [40], catalytic converters [38, 39], corrosion resistance coatings [37], high *k*-dielectric material) and healthcare applications in electrochemical biosensors [18], radiation protection, cancer therapeutic agent, radical scavenger etc. Magnetron sputtered CeO_2 thin films on SiO_2 substrate have been explored as optical waveguides [87]. CeO_2 thin films as buffer layer between the substrate (Si or sapphire) and $YBa_2Cu_3O_7$ has application in High-*Tc* superconductors [88, 89] High dielectric constant, dielectric strength, and moderate band gap of CeO_2 also present it as a potential candidate for high *k*-dielectric material for CMOS devices. Other factors such as lattice constant (Si 5.431 Å and CeO_2 5.411 Å; mismatch 0.36%) and thermodynamic stability also project it as a potential candidate [90-92].

Cerium ions exist in dual oxidation state (Ce^{3+} and Ce^{4+}) and due to low reduction potential, cerium oxide exhibit redox cycling behavior. Upon conversion from Ce^{4+} ion to Ce^{3+} ion, two oxygen vacancies are generated in the cerium oxide lattice, there it also acts as oxygen buffer. Due to redox cycling and low reduction potential, cerium oxide nanoparticles (CNPs) has shown its effectiveness as antioxidant material for scavenging reactive oxygen species (ROS) and reactive nitrogen species (RNS). CNPs having higher Ce^{3+}/Ce^{4+} ratio scavenge superoxide and hydroxyl radicals (OH*). Whereas lower Ce^{3+}/Ce^{4+} ratio CNPs scavenge hydrogen peroxide (H_2O_2) and nitrox oxide radicals

(NO*). Furthermore, CNPs also regenerates its surface over time, therefore, antioxidant properties last for long period of time.

Metallic orthopedic implants are commonly used in total hip and knee replacements, dental restoration and support material as bone in case of accidents. These metallic implants contain a thin layer of oxide which help to grow tissues and proliferate due to their biocompatibility. However, due to highly corrosive nature of human body and relative motion of implant with bone, wear debris are generated at the implant-tissue interface. The interaction between wear debris and tissue result in the generation of ROS which causes inflammation. Therefore, patient needs a revision surgery after some time. CNPs mitigate the inflammation in cells by scavenging ROS.

Coating of cerium oxide at the implant surface can scavenge ROS produced by the TiO_2-cell interaction and delay the revision surgery. In this chapter, ALD thin films of varying thickness have been grown and their surface chemistry has been analyzed in comparison to CNPs. Mimicking the surface chemistry of CNPs on ALD cerium oxide coatings have many potential application such as anti-inflammatory coatings, sensor platform, catalyst for chemical degradation etc. The bio-catalytic activity of ALD cerium oxide coatings has been tested and correlated with their surface chemistry. Furthermore, ALD grown cerium oxide coatings have been tested to detect H2O2 as a model system to develop sensor platform.

3.2 Materials and method

3.2.1 Film deposition

Cerium precursor tris(i-propylcyclopentadienyl)cerium [$Ce(iPrCp)_3$] was procured from Strem Chemicals, Inc., Newburyport, MA, USA. Analytical grade water (H_2O) was

purchased from Sigma-Aldrich, USA. Water was used as oxidizer during ALD. Cerium oxide thin films were deposited in a Savannah S200 G2 ALD reactor (Ultratech/ Cambridge NanoTech, Waltham, MA, USA) equipped with low vapor pressure delivery (LVPD) kit. Cerium precursor $Ce(iPrCp)_3$ was contained in a stainless steel bubbler. The $Ce(iPrCp)_3$ was evaporated at 135 °C to generate enough vapor pressure for ALD. Bubbler valves and lines were maintained at 145 °C, whereas manifold was kept at 160 °C. This temperature gradient was maintained during the deposition process to prevent the formation of a cold spot in precursor delivery line, the condensation of $Ce(iPrCp)_3$. H_2O cylinder was maintained at room temperature. Ultra-high purity (99.999%) N_2 gas was used as carrier gas to carry the precursor vapors to the reactor chamber. N_2 was also utilized to purge the reactor between the precursor pulses. Cerium oxide thin films were deposited at 275 °C and temperature of the exhaust lines were at 150 °C.

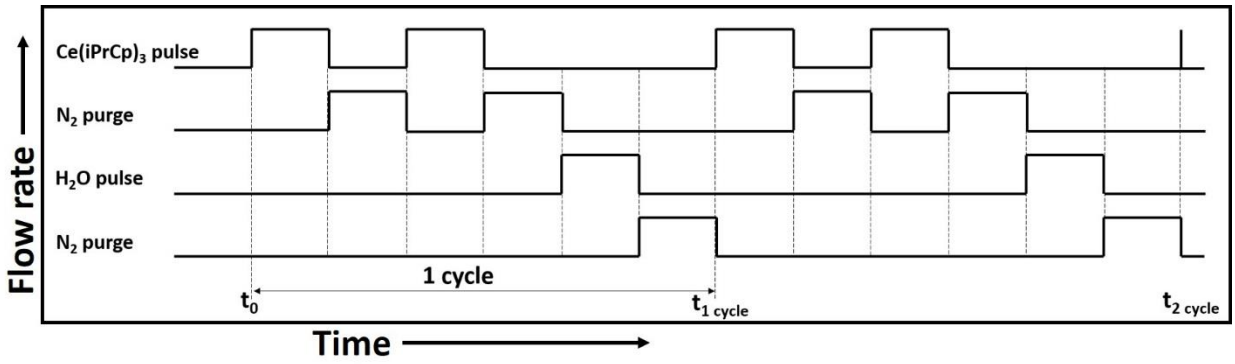

Figure 19: Precursor pulse and purge sequence used for the atomic layer deposition of cerium oxide.

As shown in figure 19, deposition sequence consisted of two consecutive pulses of $Ce(iPrCp)_3$ (exposure time 2.5 sec) a 10 sec purge with N_2, followed by 0.05 sec exposure pulse of H_2O and a final 10 sec purge with N_2. Carrier gas flow was controlled

at 80 sccm by a mass flow controller (MFC). Cerium oxide thin films were grown on silicon (100) substrates.

3.2.2 Film characterization

Ex-situ measurements were performed to determine the film thickness, structure, surface chemistry, and morphology. Film thickness was determined by X-ray reflectivity (XRR) A PANalytical X'Pert³ Materials research Diffractometer (MRD) having Cu-Kα radiation source was employed for XRR. The crystallinity of films was studied using Panalytical Empyrean having Cu-Kα radiation source. X-ray photoelectron spectrometer (XPS) measurements were performed on PE-PHI5400 spectrometer at room temperature in ultra-high vacuum (UHV) chamber (4×10^{-9} Torr) using Al-K_α radiation (binding energy 1486 eV). The spot size of the beam was approx. 4 mm spot size. C 1s peak at 284.6 eV was used as a reference for calibration. Peakfit® software was utilized for deconvolution to identify the oxidation states of Ce (3d), O (1s), and Si (2p). Zeiss Ultra 55 scanning electron microscopy was used to obtain morphology of ALD deposited CeO_x thin films on Si substrate. FTIR spectra were collected to identify the presence of residue of metalorganic Ce precursor using PerkinElmer Spectrum One® spectrometers.

3.2.3 Catalytic activity

Quantitative determination of catalase (CAT) mimetic activity of 50, 200, 500 and 1000 cycle CeO_x samples was carried out using commercially available Amplexs Red hydrogen peroxide assay kit [Invitrogen, Catalog Number #A22188]. A minor modification was done from the standard protocol where the reaction was performed in 1ml quartz cuvette with a total reaction mixture of 1 ml each. H_2O_2 concentration in the reaction mixture was kept at 1 µM and added to initiate the reaction in last. Control and ALD CeO_x

samples were used for the reaction and measurements were performed at 560 nm for a time duration of 20 minutes using the Perkin-Elmer Lambda 750S UV/Visible spectrometer and the data was plotted accordingly.

3.3 Results and discussions

The thickness of ALD grown CeOx films is plotted as a function of number of cycles in figure 20. Film thickness increases with the increase of number of cycles during the process. Thickness of 2, 7, 17 and 33 nm corresponds to 50, 200, 500 and 1000 cycles, respectively. A linear dependence shows the complete self-limiting CeO_x films, a characteristic of ALD process. Self–limiting behavior of films reveal that two consecutive pulse of $Ce(iPrCp)_3$ for 2.5 sec followed by one 50 msec pulse of oxidizer is sufficient to produce CeO_x thin films utilizing low vapor pressure delivery kit (LVPD). Essex et al [93] have deposited CeO2 film using six pulses of $Ce(iPrCp)_3$ per cycle (H_2O as oxidizer) at 250 °C to achieve the complete coverage of substrate. This clearly exemplifies the importance of LVPD kit for the deposition of thin films using precursor having very low vapor pressure. The growth rate of the films calculated from the slope of the line of linear fit is 0.33 Å/cycle. The coefficient of linear fit (R^2) value of 0.9998 shows good linear fit of obtained data. Extrapolation of fitted data shows an intercept of 0.48 nm at y-axis. This could arise from the adsorbed water/Si-OH on the substrate surface.

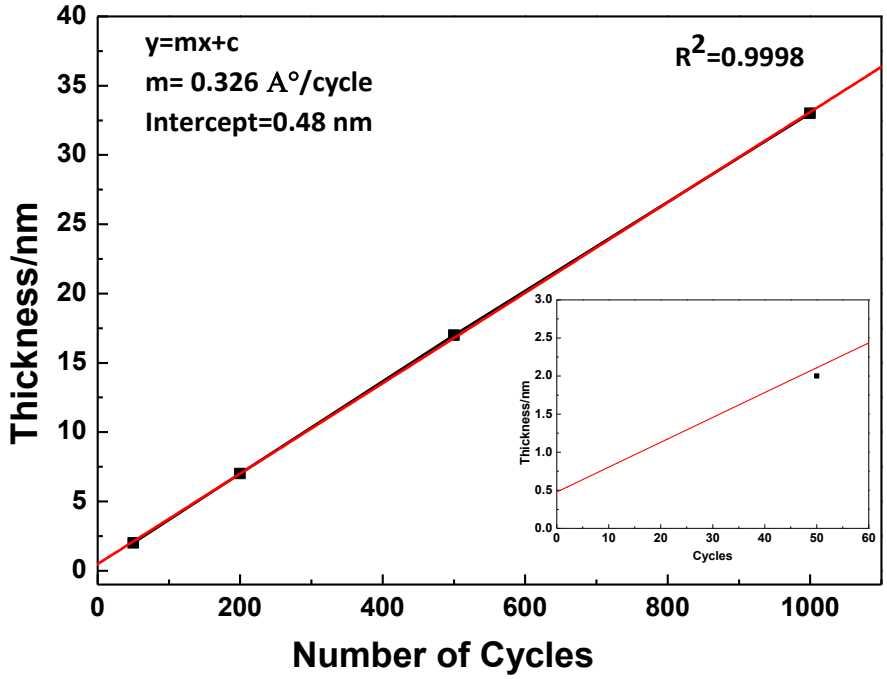

Figure 20: Thickness of CeO_x films as a function of the number of deposition cycles on a Si (100) at 275 °C.

Calculated growth rate (0.33 Å/cycle) is close to the reported values in the literature. Päivsaari *et al.* [94] obtained a growth rate of 0.32 Å/cycle and 0.34 Å/cycle for $Ce(thd)_4$ and $Ce(thd)_3$phne precursors with ozone, respectively. The growth rate of 0.35 Å/cycle has been reported for plasma enhanced (PE)-ALD process where oxygen plasma was used to oxidize the Ce precursor and deposition were carried out at room temperature [90]. During this process, precursor $Ce(iPrCp)_3$ was heated at 135 °C, line temperature was at 145 °C and LVPD (bubble) was used. Comparison of this study to our findings shown that use of oxygen plasma in ALD process can significantly bring down the CeO_2 deposition temperature without compromising growth rate. Another advantage associated with PE-ALD is the lower time required per cycle. However, PE-ALD could not compensate the heating requirement of low vapor pressure precursors.

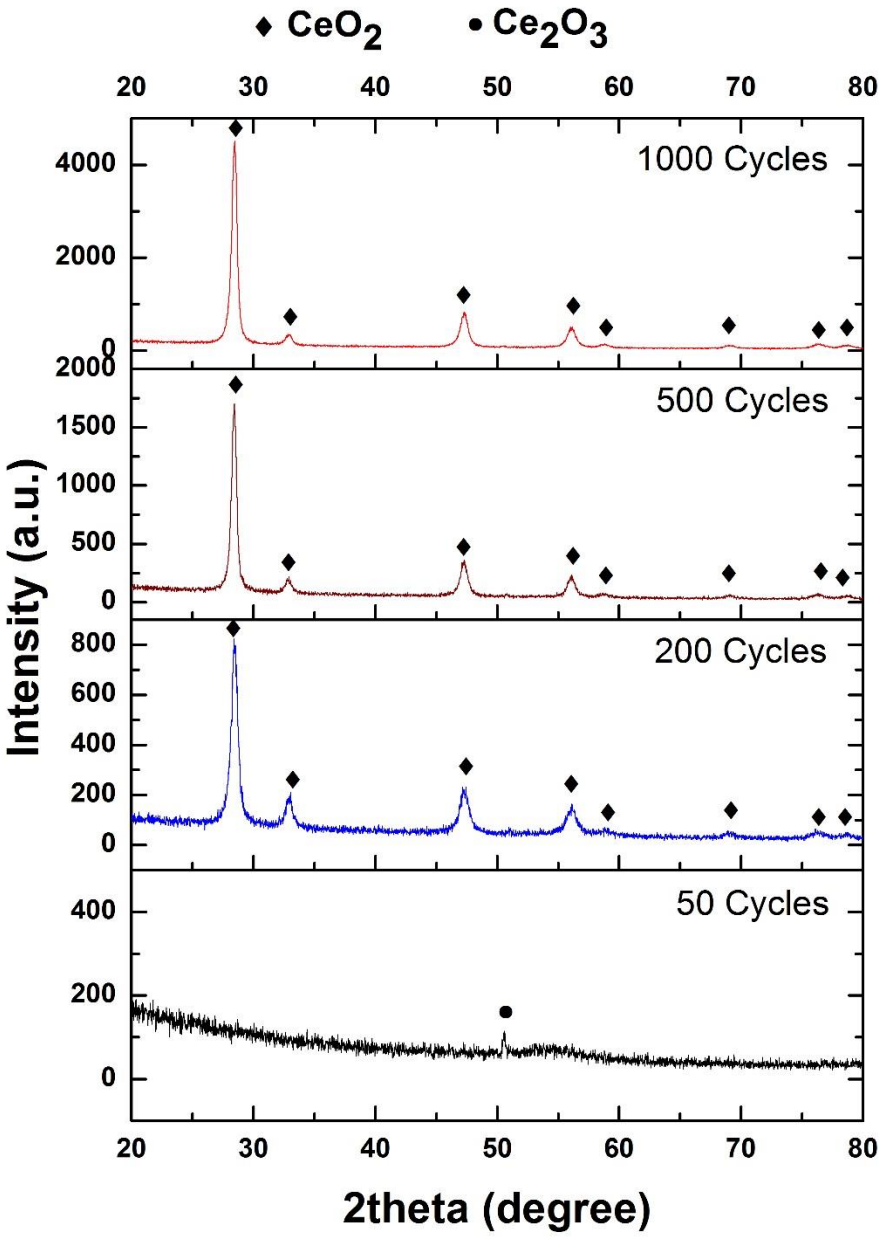

Figure 21: XRD spectrum of CeO_x films deposited for different ALD cycles on a Si (100) at 275 °C.

The crystallinity of deposited ALD CeO_x films was evaluated by XRD and presented in figure 21. Films deposited for 200, 500 and 100 cycles are polycrystalline and clearly exhibiting (111), (200), (220) and (311) peaks of CeO_2. No preferred

orientation was observed in the high deposition cycles films. However, post deposition annealing treatment result in preferred (200) orientation [94, 95]. Films deposited only for 50 cycles appears to be amorphous in nature. For 50 cycle sample, no sharp diffraction are visible except a minor peak at 50.62° (Figure 21, 22). This minor peak corresponds to Ce_2O_3 which has trigonal crystal structure (space group $P\bar{3}m1$). Similar peak of lower intensity is also visible in 1000 cycle sample (Figure 22). Therefore, it can be suggested that Ce_2O_3 phase is also present in high cycle film, but their volume fraction is small. A small amorphous peak at CeO_2 (311) position was also observed in the 50 cycle sample XRD spectrum (Figure22).

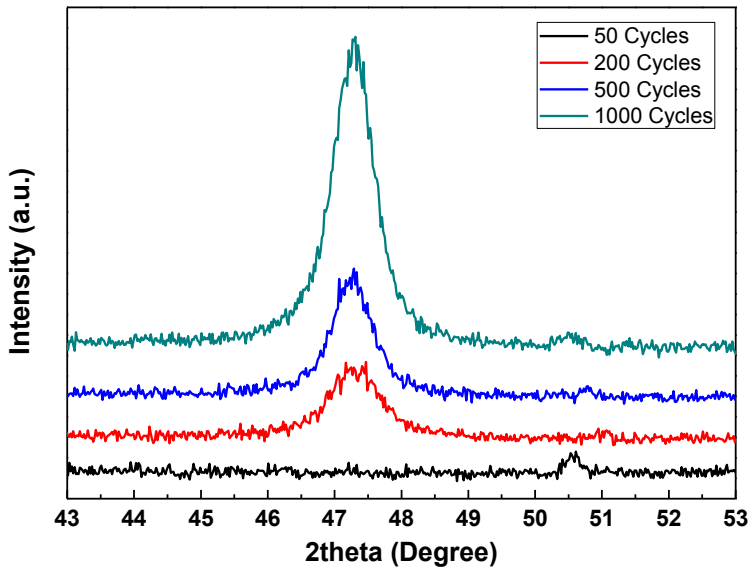

Figure 22: Broader view of XRD spectrum of CeO_x films between 2theta 43-53°.

The transaction from Ce_2O_3 to CeO_2 in 50 cycle sample to 200-1000 cycle samples is due to the stress in the films. It is known that Ce_2O_3 phase is unstable due to the stress in the material. Therefore, Ce_2O_3 convert into CeO_2 phase which is more stable to achieve the minimum energy state/equilibrium state. Thus, it can be suggested that 2-3 nm thin

films have higher residual stress than 7-33 nm thick films. Calculated residual strain in films are 1.23% (200 cycle), 0.91% (500 cycle) and 0.74% (1000 cycle). Therefore, as the film thickness increases residual strain decreases due to the presence of equilibrium phase (CeO_2).

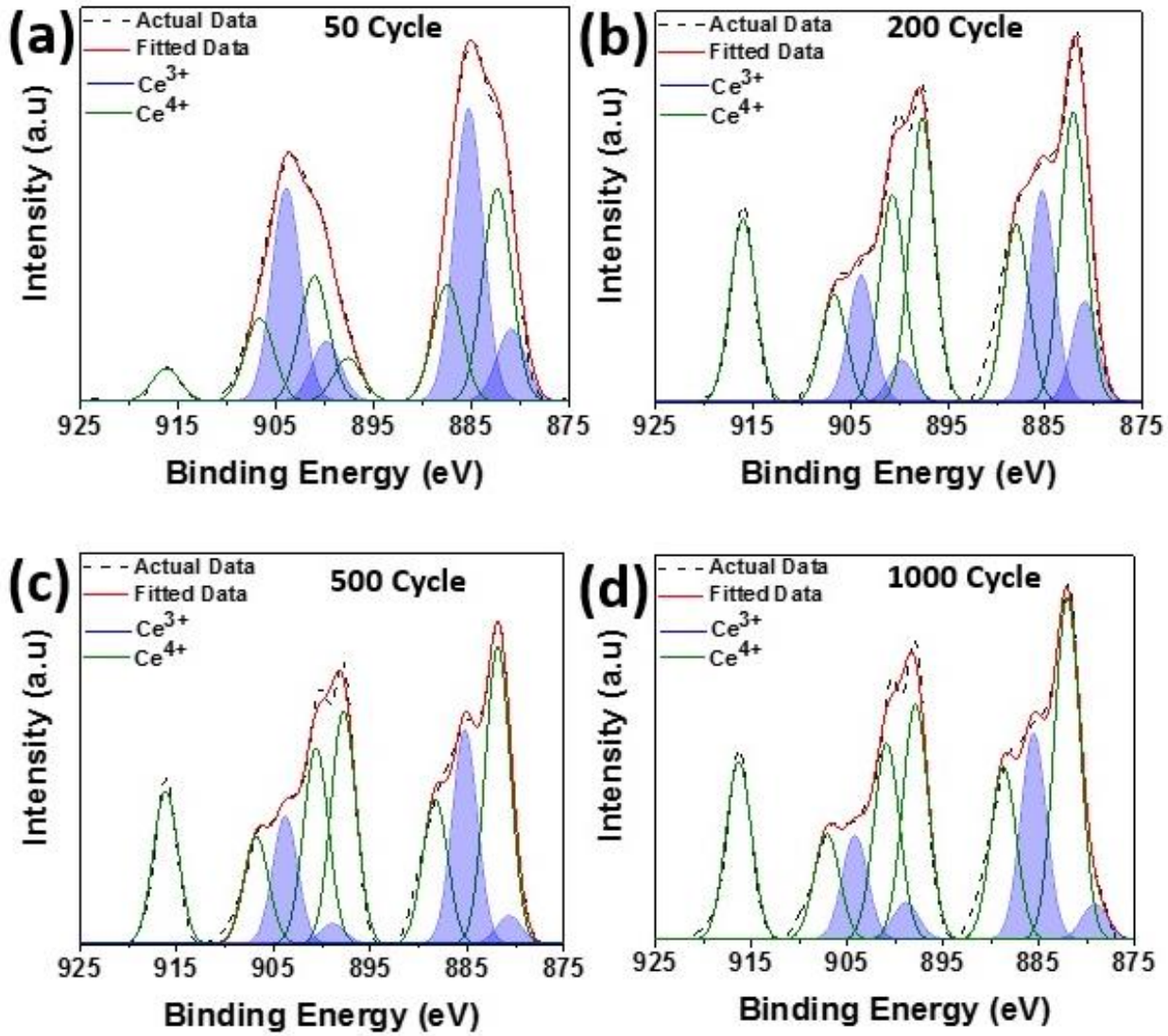

Figure 23: Deconvoluted and fitted XPS spectrum of Ce (3d) taken from different thickness CeO_x films (a) 50 cycles, (b) 200 cycles, (c) 500 cycles and (d) 1000 cycles.

In order to further understand the growth mechanism and effect of no of growth cycles on oxidation state of ALD CeO_x films, XPS studies were performed. Deconvoluted

XPS Ce (3d) spectrum of 50, 200, 500 and 1000 cycle deposited CeOx films are shown in figure 23. Peaks in the Ce (3d) spectrum can be distinguished according to their oxidation states. Peaks v''', v'', v, u''', u'' and u belongs to Ce^{4+} and peaks v^0, v', u^0 and u' belongs to Ce^{3+} [80]. For quantitative analysis of oxidation state of Ce ions in different films, various peaks present in the XPS spectrum which appear due to the $3d_{5/2}$ and $3d_{3/2}$ spin-orbital splitting were peaks fitted with Gaussian distribution. The ratio of the total area under the fitted peak of Ce^{3+} to the total area of all peaks (Ce^{3+} and Ce^{4+}) gives the concentration of Ce^{3+} in films (equation 21, where A_i is the integrated area of peak i). The relative concentration of Ce^{3+} and Ce^{4+} ions on the surface of CeO_x films are presented in table 3.

$$[Ce^{3+}] = \frac{A_{v^0} + A_{v'} + A_{u^0} + A_{u'}}{A_{v^0} + A_{v'} + A_{u^0} + A_{u'} + A_{v'''} + A_{v''} + A_{v} + A_{u'''} + A_{u''} + A_{u}} \quad (21)$$

Table 3: Summary of the surface oxidation state of Ce (3d) from XPS.

Sample	**%Ce^{3+}**	**% Ce^{4+}**
50 cycle	50	50
200 cycle	27	73
500 cycle	25	75
1000 cycle	23	77

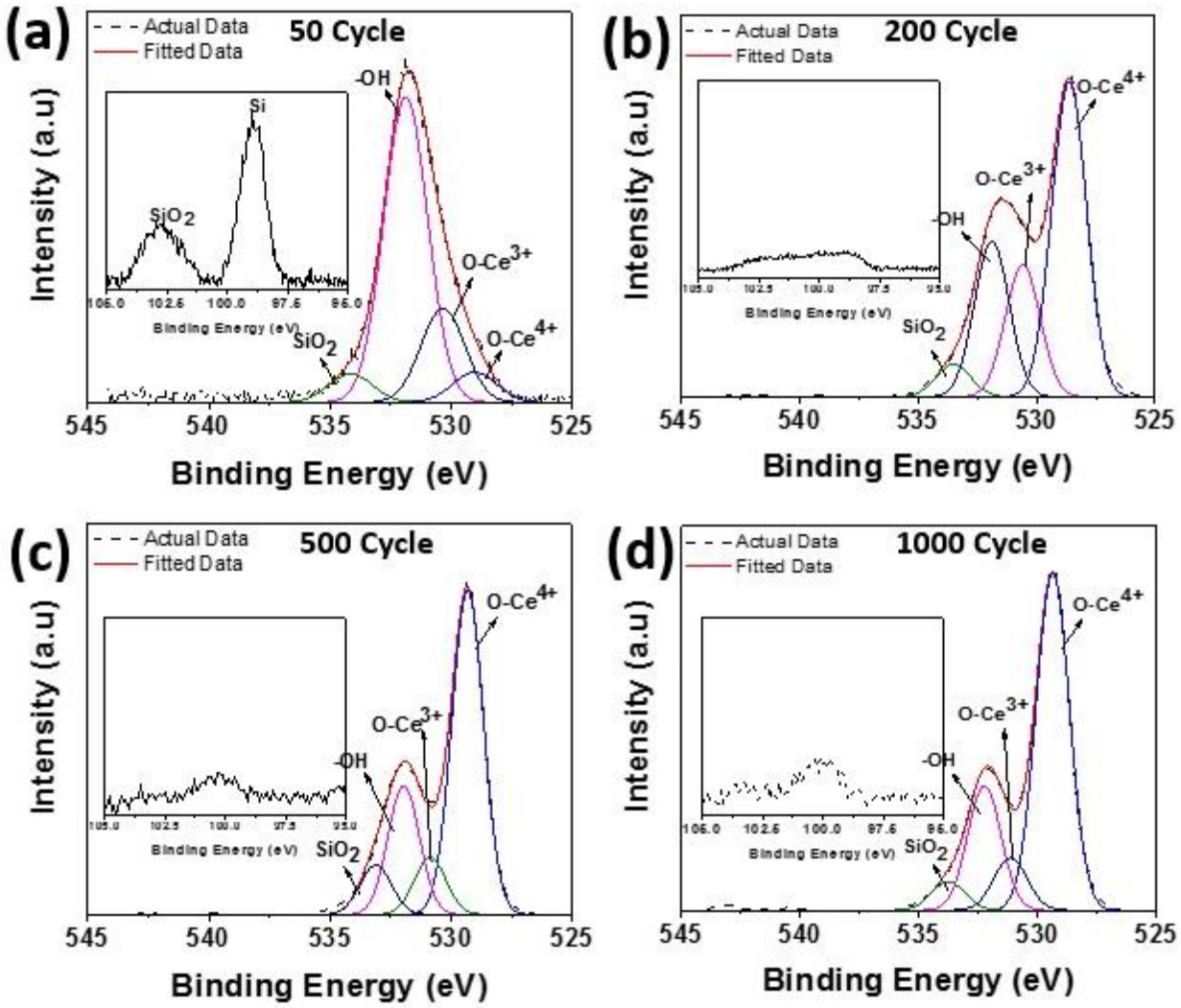

Figure 24: Deconvoluted and fitted XPS spectrum of O (1s) and Si (2p) taken from different thickness CeO_x films (a) 50 cycles, (b) 200 cycles, (c) 500 cycles and (d) 1000 cycles. XPS spectrum of Si (2p) is shown in inset of O (1s) spectrum.

XPS analysis shows that highest concentration (50%) of surface Ce^{3+} ions is present in 2 nm CeO_x film. Surface Ce^{3+} ion concentration drops sharply from 50% to 27% for 7 nm CeO_x film and remains in the range of 23-27% range for high cycle samples (17 and 33 nm thickness samples). This change in surface Ce^{3+} concentration is also visible in XPS spectrum. Peak at 916 eV in the Ce (3d) XPS spectrum corresponds to

Ce^{3+}.Thus, any change in the intensity relative to other peaks provides qualitative information of different oxidation state. The intensity of the peak at 916 eV is significantly lower for 50 cycle CeO_x film compared to the rest of the high cycle CeO_x films. To maintain the charge balance, substitution of one Ce^{4+} ion from cerium oxide lattice by Ce^{3+} creates two oxygen vacancies in the lattice. Therefore, it can be stated that 2 nm thick CeO_x films have 50% oxygen lattice vacancies because x-ray photoelectrons emit only from 4-5 nm depth of the samples. Since the thickness of the sample is only 2 nm, XPS can provide the exact chemical composition in the present case. This was verified by collecting the Si (2p) spectrum presented in figure 24.

Peaks of SiO_2 and Si (2p) are present only in 50 cycle sample because of its 2 nm thickness. No peaks of Si (2p) and SiO_2 were observed in 200, 500 and 1000 cycle samples because the thickness of films is higher than the depth of photoelectron emission. Furthermore, very high intensity –OH peak is observed in deconvoluted O (1s) spectrum of 50 cycle sample. Whereas, the intensity of –OH peak is relatively similar for 200, 500 and 1000 cycle samples (Figure 24). Higher intensity of O-Ce^{3+} peak in O (1s) spectrum collected from 50 cycle sample is higher than O-Ce^{4+} peak. Contrary to this, O-Ce^{4+} peak is more intense than O-Ce^{3+} peak in case of 200, 500 and 1000 cycle samples (Figure 24). This further support our claim of ~50% oxygen vacancies in 2 nm thick CeO_x films. This finding is in good agreement with the calculated surface Ce^{3+} concentration.

The presence of –OH, O-Ce^{3+} and O-Ce^{4+} peaks also provide valuable insight of CeOx film formation and its transaction from Ce^{3+} rich surface to Ce^{4+} rich surface. During the ALD process, Ce precursor reacts with the hydroxyl groups present on the substrate, liberating i-propylcyclopentadienyl molecule. The reaction is self-limiting as the Ce

precursor does not react with adsorbed Ce species. Unreacted precursor and liberated i-propylcyclopentadienyl removed from the reactor by a carrier gas (N_2). In the next step, H_2O reacts with i-propylcyclopentadienyl groups on deposited Ce atoms forming both Ce-O-Ce bridges and new hydroxyl groups which prepare the surface for the next layer deposition. Thus, both Ce-O-Ce and -Ce-OH form on the surface. In typical CeO_2 synthesis process, first cerium hydroxide ($Ce(OH)_3$) form, which further oxidizes and converts into CeO_2. The presence of strong –OH peak in O (1s) XPS spectrum indicates that in the ALD CeOx deposition, $Ce(iPrCp)_3$ precursor reacts with H_2O and form $Ce(OH)_3$ which further convert into Ce_2O_3 and CeO_2 with increasing ALD cycles. Also, amorphous to crystalline transformation occur as indicated by XRD analysis. Therefore, presence of minor crystalline Ce_2O_3 and amorphous peak in XRD of 50 cycle sample appears to be in amorphous to crystalline transition. Minor impurities in films have been detected from FTIR (Figure 25). RBS experiment in ongoing to measure the exact composition of films.

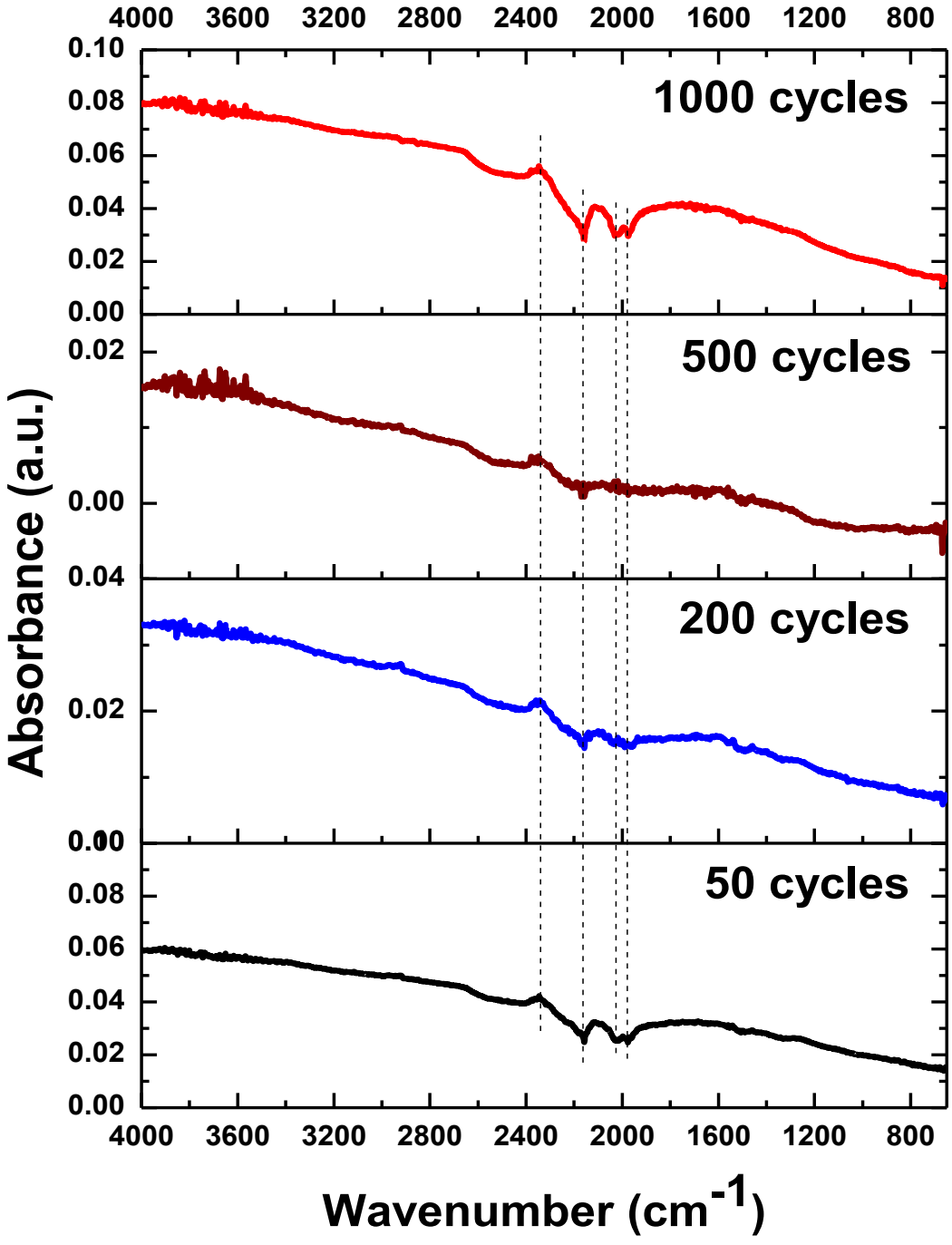

Figure 25: FTIR spectra of CeO_x deposited for different ALD cycles.

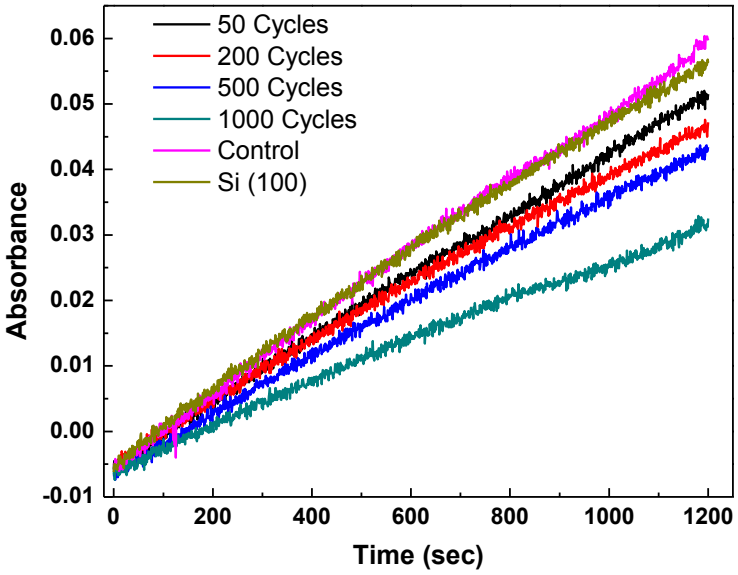

Figure 26: Thickness dependent catalase mimetic activity of ALD CeO_x films.

Bio-catalytic properties of ALD grown CeO_x films have been evaluated in the form of catalase mimetic activity. It is evident from figure 26 that 1000 cycle sample has highest catalase mimetic activity and it decreases with reduced number of deposition cycles. In other words, catalase mimetic activity of CeOx films decreases with increasing surface Ce^{3+} concentration. 1000 cycle sample has only 23% surface Ce^{3+} concentration, whereas 50 cycle sample has 50% Ce^{3+} at the film surface. It is reported in the literature that bio-catalytic properties of CNPs prepared by different methods is Ce^{3+}/Ce^{4+} dependent [3]. Higher Ce^{3+}/Ce^{4+} CNPs have SOD mimetic and OH* scavenging activity. Lower Ce^{3+}/Ce^{4+} CNPs have catalase (H_2O_2) mimetic and NO* scavenging activity. Our catalase results seem to be in good correlation with the previous reports. Additionally, catalase results exhibit the mimicking of catalytic behavior of CNPs in ALD CeOx sample prepared by ALD at 275 °C.

ALD-prepared CeO_x electrodes were characterized in presence of H_2O_2. The relevance of this interaction comes from the prevalence of H_2O_2 as a product of free radicals in the body which accumulate in instances of pathology (i.e. concentration correlates with progression of disease states such as cancers, diabetes, neurodegenerative diseases). Cyclic voltammetry (CV) was performed to characterize the electrochemical behavior of ALD CeO_x in presence of H_2O_2. Voltammetry was performed at 50 mV/s and in the range of (-0.3) to (0.7) V. This range was specifically chosen to prevent signals from hydrolysis (oxidation at ~ -0.32 V and reduction at ~0.8 V). Measurements show (Figure 27) an increase in reduction current at -0.3 V in presence of H_2O_2 and a positive correlation between concentration and current. This observation is supported by other findings in related works [96, 97] and represents the reduction of peroxy groups at the surface of CeO_x. To be certain that the observed peak is characteristic of H_2O_2 reduction at surface sites and not from elaborate surface reactions or Galvanic responses: CV was performed at varying scan rates. The trend in current increase with increasing scan rate suggests that the response is diffusion limited (Figure 28). Inputting these values in the Randles-Sevcik equation confirms this behavior. However, absence of an obvious corresponding oxidation peak suggest that this reaction is irreversible. This determination is reasonable given the radical nature of the H_2O_2 analyte (i.e. relatively low stability, high reactivity). In order to use ALD CeO_x electrodes as biosensors, the described electrochemical reaction must produce a consistent signal response in presence of specific concentrations of analyte. However, CV is not appropriate for these analyses. Therefore, chronoamperometry (CA) was utilized at (-0.3) V, per the observed electrochemical response in CV.

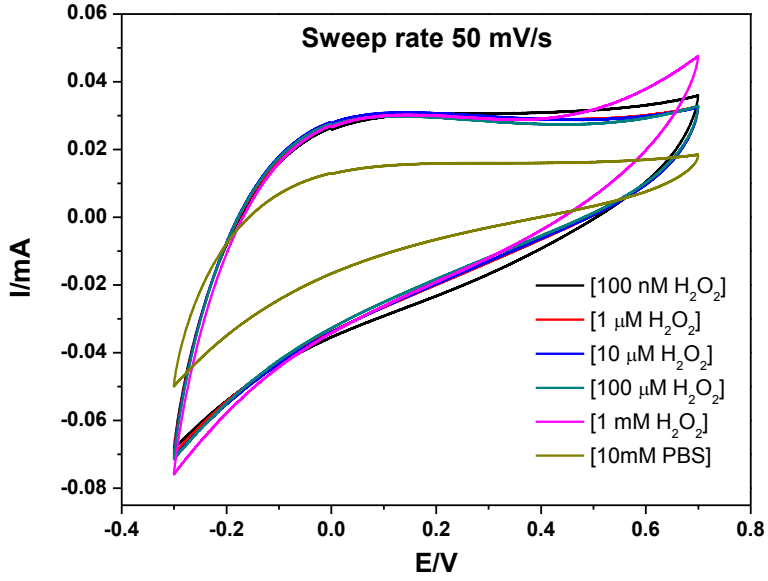

Figure 27: Cyclic voltammograms response of 200 cycles deposited ALD CeO_x electrode in 10 mM PBS electrolyte at 50 mV/sec scan rate with varying [H_2O_2].

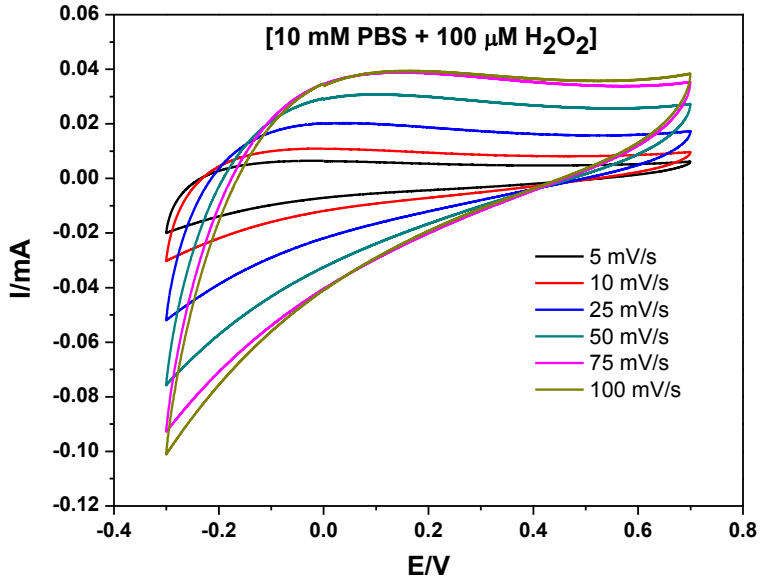

Figure 28: Cyclic voltammograms response of 200 cycles deposited ALD CeO_x electrode in [10 mM PBS and 100 µM H_2O_2] with varying scan rate.

Chronoamperometry (CA) was performed by applying a constant potential and spiking the test solution with known concentrations of H_2O_2 under N_2 gas purging to mix the test solution. Current response was immediate (time of response ~8 s; time from addition of analyte to equilibration of current signal baseline), following addition of analyte. Additionally, current response was reliable (mean response for 10nM: 0.420 µA, SD: 0.0464 µA) (Figure 29). Addition of different concentrations of H_2O_2 shows increasing current with increasing analyte concentration. The sensitivity of this measurement was determined to be 9.04 A*L/g*cm^2*s based on current response. Further, the limit of quantitation (LOQ) was determined to be ~1 pM using CA. This value was determined using the conventional description,

$$LOQ = (\text{Root Mean Square of Blank current}) + 10\,\sigma_{RMS}, \text{Blank} \quad (22)$$

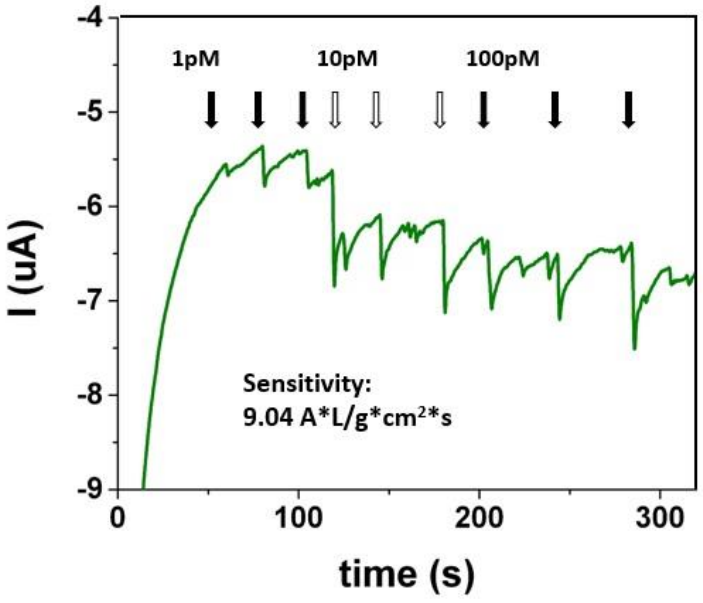

Figure 29: Chronoamperometric response of 200 cycle deposited ALD CeO_x electrode towards H_2O_2 in 10 mM PBS electrolyte.

This value is highly significant, as disease states can be detected at very early stages as well as in small/dilute samples of bio-fluid. This sensor is several orders of magnitude below that of the reviewed sensors: both enzymatic and inorganic-based sensors (Chapter 4, table 4). Ceria has been showingn elsewhere to be highly specific towards reactive oxygen species [63, 64, 98, 99]. In recent study, we have shown that none of glucose, nitrite, nor uric acid interfering species elicit current signals from the ceria sensor [97]. These results speak to the high degree of selectivity posed by the sensor. Use of an inorganic oxide thin film, CeO_x, as the detection element of the sensor allows for a highly robust device/detection. Ceria is largely insensitive to heating and will not lose activity as enzymes do when exposed to varied conditions.

3.4 Conclusions

Cerium oxide thin films were successfully deposited on Si (100) substrates using $Ce(iPrCp)_3$ and H_2O as a precursor for different ALD cycles. Linear relation relationship between thickness and deposition cycles indicate the self-limit character of ALD process. The calculated growth rate was 0.33 Å/cycle. XRD results indicate that Ce_2O_3 phase nucleate initially which convert into CeO_2 phase with time due to high temperature in the reactor chamber. Therefore, only CeO_2 phase was present in higher thickness coatings. XPS analysis of Ce (3d) shows the increase of surface Ce^{4+} ion as the thickness increase. The relative ratio of the deconvoluted peak of oxygen corresponding to Ce^{3+} and Ce^{4+} ions from XPS O (1s) spectrum support the change in Ce^{3+} to Ce^{4+} ratio with increasing thickness. Excellent catalase mimetic activity was measured for lower Ce^{3+}/Ce^{4+} CeOx films exhibiting the mimicking of nanoparticle behavior in CeO_x films as a function of its thickness. Limit of quantitation (LOQ) was determined to be 1 pM for H_2O_2 analyte from

chronoamperometry using CeO_x. Therefore, ALD CeO_x films have the potential to be utilized as a coating on implants to mitigate inflammation.

CHAPTER FOUR: MOLYBDENUM DISULFIDE BASED ELECTROCHEMICAL SENSORS

The work presented in this chapter has been published before in

2D Materials, 2017.

Reproduced by permission of The Institute of Physics.

4.1 Introduction

Antioxidants are essential to the human body for keeping the concentrations of pro-oxidants under control. Pro-oxidants are generated in the human body as a by-product of various biochemical reactions essential to metabolism. The pharmaceutical industry has long shown an interest in the effects of light exposure and storage conditions on the state of pharmaceuticals. Of particular interest is the evolution and measurement of free radicals. Free radicals, specifically reactive oxygen species (ROS) and nitrogen species, possess strong electron affinity and therefore have a tendency to gain electrons from neighboring molecules/cell membrane to achieve stable electron configurations. This process continues until interrupted by antioxidants which donate/take electrons to neutralize radicals. However, an unbalance between the production of pro-oxidants and antioxidants in cells could lead to the accumulation of ROS like superoxide ($O_2^{\bullet -}$), hydrogen peroxide (H_2O_2) and nitric oxide (NO^*) species. resulting in significant cellular damage. Alzheimer's disease, cancer, aging, fibrosis, inflammation, and multiple sclerosis are a few conditions related to oxidative stresses generated by free radicals [98, 100, 101]. However, cells also produce pro-oxidant molecules which protect against bacterial infection. Myeloperoxidase (MPO) is released by neutrophils during oxidative burst and can also produce oxidative stress. When MPO combines with H_2O_2 and a

chlorine ion (Cl^-), it generates hypochlorous acid (HOCl) in the cells. HOCl is a short-lived and powerful diffusible oxidant, strong oxidizer and could react with O^{2-} to produce hydroxyl radicals (OH^*). Therefore, in physiological condition, HOCl has a major role as a potent microbicidal agent in the immune defense. However, during the oxidative burst, HOCl not only attacks cell components, it also generates extremely reactive radicals. Therefore, monitoring of the production of free radicals at the cellular level is very important for diagnostic purposes.

Over the past years, several methods such as use of fluorescence probes [8-10], colorimetric assays [11, 12], electrochemical methods [13-17], spectrometry [19], and cell imaging coupled with Raman spectroscopy [20], have been developed to detect free radicals. Detection limit, time and cost are vital factors in today's scenario of affordable health care, pharmaceuticals and drug delivery application. Almost all methods mentioned above are time consuming, costly and their detection limits are well above the cellular-level of free radical species generation except via electrochemical methods. Electrochemical methods seem viable because of their low-cost set-up and fast response time [26, 102]. However, most of the current commercially used electrochemical sensors are enzyme based. For example, glucose and hydrogen peroxide sensors utilize glucose oxidase and horseradish peroxidase, respectively. These enzymes are costly and temperature- and pH- sensitive; thus, their activity and consistency varies significantly with geographical locations. Furthermore, the shelf life of these sensors is limited due to their strict temperature requirements. To overcome these shortcomings, several inorganic materials have been used to develop sensors for free radical detection such as cerium oxide nanoparticles (CNPs) [32], precious metal (gold and platinum) nanoparticles [13,

24, 25], and molybdenum disulfide (MoS_2) nanosheets and nanoparticles [26]. However, detection of free radicals at the cellular level is still challenging. Over the past years, some inorganic materials have been demonstrated to possess enzyme-mimetic behavior, such as CNPs [59, 98], V_2O_5 [36] etc. This enzyme-mimetic behavior has made them attractive choices because of their temperature-independent function which exists over a large range of temperature, a wider operating pH range, and longer shelf life.

Discovery of single layer graphite called graphene has opened up new possibilities for materials scientists in the fields of electronics, sensing, corrosion protection etc.; and have led to the rise of a new class of "two-dimensional (2D) materials". MoS_2 is one of the more promising materials in this class. It has unique electronic, optical and chemical properties similar to graphene. However, modulation in the band gap of MoS_2 from metallic to semiconductor compared to graphene (no band gap) and 2D oxides (large band gap), offers sensitivity and selectivity for a wide range of devices/biomolecules in biosensing performance [103, 104]. MoS_2 has been functionalized with thiols, silanes, and amides resulting in the creation of surface dipoles and charge displacement. Additionally, two thiol groups can couple and form RSSC bonds which can be used to immobilize a wide variety of proteins [104]. These proteins further interact with –SOH group containing compounds which are used for biocatalysis and biosensing [104]. For bio-analyte detection, various types of field effect biosensor configurations without a reference electrode (nonspecific binding [105] and lock-and-key concept [106]); and with a reference electrode (introduce electrical double layer and intercalation) have been studied using 2D MoS_2 acting as a transducing layer between drain and source. 2D MoS_2-based field-effect biosensors have been employed along with/out microfluidic

channels to sense antigens (picomolar detection) [106] , proteins (femtomolar detection) [107], single strands of DNA (10 fmol detection limit) [108], DNA mutations (Alzheimer's disease; nanomolar level detection) [109], glucose [26] and dopamine [102]. Recently, MoS_2/Au microcubes have been prepared from hydrothermal method and utilized for ultra-low detection of microRNA-21 (detection limit 0.086fmol) [110]. This electrochemical biosensor has showed high selectivity towards microRNA-21. Wang et al. [26] have shown the effectiveness of MoS_2 particles in the nanomolar level detection of H_2O_2 via the electrochemical method. To the best of our knowledge, no study has been performed on other free radicals such as NO^* detection using MoS_2. Several composite materials based on 2D MoS_2 and $MoSe_2$ such as MMNT/MoS_2 [111] and Ni foam-$MoSe_2$/acetylene black [112] have been studied for hydrogen evolution and supercapacitor applications. Ni foam-$MoSe_2$/acetylene black composite has demonstrated fast charging and slow discharging behavior in comparison to Ni foam-$MoSe_2$ tested over 1000 cycles. Specific capacitance, Tafel slope and overpotential of 2020 F g^{-1} at 1 A g^{-1}, 55 mV dec^{-1} and 80 mV have been reported [112]. In case of MWNT/MoS_2 composite, specific capacitance of 452.7 F g−1 at 1 Ag^{-1} have been achieved and small reduction of 4.2% after 1000 cycles [111]. The reported specific capacitance is higher than MWNT (69.2 F g^{-1}) and MoS_2 (149.6 F g^{-1}). These studies exhibit the wide range of applications of MoS_2 in biosensing and energy storage field.

The present study focuses on understanding/unfolding the size dependency of MoS_2 for free radical detection by electrochemical methods and theoretical modeling by means of density functional theory (DFT). This study also shows the development of a multi-role electrochemical sensor demonstrating ultra-low detection of free radicals;

namely, H_2O_2, HOCl and NO^*. We have successfully measured H_2O_2 and HOCl in pico-molar concentrations and NO^* at nano-molar concentration. To gain fundamental insights into the catalytic activity of MoS_2 nanosheets, we have applied DFT to understand the subtleties of the system electronic structure and to calculate the adsorption energy of H_2O_2 at the edges of stoichiometric and sulfur-deficient MoS_2 particles.

4.2 Materials and method

4.2.1 Thin glassy carbon preparation

Thin glassy carbon electrodes were prepared from 8 wt.% polyacrylonitrile (PAN, M_w 150,000) polymer solution as per earlier reports [113, 114]. PAN polymer powder was dissolved in dimethylformamide (DMF) at 40°C and kept at this temperature for 30 min. One-side polished silicon wafer was cut into small pieces and cleaned via ultrasonication in acetone, followed by ethanol and water. Cleaned Si wafers were dried under inert atmosphere (N_2 gas). PAN solution was spin-coated on cleaned Si wafers at 3000 rpm for 30 sec to evenly coat PAN and achieve a uniform thickness. These PAN-coated Si wafers were later heat-treated at 250^0C for 1 hr to stabilize followed by carbonization at 900 ^{0}C for 1 hr under inert atmosphere (Ar, flow rate 150 mL/min). Heating and cooling rate were maintained at 5 C^0/min. A schematic representation of preparation method is shown in figure 30.

4.2.2 MoS_2 preparation and their size sorting

Commercially available MoS_2 powder (99.00% pure, size ~2μm) was purchased from Sigma-Aldrich, USA and used without further purification. DMF was used as a solvent to exfoliate MoS_2 because its surface tension is similar to the surface energy of MoS_2 which makes exfoliation of MoS_2 easy and effective [26, 103, 115]. 1 mg/mL MoS_2

was dispersed in DMF and sonicated using horn sonicator for 4 hrs (see Figure 31). This process was carried out in an ice bath to avoid agglomeration of MoS_2 due to heat and evaporation of DMF to maintain uniform concentration. Exfoliated MoS_2 sheets and particles were sorted using differential centrifugation at 1000, 3000, 6000 and 12000 rpm. After each centrifugation step, the precipitate was collected and resuspended in DMF and supernatant was used for next centrifugation process.

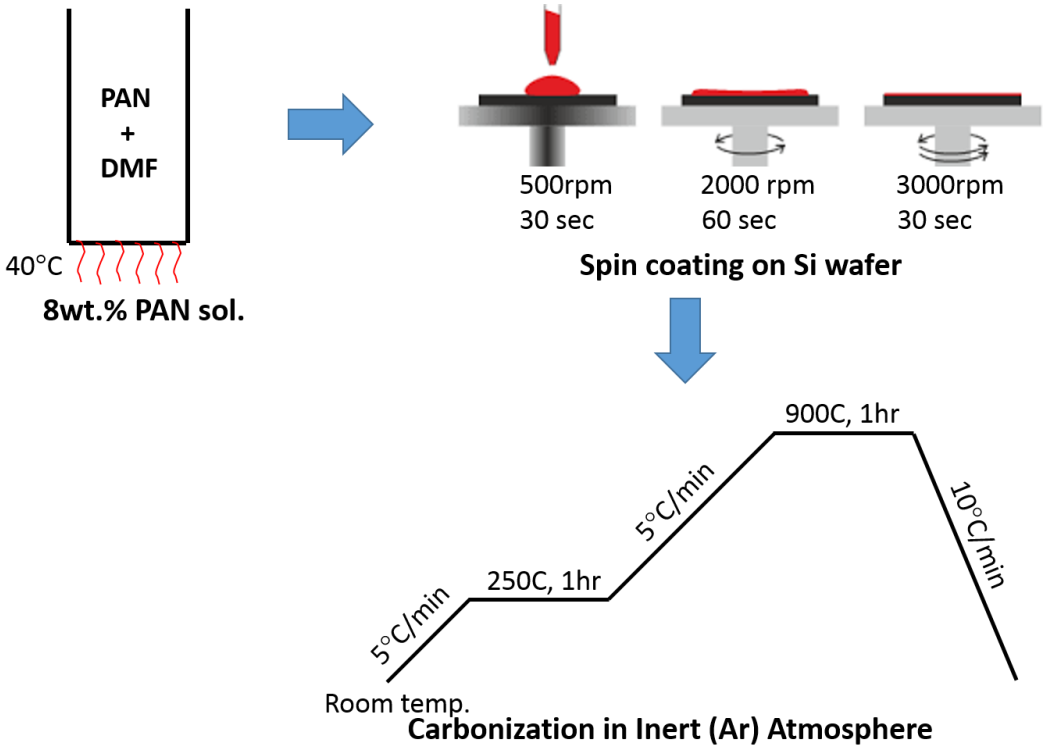

Figure 30: Schematic of synthesis procedure adapted for the preparation of thin glassy carbon. The process includes three steps i.e. (i) dissolving PAN in DMF, (ii) spin coating of PAN solution and (iii) carbonization of spin coated substrates in inert atmosphere.

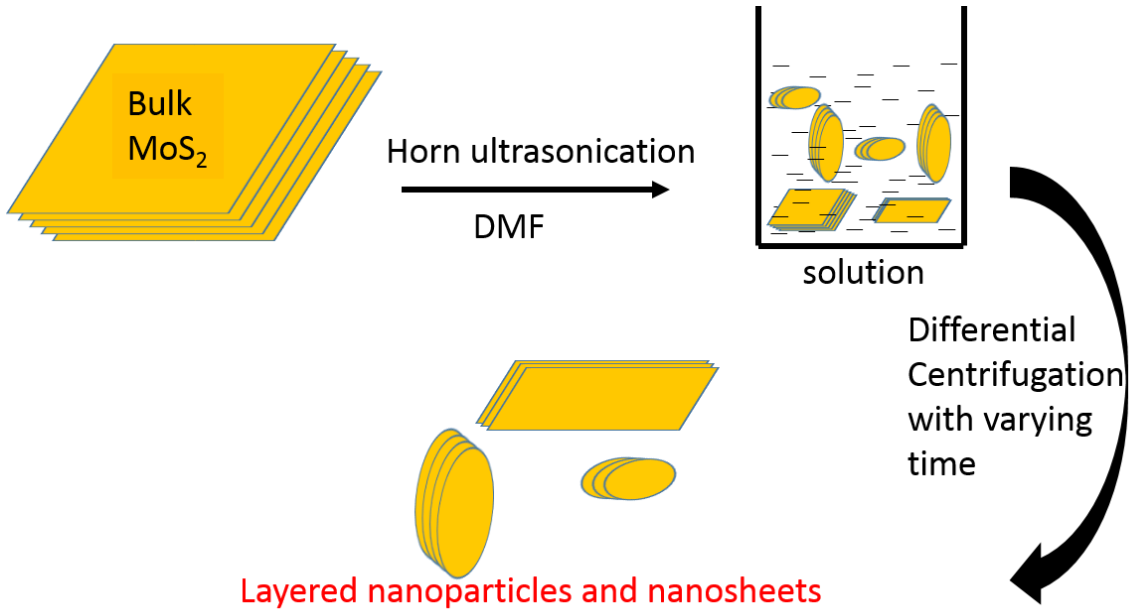

Figure 31: Schematic of exfoliation process and size sorting of MoS_2 nanoparticles and nanosheets. Liquid exfoliation has been carried out in DMF using horn sonicator. Differential centrifugation has been applied to collect MoS_2 nanoparticles and nanosheets of different size.

4.2.3 Biosensor fabrication and modification

To fabricate biosensors, 25 µL of MoS_2 in DMF solution were drop-cast on thin glassy carbon and kept under vacuum for drying. A Nafion® film was used to prevent the detachment of MoS_2 from thin glassy carbon/Si substrate. Electrical connection between glassy carbon and copper wire was made by applying silver paste at the corner. This biosensor was rinsed in deionized water and dried at room temperature under ambient conditions. Biosensors were stored in vacuum desiccator when not in use.

4.2.4 Characterization of size sorted MoS_2 and thin glassy carbon

All size-sorted MoS_2 were characterized by X-ray photoelectron spectroscopy [XPS, Physical Electronics (PHI5400 ESCA)] with a monochromatic Al Kα X-ray source

at 300 W with a base pressure of $5x10^{-8}$ Torr to determine the S to Mo ratio. UV-Vis spectroscopy was conducted at 1 mM concentrations using Perkin-Elmer Lambda 750S spectrometer. A FEI Tecnai F30 high-resolution transmission electron microscope (HRTEM) operating at 300 keV was utilized to confirm the crystalline nature and to determine particle size and morphology of different MoS_2. Zeiss Ultra 55 scanning electron microscopy was used to obtain morphology of drop-cast MoS_2 on thin glassy carbon. Renishaw RM 1000B micro-Raman spectrometer was used to confirm the structure. XPS, Raman spectroscopy and cyclic voltammetry (CV) were also conducted on thin glassy carbon to confirm and compare its physical and chemical properties with commercial glassy carbon.

4.2.5 Electrochemical measurement

Three electrode system was used for electrochemical measurements. A schematic diagram of experimental set-up has been presented in figure 32. Ag/AgCl electrode and Pt mesh were used as a reference electrode and the counter electrode, respectively. MoS_2/thin glassy carbon acted as the working electrode for detection. All potentials are referred against Ag/AgCl electrode. All electrochemical measurements were carried out on Bio-Logic SA VSP (Princeton Applied Research) at room temperature. Prior to any experimental measures, the Pt mesh electrodes were electrochemically cleaned by cyclic voltammetry in 0.5M H_2SO_4 and the potential range was swept between 1.6 and -0.5V vs. the reference for 50 cycles at 1000mV/s. Electrochemical measurements were performed in N_2 saturated 10mM phosphate buffer saline (PBS) solution unless otherwise mentioned. H_2O_2 and NaOCl solutions were procured from Sigma-Aldrich, USA and diluted with 10mM PBS solution to obtain the desired concentration. Experimental cyclic

voltammetry was performed at different potential range vs. reference for each different free radical solution at a constant sweep rate of 25mV/s. The sensitivity of the biosensor was evaluated using chronoamperometry and free radical solutions were added in 100µL increments every 30-60 seconds.

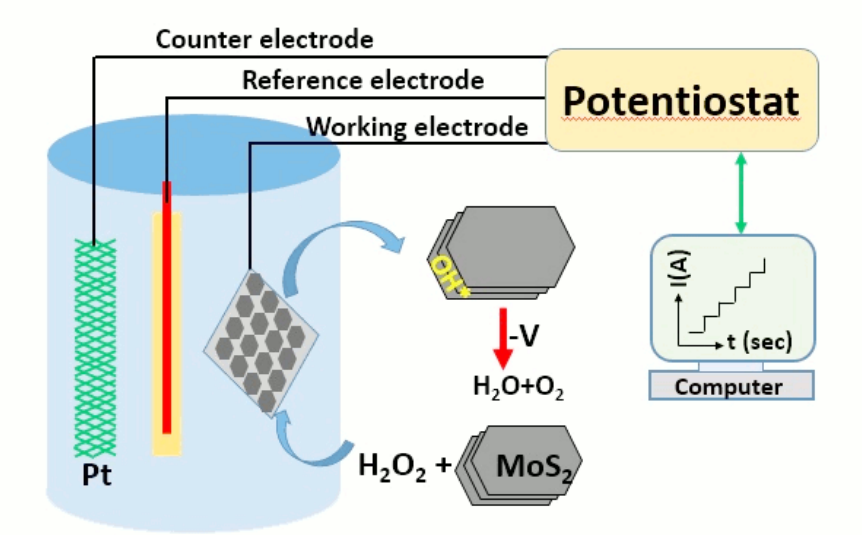

Figure 32: The experimental set for electrochemical detection of free radicals. MoS_2 drop-cast thin glassy electrode as working electrode and Pt mesh as counter electrode were used during experiment. External potential was applied using potentiostat connected to the computer for data processing.

4.2.6 Computational methods

Density functional theory (DFT) calculations were performed using the Vienna *ab-initio* Simulation Package (VASP) [116, 117]. Projected-augmented wave [118, 119] technique, and generalized-gradient approximation (GGA) in the form of Perdew-Burke-Ernzerhof (PBE) [120] functional were employed to describe ion-electron interaction, and exchange–correlation interaction between electrons, respectively. In our calculations, van der Waals interactions were also taken into account using DFT-D3 approximation [121].

To avoid the spurious electrostatic interaction between nanoparticles (NPs), we placed NPs in the center of the large supercell to ensure the sufficient separation (20 Å) between periodic images along all three (x, y, z) directions. Nanoparticles of several sizes (Mo_xS_y, where x=12, y=24; x=27, y=48 or 54; x=48, y=96; and x=75, y=150 represent the number of respective atoms in the NP) were constructed from the calculated bulk MoS_2 structure (of which lattice parameter (a=3.16 Å) agrees with the experiment [122]). For the calculations of the total energy of all considered systems the Γ point was used to sample the Brillouin zone. The kinetic energy cutoff for the plane-waves expansion was chosen to be 500 eV. All atom positions were fully relaxed using the conjugate-gradient algorithm [123, 124] until the total energy converged to 10^{-5} eV and the forces acting on each atom reduced to less than 0.01 eV/Å.

4.3 Results and discussions

4.3.1 Experimental results

4.3.1.1 Characterization of glassy carbon electrode

The pyrolyzed thin films obtained from PAN are amorphous in nature as confirmed by XRD spectrum [Figure 33(a)]. A large, wide peak provided clear evidence of short-range ordering in the pyrolyzed PAN films. The raw Raman spectrum shows two peaks appearing belong to D and G bands of carbon, however the asymmetric nature and broad peaks suggested the presence of other peaks. De-convoluted Raman spectrum of amorphous film shows four distinct peaks centered at 1223, 1378, 1480 and 1586 cm^{-1} [Figure 33(b)]. The peak at 1223 cm^{-1} corresponds to nanocrystalline diamond formed during carbonization treatment [125] as discrete nanopockets of crystalline diamonds. Another peak at 1480 cm^{-1} belongs to the disordered sp^3 carbon. Peaks at 1378 and 1586

cm^{-1} correspond to disorder induced peak of graphite lattice vibration mode with A_{1g} symmetry, and the graphite lattice vibration mode with E_{2g} symmetry, respectively [113, 125-127]. The background corrected intensity ratio of I_D to I_G for amorphous carbon electrode is 0.92. These peaks are in good agreement with the conventional glassy carbon pyrolyzed at identical temperature [113, 125, 128]. Thus, these amorphous films will be termed glassy carbon film in the present article afterward. XPS survey taken from the film have shown the presence of C, O and N, the main chemical elements present in the PAN [Figure 33(c)]. The amount of N is very similar (6.58 at.%) in our glassy carbon film as compared to the other reported values (6.28 at.%) for PAN derived carbon film at 900°C [129]. The deconvoluted 1s carbon peak is also presented in figure 33(d). Peaks at 284.4 eV, 285.3 eV, 286.1 eV, 287.1 eV, 288.1 eV, 288.7 eV and 289.9 eV belong to C-C (sp^2), C-C (sp^3), C-O, C-N, C=O, C≡N, and -C(O)-OH, respectively [130-132]. C-N and C≡N peaks are observed due to the presence of residual N. The SEM micrograph in figure 33(e) shows the porous nature of glassy carbon film. These pores are formed due to the evolution of gases during heating. ImageJ software analysis of pore size analysis on SEM micrographs has been summarized in figure 33(f) exhibiting wide range of pore size distribution from 10's of nm to a few μm. However, the majority of pores size is less than 100 nm. The pore size and quantity can be controlled by controlling the heating rate. Slow heating rate of 1°/min result in relatively pore free structure [125].

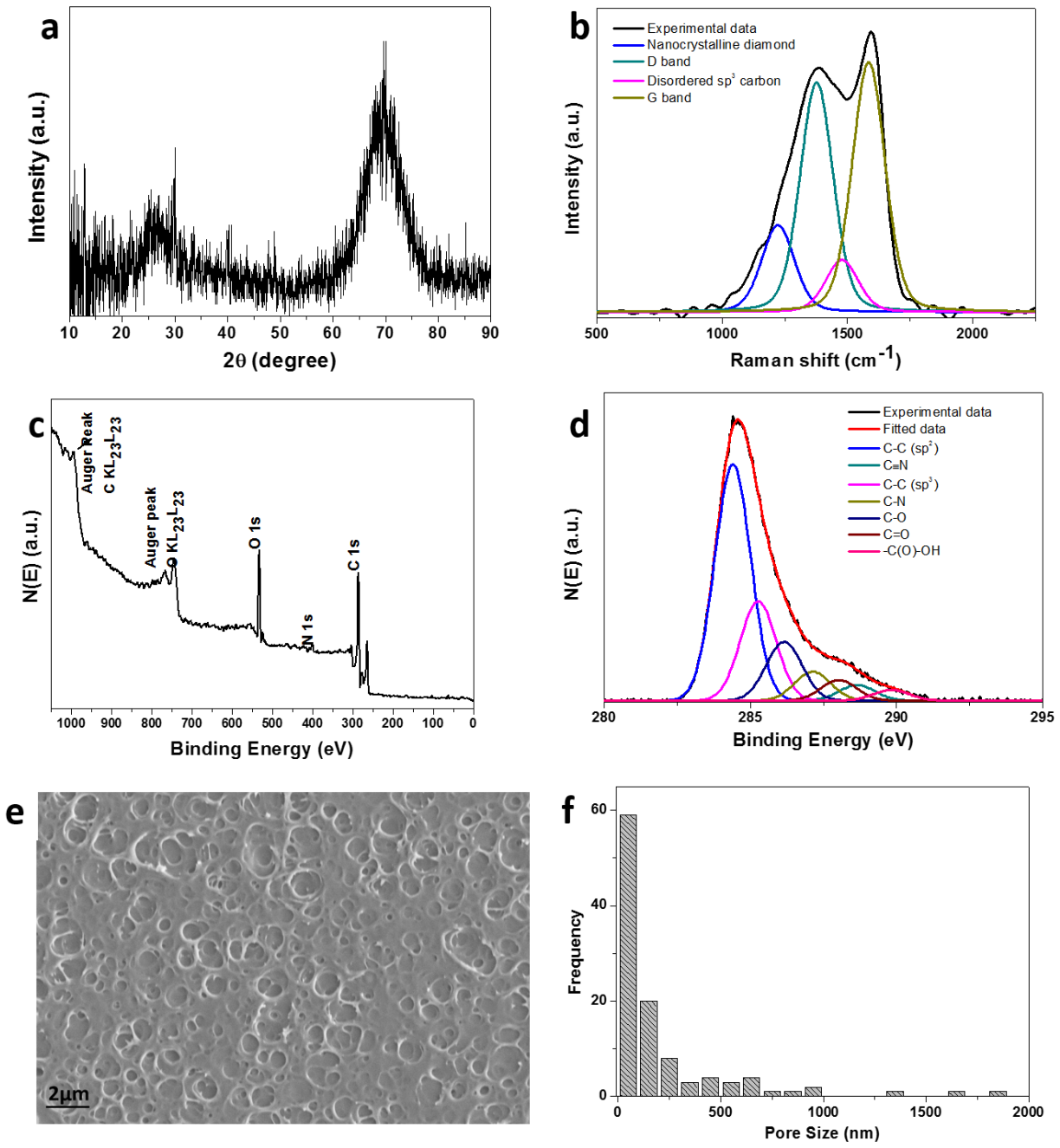

Figure 33: Characterization of in-lab synthesized thin glassy carbon. (a) XRD, (b) deconvoluted Raman, (c) XPS survey, (d) deconvoluted and peak-fitted XPS spectrum of C (1s) peak of synthesized glassy carbon. (e) SEM micrograph and (f) pore size distribution of glassy carbon.

4.3.1.2 Analysis of different size sorted MoS_2

The MoS_2 particles and sheets were prepared in DMF by liquid exfoliation and separated by differential centrifugation. Representative TEM micrographs of MoS_2 collected at different centrifugation speed are presented in figure 34. Typical particle sizes collected at 1000, 3000, 6000 and 12000 rpm centrifugation speeds are 2000±1000 nm, 1000±200 nm, 500±100 nm and 5-7 nm, respectively. Evidence of liquid exfoliation have been found at particles/sheets collected at 3000 and 6000 rpm. Multilayered MoS_2, and small-size nanosheets and nanoparticles are loosely adhered on large sheets [Figure 34(b, c)]. This indicates the intercalation of MoS_2 sheets during liquid exfoliation process by organic solvent (DMF). A high resolution transmission electron micrograph (HRTEM) of sheets at 6000 rpm is shown in figure 35(b). The image shows the crystalline nature of sheets which has been further confirmed by inverse fast Fourier transformation (IFFT) [Figure 35(c)]. Line analysis of lattice spacing from IFFT image [Figure 6(d)] indicates the lattice spacing to be 2.79 nm which corresponds to $< 10\bar{1}0 >$. The selected area diffraction pattern (SAED) [Figure 35(e)] taken from figure 35(a) further confirms the crystalline nature of sheets/particles; with no lattice structural change in MoS_2 during liquid exfoliation.

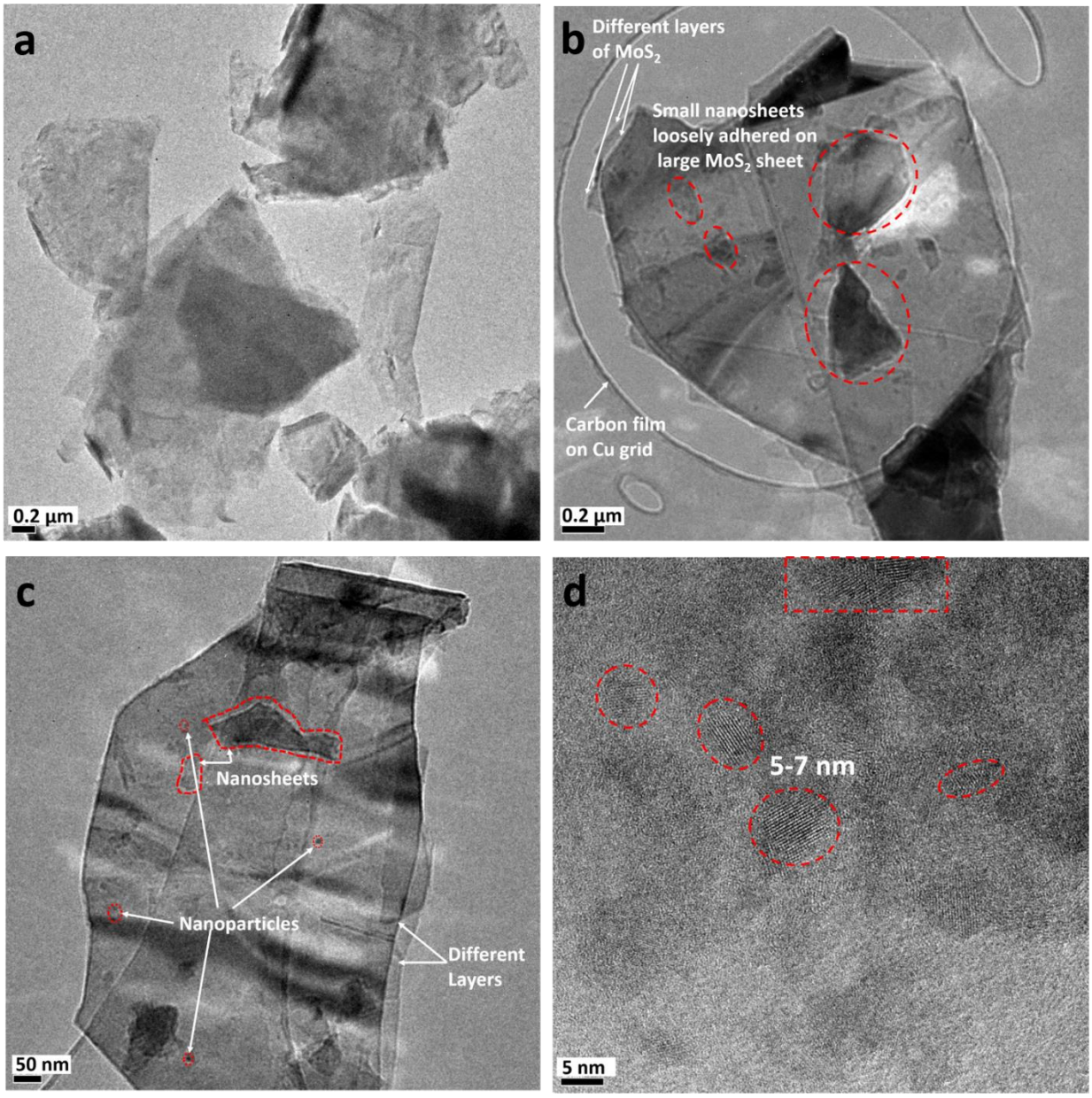

Figure 34: Bright field TEM micrographs of MoS2 particles collected at (a) 1000 rpm, (b) 3000 pm, (c) 6000 rpm and (d) 12000 rpm centrifugation speed showing nanosheets and nanoparticles of different size.

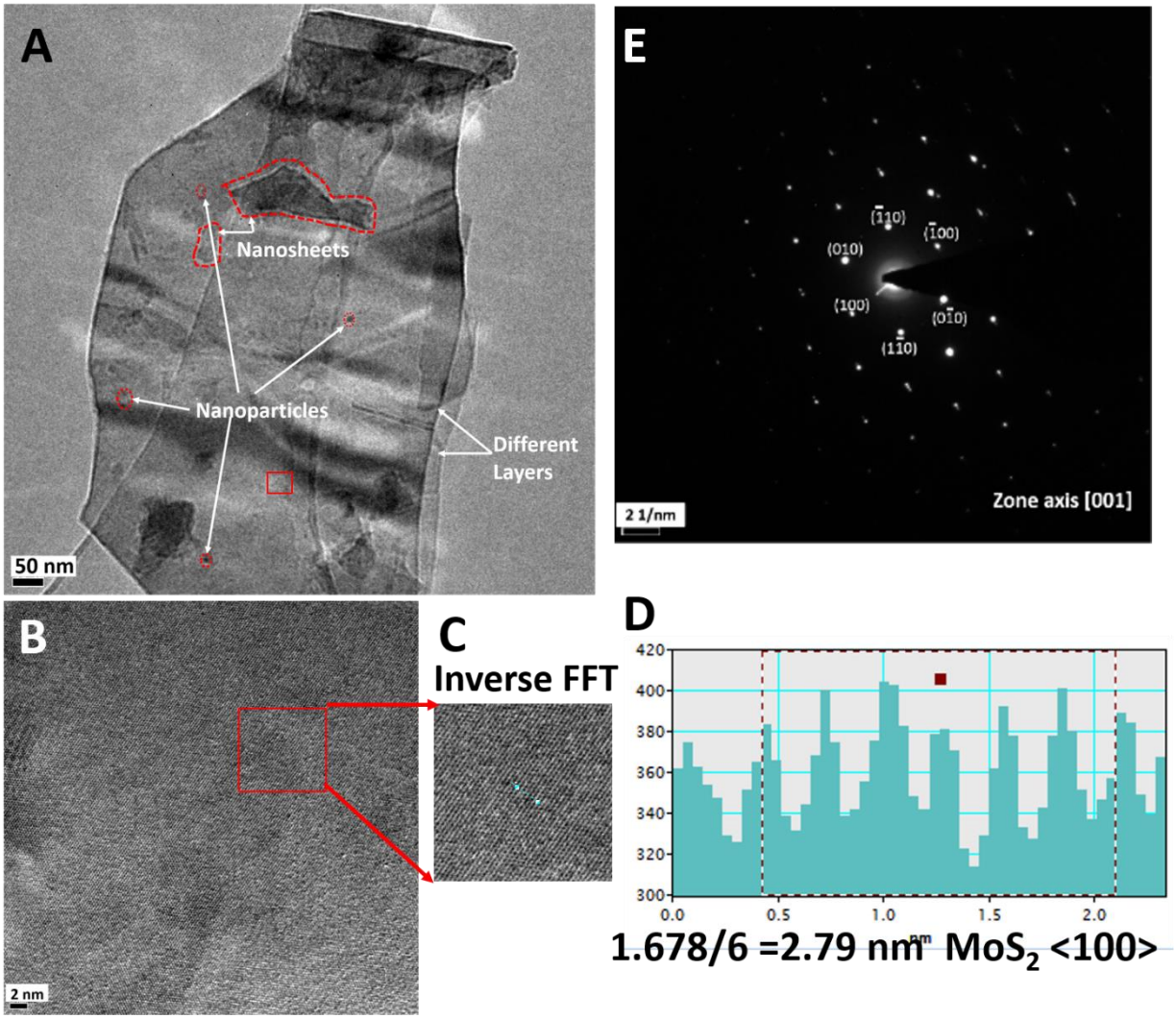

Figure 35: Structure analysis of exfoliated MoS_2. (a) Bright field TEM micrograph of MoS_2 particles collected at 6000 rpm centrifugation speed, (b) magnified view of (a), (c) inverse fast fourier transformation (FFT) obtained from (b), (d) d-spacing analysis. (e) Selected area diffraction pattern (SAED) taken from (a).

MoS_2 particles and sheets were studied by Raman spectroscopy. Raman spectrum of different size-sorted MoS_2 captured using Ar-514nm excitation laser are shown in figure 36(a). Both, E^1_{2g} and A_{1g} Raman modes were observed for 2μm-500nm MoS_2 particles. The E^1_{2g} peak is at 383cm^{-1} for 2±1 μm MoS_2, 383 cm^{-1} for 1±0.2 μm MoS_2,

and 3843 cm^{-1} for 500±100nm MoS_2. The A_{1g} peak is at 408 cm^{-1} for 2±1 μm MoS_2, 408 cm^{-1} for 1±0.2 μm MoS_2, and 409 cm^{-1} for 500±100 nm MoS_2. Therefore, the peak separation is 25, 25 and 24 cm^{-1} for 2±1 μm MoS_2, 1±0.2 μm MoS_2 and 500±100 nm MoS_2, respectively. A blue shift has been observed in UV-Vis spectroscopy for different size particles/nanosheets [Figure 36(b)]. These peak positions and their separations are in good agreement with literature [133, 134] and indicate the gradual decrease in number of MoS_2 layers present in particles and sheets with decreasing size of MoS_2 exfoliated by the liquid exfoliation method. SEM micrographs of different sizes drop-cast MoS_2 on thin glassy carbon are presented in figure 37. It is clearly evident that roughness of drop-cast electrode decreases with reducing particle size. MoS_2 particles collected at 1000 rpm, 3000 rpm and 12000 rpm are 1-2 μm, 0.5-1 μm and 600-400 nm in size. Similar particle sizes have been observed from TEM (Figure 34). Platelet type morphology has been observed from SEM micrographs for particles collected at 1000 rpm and 3000 rpm. 5-7 nm Size MoS_2 particles collected at 12000 rpm are much smaller in size. However, these nano size particles form dense adherent layer with thin glassy carbon upon drying resulting in relatively smooth film.

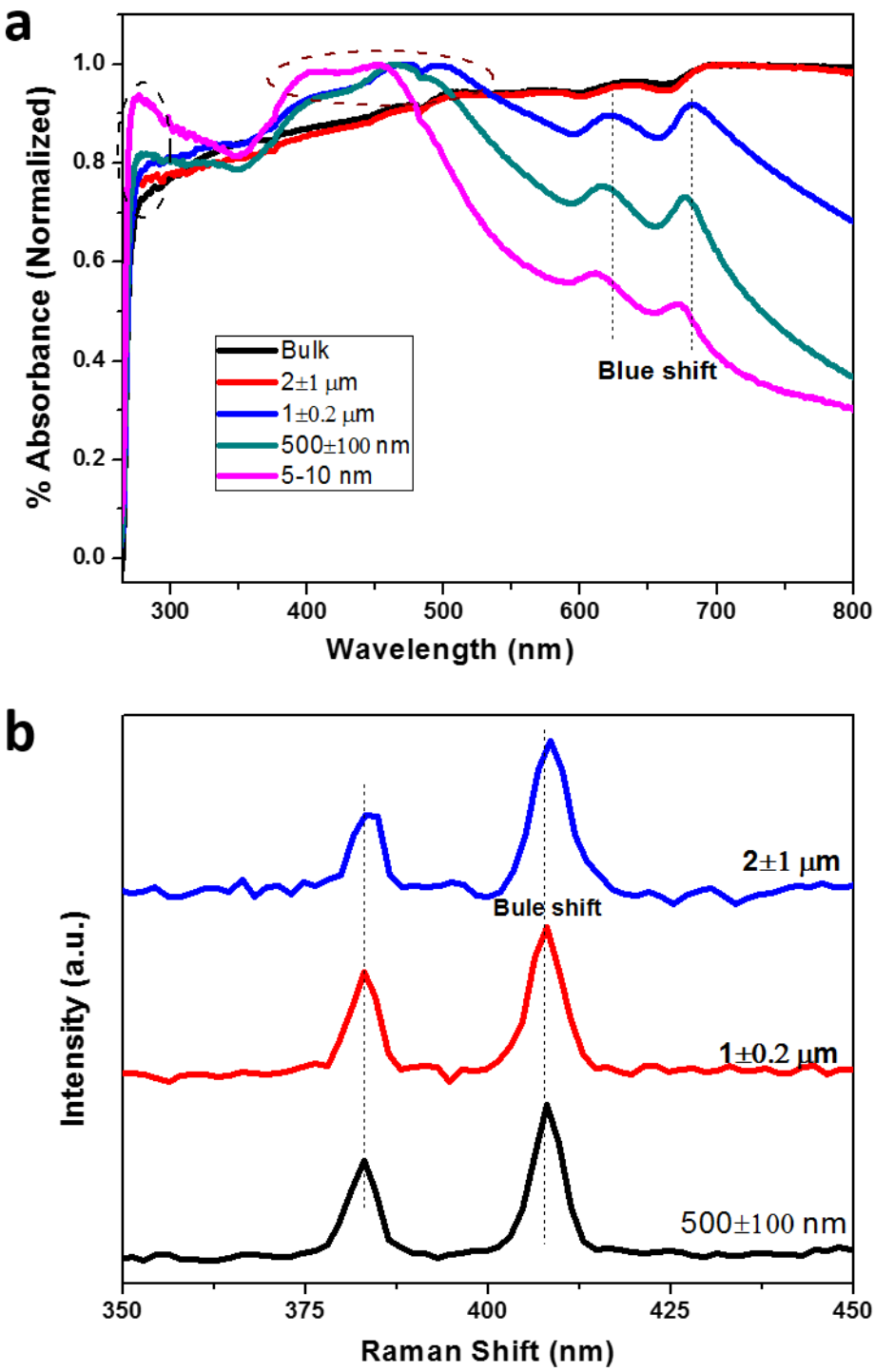

Figure 36: (a) UV-Vis and (b) Raman spectrum of different size MoS_2 particles collected at different centrifugation speed.

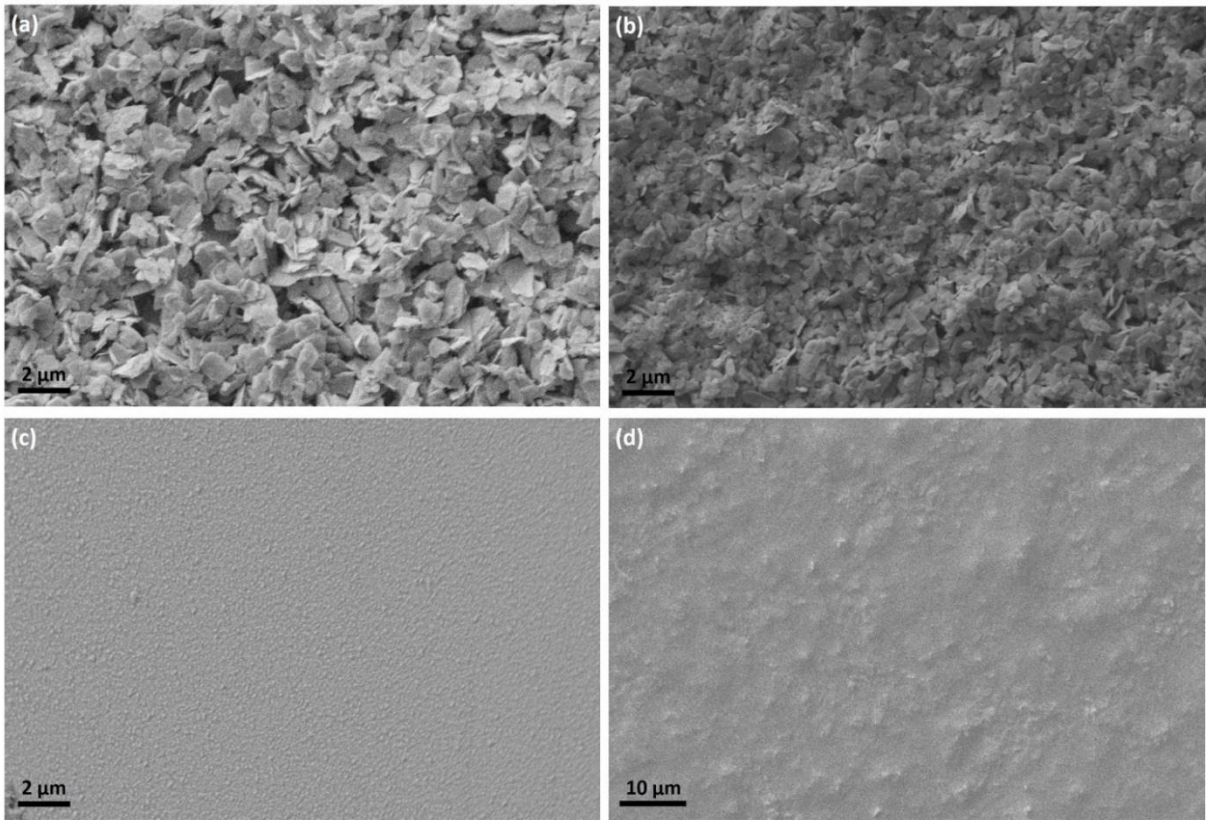

Figure 37: SEM micrographs of drop-cast MoS_2 on thin glassy carbon centrifuged at different speed (a) 1000 rpm, (b) 3000 rpm, (c) 6000 rpm and (d) 12000 rpm.

4.3.1.3 Electrochemical detection of free radicals

Electrocatalytic activity of glassy carbon and MoS_2 modified glassy carbon electrodes were assessed in N_2 saturated 10 mM PBS solution (pH ~7.4; similar to the human body). Cyclic voltammetry response of glassy carbon and MoS_2 modified glassy carbon electrodes are presented in figure 38A. Cyclic voltammetry measurements for H_2O_2 were conducted in the potential range between -0.2 to -0.8 V. It is clearly visible that reduction current increased in the case of MoS_2-modified electrode. The negligible reduction current response of glassy carbon (without MoS_2) in the presence of 5 mM H_2O_2 is attributed to the highly inert nature of glassy carbon toward H_2O_2. Porous glassy carbon was used to capture small variations in reduction current due to its low internal resistance

as compared to gold electrodes [135]. On the other hand, MoS_2 reacts with H_2O_2, and generates ~9 times more current than unmodified glassy carbon. The systematic increase in the reduction current during cyclic voltammetry suggests that the effective surface area and active edge sites play a crucial role in the electrocatalytic activity of H_2O_2 reduction similar to the hydrogen evolution reaction [136, 137]. Based on the cyclic voltammetry, only 5-7 nm size MoS_2 nanoparticles were selected for chronoamperometry study.

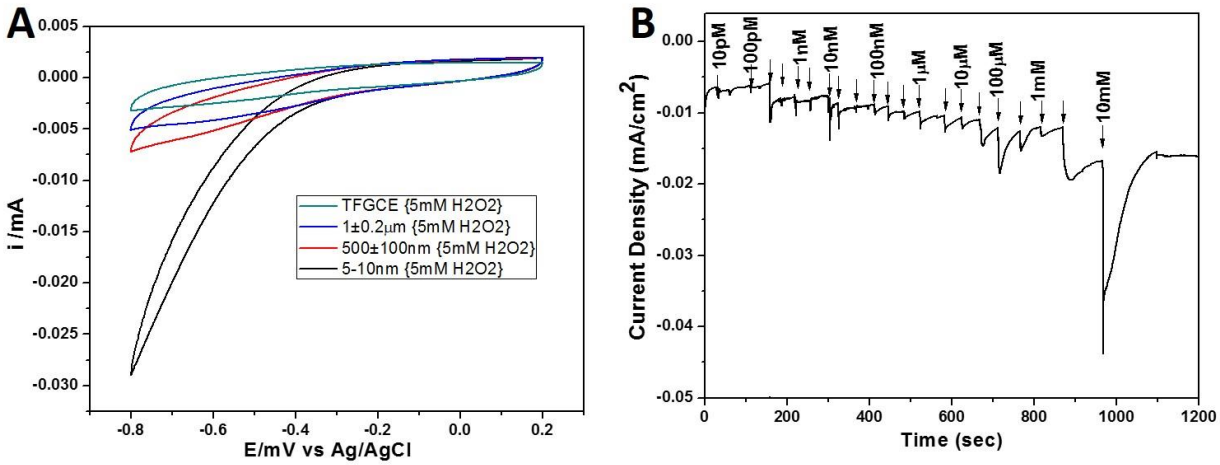

Figure 38: Electrochemical performance evaluation of MoS_2 modified electrode. (A) Cyclic voltammograms for bare glassy carbon and different size sorted MoS_2 modified electrode in 5mM H_2O_2 in 10 mM PBS electrolyte at 25mV/sec scan rate. (B) Chronoamperometric response of 5-7 nm size MoS_2 modified electrode towards H_2O_2 in 10 mM PBS electrolyte.

The chronoamperometry experiment was conducted at -0.25 V to evaluate the detection limit of the constructed biosensor. Our results show that water does not dissociate at potential >-0.3V; therefore the measured reduction current is only from the dissociation of H_2O_2 (O_2 redox produces minimal response due to N_2 purging treatment). Current (i) vs time (t) graph of nanoparticle-modified glassy carbon electrode is shown in

figure 38B. Different concentrations of H_2O_2 were added in the N_2 saturated 10 mM PBS solution at an interval of 30 sec or after current saturation. A reduction in current change at -0.25 V was observed when 10 pM H_2O_2 was added in the 10 mM PBS electrolyte. A similar amount of reduction current increase is also visible from figure 38B for the further addition of 10 pM H_2O_2. The amount of current increase is constant with H_2O_2 addition up to micro-molar concentration. However, we observe significant enhancement of current when H_2O_2 concentration increases to milli-molar. Comparison of current work with the literature (Table 4) demonstrates that the biosensor, which is fabricated with MoS_2 nanoparticles, is extremely sensitive towards H_2O_2 and therefore can detect H_2O_2 of 2 order lower concentration when compared to existing literature (Table 4). Wang et al. [26] have analyzed the effect of interfering species (ascorbic acid and uric acid) on H_2O_2 detection in PBS electrolyte during chronoamperometry experiment using MoS_2 as working electrode. The chronoamperometry test did not show any change in the reduction current with 500 μM uric acid and 100 μM ascorbic acid addition which indicate excellent selectivity of MoS_2 sensor. The response time of MoS_2 sensor for H_2O_2 detection is 2-3 seconds.

Table 4: Summary of performance of H_2O_2 sensors/assays.

Detection Element; electrode	**Detection Type**	**Sensitivity**	**LOD**	**Ref.**
MoS_2 nanoparticles on porous glassy carbon	Sensor	NR	1 pM	This work
Ag NPs decorated carbon nanotubes	Sensor	NR	1.6 µM	[24]
$CoFe_2O_4$ magnetic NPs in *β*-cyclodextrin	Assay	NR	20 nM	[8]
Carbon-coated SnO_2 supported Pt NPs	Sensor	241.1 $A.mM^{-1}.cm^{-2}$	0.1 µM	[13]
Prussian blue deposited on glassy carbon	Sensor	0.6 $A.M^{-1}.cm^{-2}$	80 nM	[138]
Mesoporous Pt microelectrode from liquid crystals	Sensor	2.8 $A.M^{-1}.cm^{-2}$	4.5 µM	[139]
Mg-modified silicon nanowire thin film	Sensor	78.9 ± 2.9 nA. $mmol^{-1}$	NR	[140]

NR: Not reported

Similarly, the prospect of HOCl detection using MoS_2-modified electrode was also investigated via electrochemical methods. The potential range of -0.2 to 1.0 V was selected for cyclic voltammetry experiments. As a surrogate for HOCl, NaOCl was utilized for experiments; which is permissible since measurements were performed in a neutral pH

PBS buffer. PBS buffer solution contains sodium phosphate, potassium chloride and sodium chloride, NaOCl can be used as a substitute of HOCl. Figure 39A shows the cyclic voltammetry response in 10mM PBS solution while 5mM NaOCl was added in the PBS electrolyte. It is important to note that the current response of glassy carbon is similar to bulk MoS_2. However, current response increases with decrease in MoS_2 particle size from bulk to nanoparticles, evidently signifying the importance of MoS_2 edge to volume ratio. Chronoamperometry experiment was conducted at 1.1 V to avoid interference from water reaction with MoS_2. Therefore, current increase will be purely due to the dissociation of NaOCl only.

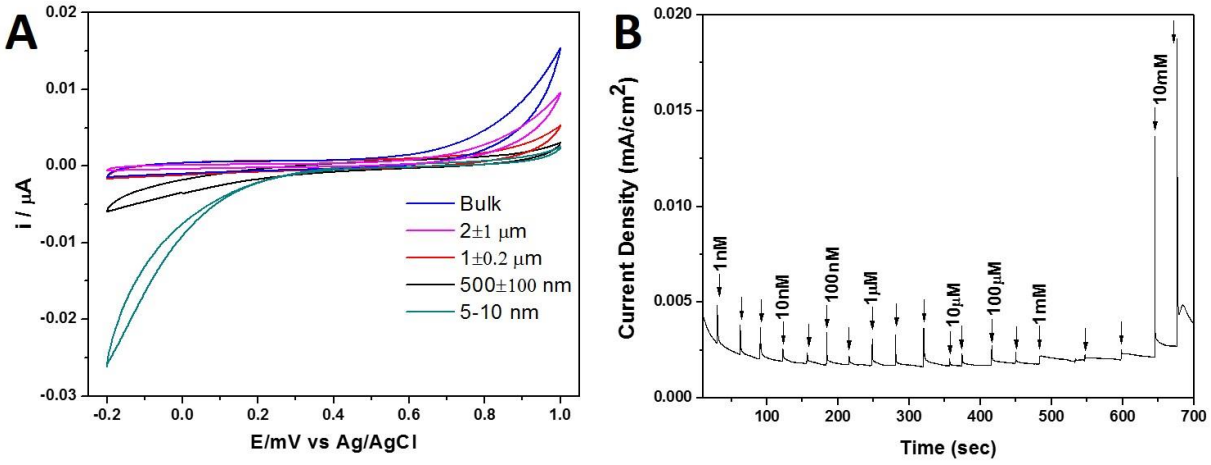

Figure 39: Electrochemical performance evaluation of MoS_2 modified electrode. (A) Cyclic voltammograms for bare glassy carbon and different size sorted MoS_2 modified electrode in 5mM NaOCl in 10mM PBS electrolyte at 25mV/sec scan rate. (B) Chronoamperometric response of 5-7 nm size MoS_2 modified electrode towards NaOCl.

Different concentrations of NaOCl were added in the solution at an interval of 40-45 sec. Current increase was clearly evident from figure 39B when 1 nM NaOCl was added in the 10 mM PBS electrolyte. A sudden increase in current, observed at the addition of 1 mM NaOCl, is attributed to the higher catalytic reactivity at MoS_2 edges because of the moderate bonding energy of ligands on edge sites (discussed in section 4.3.2.2). Chronoamperometry response also indicates two different linear detection ranges from 1 nM to 1 µM, and from 10 µM to 3mM as reported in table 5. The lower detection limit of this work is three orders lower than the published literature (Table 5); demonstrating the ultra-low concentration detection ability of MoS_2 nanoparticle-modified electrode. This electrochemistry based sensor also exhibited a fast response time of 2-3 seconds which is significantly faster in comparison to the organic molecule based fluorescence assays commonly used to detect HOCl [9, 10].

Another important radical of interest to the biomedical research community is the nitric oxide radical (NO^*). The NO^* acts as a neurotransmitter and regulates cardiovascular physiology indicating the bright side of gaseous radical [60, 141, 142]. On the other hand, NO^* interacts with superoxide radical ($O_2^{\bullet-}$), and forms peroxynitrite ($ONOO^-$) which is a strong oxidizer for DNA, proteins and lipids [60, 141]. In the present study, NO radicals have been produced by the decomposition of *S*-Nitroso-*N*-acetyl-D,L-penicillamine (SNAP). The decomposition of SNAP is very slow, therefore various metal ions catalysts (Cu^{2+}, Cu^{+}, Fe^{2+}) have been used to accelerate the decomposition of SNAP [60, 142]. CuCl is used as a catalyst for the decomposition of SNAP in the present study based on its performance over a large range of SNAP concentrations. For the electrochemical detection of the NO^*, measurements were carried out at room

temperature at pH 5.5. At pH <4 or pH >7, the conversion rate of SNAP into NO^* reduces to ~80% [142]. It is important to note that the pH of cancerous tumors is also acidic and is in the pH range of 4-6. For measurements, CuCl solution was used as an electrolyte and desired amount of SNAP solution was added during electrochemical measurements.

$$2SNAP\ (RSNO) \xrightarrow{CuCl\ [3mM]\ pH\ 5.5} RSSR + 2NO^* \quad (23)$$

Table 5: Summary of performance of recent HOCl sensors/assays.

Detection Element; electrode	**Detection Type**	**Sensitivity**	**LOD**	**Ref.**
MoS_2 nanoparticles on porous glassy carbon	Sensor	NR	1 pM	This work
SC pi-conjugated fluorescent polymers; oxidation of aniline units produces fluoro quenching	Sensor	NR	0.5 μM	[143]
Boron-containing fluoro compound	Assay	NR	0.2 μM	[9]
Rhodamide + hydrazide fluorescent compounds	Sensor	NR	0.06 μM	[144]
Acenaphthenequinone fluoro molecule	Sensor	NR	0.34 μM	[31]
Fluorescent, organic molecule emitting in NIR	Assay	NR	0.7 μM	[10]

NR=Not reported

For NO^* detection, cyclic voltammetry experiment was carried out in the potential range of 0.2 to 1.0 V. These findings are similar to the H_2O_2 and HOCl (Figure 40A). It is clearly evident from CV results that MoS_2 nanoparticle-modified electrode showed an increase in current when 50nM SNAP solution was added in the 3mM CuCl solution. On the other hand, glassy carbon electrode and the electrode modified with larger size particle of MoS_2 did not show any significant increase in current in presence of CuCl and upon addition of SNAP solution. For sensitivity measurement, chronoamperometry experiment was conducted at 867mV, again above -0.25V. Therefore, current density increase is purely due to the dissociation of SNAP only. Different concentrations of SNAP were added in the solution at an interval of 40-45 sec. Current density increase was clearly evident from figure 40B when 10nM SNAP was added in the electrolyte. The behaviour of NO^* is similar to H_2O_2 and HOCl. The sensitivity of MoS_2 nanoparticle-modified electrode is 4.56×10^{-6} A/nM.cm^2 and the linear range of detection is 10-110 nM. These values are comparable to literature and summarized in table 6. Additionally, time of detection for MoS_2 based electrochemical method is 4-5 seconds.

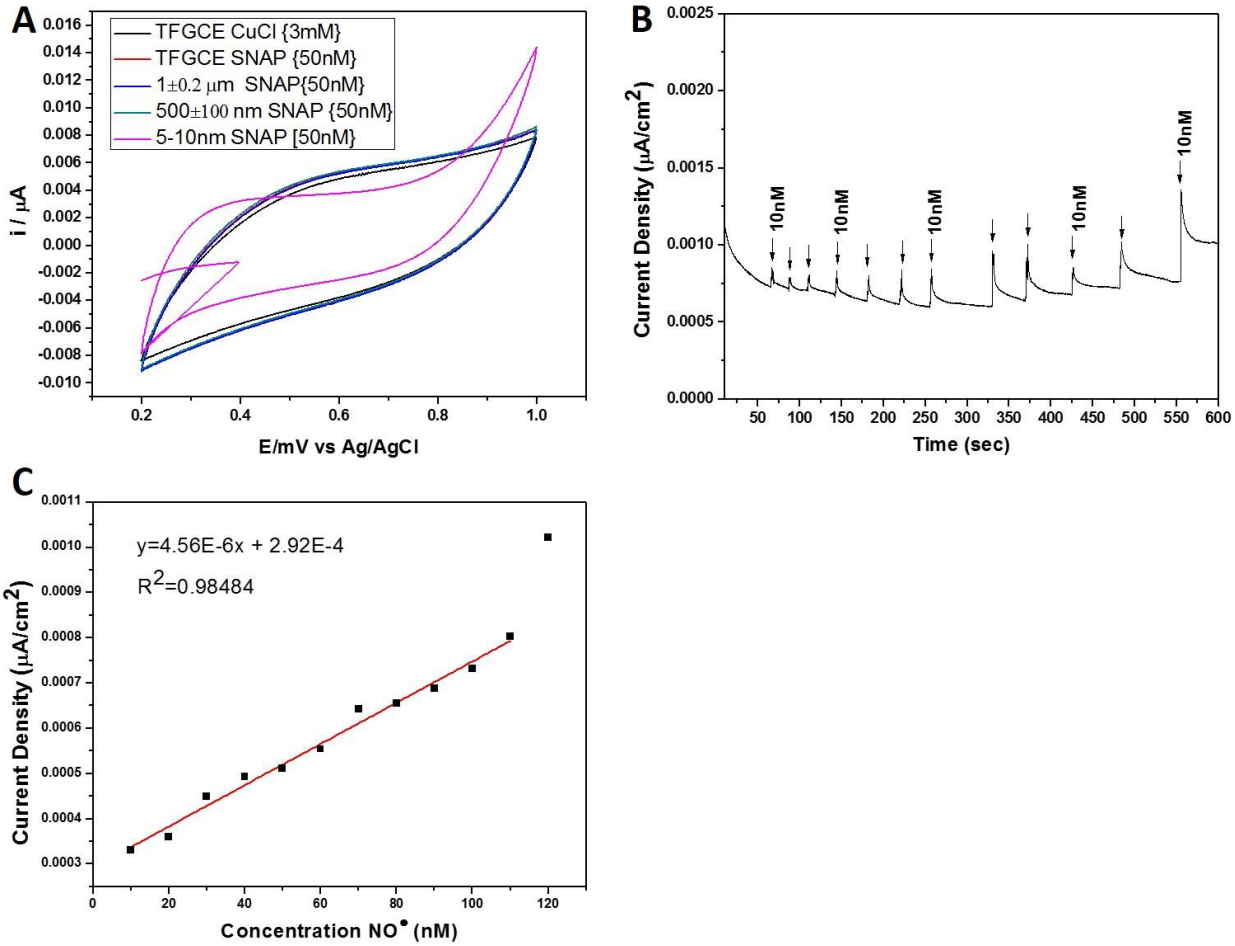

Figure 40: Electrochemical performance evaluation of MoS_2 modified electrode. (A) Cyclic voltammograms for bare glassy carbon and different size sorted MoS_2 modified electrode in 50nM SNAP in 3mM CuCl electrolyte at 25mV/sec scan rate. (B) Chronoamperometric response of 5-7 nm size MoS_2 modified electrode towards NO^*. (C) Calibration curve of the amperometric response to the concentration of NO^* from 10 nM to 110 nM.

Table 6: Summary of performance of recent NO sensors.*

Detection Element; electrode	**Detection Type**	**Sensitivity**	**LOD**	**Ref.**
MoS_2 nanoparticles on porous glassy carbon	Sensor	$4.56x10^{-6}$ A/nM.cm^2	--	This work
Au NPs on nanostructured ITO	Basic research	NR	0.65 μM	[36]
Catalase/SOD/Microperoxidase/MWCNT-poly-5,2 :5 ,2 -terthiophene-3 -carboxylic acid/AuNPs	Sensor	1.10±0.01 AM^{-1}	4.3±0.2 nM	[145]
Nafion/MWNTs-CS-Au NPs	Sensor	$1.73AM^{-1}$	7.60 nM	[25]
QCL	Sensor		0.7 ppbv	[146]
Nano-alumina glassy carbon	Sensor	0.037 μA $μM^{-1}$	7.2 nM	[14]
4,5-diaminofluoroscein formed on electrode substrate via layer-by-layer assembly	Sensor	NR	5 nm	[147]
Electrodeposited poly(p-phenylenevinylene) on GC	Sensor	42.68 nA/μmolL^{-1}	0.23 nmolL^{-1}	[148]
Fluorinated xerogel on microelectrodes	Sensor	7.91 pA·nM^{-1} 7.60 nA· $μM^{-1}$	83 pM	[149]
QCL	Sensor		4.9 ppbv	[15]

Detection Element; electrode	Detection Type	Sensitivity	LOD	Ref.
Single-walled carbon nanotubes/Room temperature ionic liquid gel on a micro-electrode	Sensor	43.6 $mA.mM^{-1}$	NR	[150]
Hemoglobin protein immobilized in sodium montmorillonite on pyrolized graphite electrode	Sensor	NR	20 pM	[151]
Hemoglobin/montmorillonite/ PVA on pyrolized graphite electrode	Sensor	NR	0.5 μM	[16]
Hemoglobin on nanoporous tin oxide	Sensor	NR	1 μM	[17]
RGD peptide functionalized Graphene	Sensor	NR	25 nM	[152]
MWCNT	Sensor	NR	0.8 nM	[153]

NR=Not reported

4.3.1.4 Surface chemistry of size-sorted MoS_2

To understand the size-dependent electrocatalytic behavior of MoS_2, XPS studies were carried out on different size-sorted MoS_2. Deconvoluted XPS spectra of Mo (3d) and S (2p) are shown in figure 41. Peaks were fitted with PeakFit® software using Gaussian distribution. Four prominent peaks are visible for bulk MoS_2 at binding energies of 232.0 eV, 228.8 eV, 163.9 eV and 161.7 eV corresponding to Mo($3d_{3/2}$) Mo($3d_{5/2}$), S($2p_{1/2}$) and S($2p_{3/2}$) in the Mo-S bond, respectively. However, peak shift for both Mo (3d) and S (2p) towards higher binding energy is clearly evident with decreasing MoS_2 size. This behavior of MoS_2 is in good agreement with our UV-Vis and Raman spectroscopy results presented in figure 36. To quantify the stoichiometric chemistry of different size-sorted MoS_2, the S to Mo ratio were calculated from XPS spectrum. The S to Mo ratios are 1.99, 1.99, 1.98, 1.92 and 1.83 for bulk MoS_2 (raw material), sizes 2±1 μm MoS_2, 1±0.2 μm MoS_2, 500±100 nm MoS_2 and 5-7 nm MoS_2, respectively. Therefore, 5-7 nm MoS_2 is sulfur-deficient in nature and deficiency increases as the MoS_2 size decreases from μm to nm. The crystalline nature of MoS_2 from HRTEM images (Figure 34 and 35) indicates the presence of sulfur deficiency at the edges of layered MoS_2 structure. These defects alter the band gap and binding energy of MoS_2 [154-156] as observed from UV-Vis and XPS spectra which could be responsible for the detection of different free radicals.

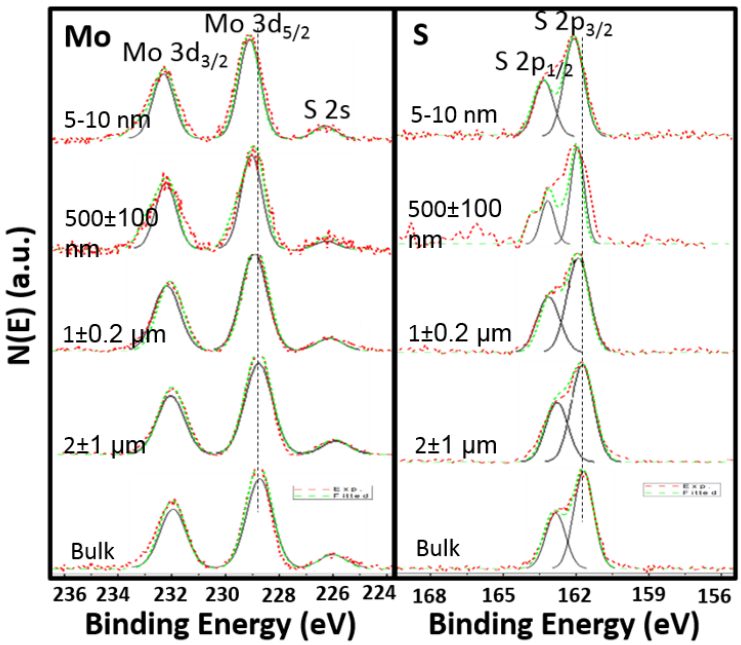

Figure 41: Deconvoluted and peak-fitted XPS spectrum of Mo (3d) and S (2p) taken from different size sorted MoS_2 particles/nanosheets. Reduction in size leads results in sulfur deficiency. Surface S to Mo ratio for different MoS_2 was measured from the integrated area under peaks corresponding to Mo ($3d_{5/2}$) and S ($2p_{3/2}$).

The CV results of different size-sorted MoS_2 have shown an increase in reduction current density with 5 mM H_2O_2 addition in 10 mM PBS solution. Several recent studies have demonstrated various physical property changes with increase in defect density in MoS_2 monolayers processed via defect engineering [157-162]. Islam et al. [157] has demonstrated up to four order of magnitude change in mobility, on-current and resistance of single layer MoS_2. This was accomplished by developing insulating MoO_3-rich disordered domains in single layer MoS_2 by varying oxygen plasma exposure time. Therefore, single layer MoS_2 deviate from semiconductor to insulator type behavior. Parkin et al. [158] report a shift in Raman peak for electron-irradiated single layer MoS_2.

The peak shift has been attributed to the generation of sulfur vacancies upon electron beam irradiation in TEM and correlated with 2D conductivity of MoS_2 single layer. Current decreases with increasing the electron-irradiation dose. On the other hand, Yu et al. [161] have developed a thiol-based chemistry route to repair the sulfur vacancy defects. Mobility of MoS_2 monolayer improved due to the reduction in charged impurities, short-range defects and traps leading to higher intrinsic charge transport. This study supports the finding of Parkin et al. [158] validating the role of sulfur vacancies on conductivity. A strong photoluminescence and electrocatalytic activity towards the hydrogen evolution reaction has also been observed for electrochemically exfoliated 2.5-6 nm MoS_2 particles [162]. Interestingly, a blue shift has been observed for 2.5 nm and 4.6 nm particles exfoliated with 0.1% and 1.0% aqueous LiTFSI electrolyte [162]. It is clearly evident from these examples that improvements in various physical and chemical properties of MoS_2 is highly dependent on defect density and charge impurities. In the present case, the intrinsic defect density of sulfur vacancies increases with decreasing size of MoS_2. It is well known that basal planes of MoS_2 are inactive, and active edge sites were proposed to be mainly responsible for the electrocatalytic activity of MoS_2 nanosheets [163-166]. Recent studies [167] point to the important role of vacancies in enabling chemical reactivity of the MoS_2. MoS_2 has two edges: $(\bar{1}010)$ and $(10\bar{1}0)$ edges, which correspond to S- and Mo edges, respectively. Our experimental studies summarized above, however, do not shed light on which edge site (either Mo or S) is more active for the catalytic activity. To obtain atomistic insights into the relative importance of the two types of edges and possible role of S vacancies, we present below results of our modeling of a set MoS_2 nanoparticles (NPs) using DFT.

4.3.2 Computational modelling results

4.3.2.1 Geometry and electronic structure of Mo_xS_y nanoparticles

For our DFT calculations four different sizes of NPs were constructed, consisting of 36, 81, 144, 225 atoms, i.e. $Mo_{12}S_{24}$, $Mo_{27}S_{54}$, $Mo_{48}S_{96}$ and $Mo_{75}S_{150}$. All NPs considered in our calculations have hexagonal shape following their Wulff construction (Figure 42), according to which the equilibrium shape minimizes the total free energy of the cluster, i.e. the sum over all edge free energies times the corresponding edge length [168]. Thus, if the ratio of edge free energies is equal to unity the shape will be perfectly hexagonal. The equilibrium shape of an MoS_2 NP is governed by the relative free energies of edges with two low-index edge terminations of the (0001) basal plane, i.e., the $(10\bar{1}0)$ Mo edge and $(\bar{1}010)$ S edge. Since the free energies of these two edges are identical, the MoS_2 NPs considered here form perfectly hexagonal shape, as shown in the inset of figure 43. Such truncated hexagonal shapes were observed in the STM images of single-layer MoS_2 on Au(111) under the sulfo-reductive conditions [169].

Our calculated electron density of states (DOS), from -2.5 to 2.5 eV, projected onto the d-orbitals of Mo atoms at both the $(10\bar{1}0)$ and $(\bar{1}010)$ edges of the NPs of four sizes are shown in figure 43(a-b), respectively. Clearly, the electronic structure at the Fermi level depends on the size of the NPs. Of most interest to us is the frontier occupied state, which is most well-defined for the smallest of the NPs, as seen in figure 43a. As the NP size increases, it breaks the degeneracy of orbitals. The peak just below the Fermi level for $Mo_{27}S_{54}$ is thus split into two and the splitting arises mainly from the non-degeneracy of the d_{xy} and d_{x2-y2} orbitals.

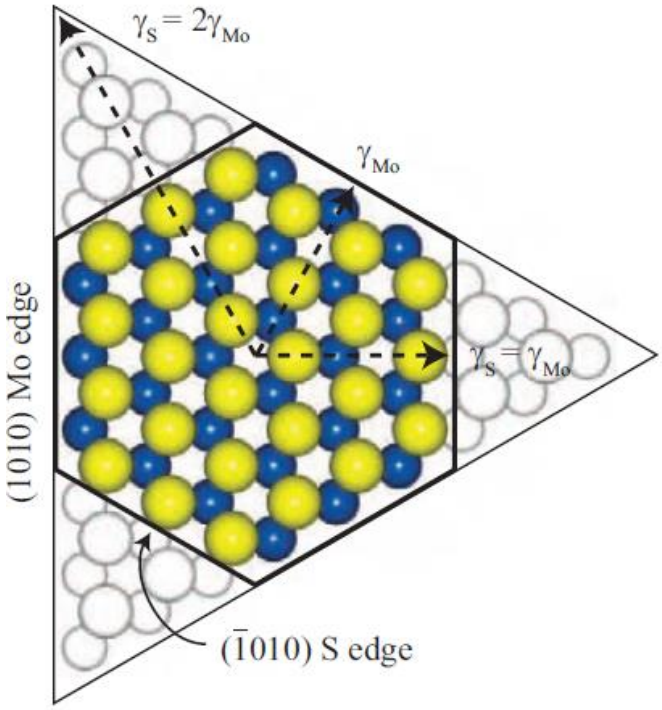

Figure 42: Wulff construction of MoS_2 NPs considered in DFT calculations showing stable hexagonal shape, and Mo and S rich edges.

Note that the $(10\bar{1}0)$ and $(\bar{1}010)$ edges of the NPs are distinctly different as they contain 0% and 100% S, respectively (see Figure 44). Termination of the single-layer MoS_2 with either edge breaks its point symmetry group (D_{3h}) and edge states of the NPs appear inside the single-layer band gap [163, 164]. These edge steps have been proposed as sites for adsorption of molecules and ligands [170, 171], and regions of enhanced catalytic activity [172]. For insights into the differences in the electronic structure of Mo atoms (dark blue and purple balls) on the $(10\bar{1}0)$ and $(\bar{1}010)$ edges we compare their electronic density of states (DOS) in figure 45. Most prominently, as seen in the lower two panels of figure 43b, Mo atoms in the $(\bar{1}010)$ edge, for both $Mo_{48}S_{96}$ and $Mo_{75}S_{150}$, do not contribute to d states in the energy range -0.5 eV to the Fermi level (E_F), but Mo at $(10\bar{1}0)$ offer d states (figure 43a, lower panels) in the same energy range. This

difference originates from the local coordination: Mo atom at $(10\bar{1}0)$ edge consists of more dangling bonds than that at $(\bar{1}010)$, because of the absence of S atoms (0% S) at the former edge and the presence of 100% S at the latter. These results suggest that the $(10\bar{1}0)$ edge may be more chemically active than $(\bar{1}010)$.

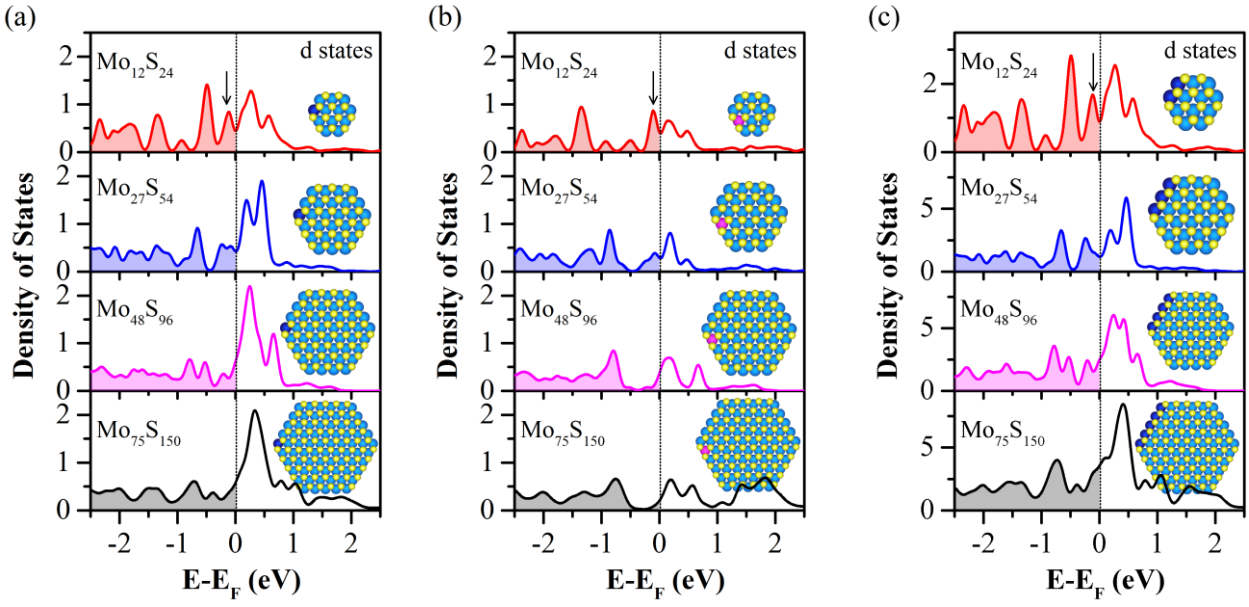

Figure 43: (a) Electronic density of states of a) a Mo atom (dark blue) at $(10\bar{1}0)$ edge, and (b) a Mo atom (pink) at $(\bar{1}010)$ edge, and (c) all Mo atoms (dark blue) at $(10\bar{1}0)$ edge.

In order to understand the combined effect of all edge atoms on the electronic structure, we present in figure 43c the d-states of all Mo atoms (dark blue balls) at the $(10\bar{1}0)$ edge. The sharp peak just below E_F observed for the smallest NP, $Mo_{12}S_{24}$, in the top panels of figure 43a and 43b, is even more prominent in figure 43c, but for the larger NPs (lower panels), this peak smoothens and shifts away from E_F (bottom panel). In fact, the features in figure 43c are essentially similar to those in figure 43a, with enhancements as a result of inclusion of multiple atoms. As the d-states near the Fermi level are

expected to play a dominant role in chemical activity, these results suggest, in agreement with the experimental observations presented above, that NPs of larger size are less catalytically active than the smaller ones. These comparisons are, of course, only qualitative, given the large difference in the size of the nanoparticles in the experiments as compared to those considered in our calculations.

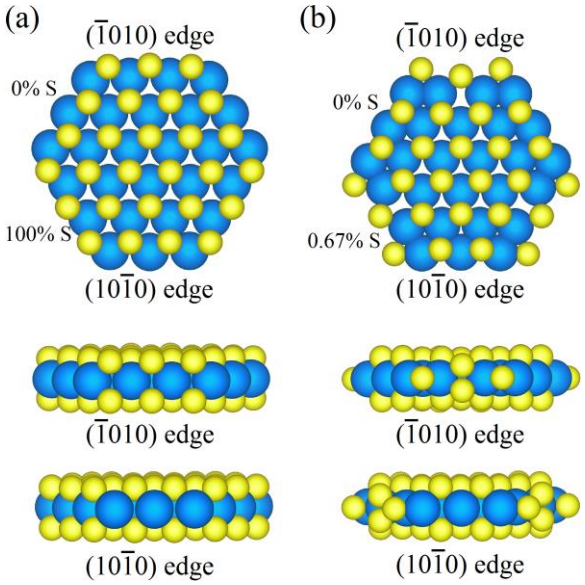

Figure 44: Schematic representation of atomic structures of (a) $Mo_{27}S_{54}$, and (b) $Mo_{27}S_{48}$ nanoparticles. The blue and yellow balls represent the Mo and S atoms, respectively.

Since our experiments, summarized above, and in particular the XPS findings, indicate a strong role for S-vacancies in facilitating the reactions, and since such role of vacancies have also been proposed [167], we present below a comparative examination of the initial steps of reactions of interest here for two small NPs, one of which contains S vacancies, i.e. $Mo_{27}S_{54}$ (Mo:S=1:2) and $Mo_{27}S_{48}$ (Mo:S=1:1.8). The schematic representation of atomic structures of $Mo_{27}S_{54}$ and $Mo_{27}S_{48}$, in figure 44, shows their $(\bar{1}010)$ and $(10\bar{1}0)$ edges, which for the former contain, respectively, 100% S and 0% S

atoms, whereas in the case of the latter have 67% S and 0% S atoms, respectively. Similar truncated hexagonal MoS_2 nanostructures have been predicted for catalytic application by previous studies [173, 174].

4.3.2.2 Adsorption of H_2O_2, OH and H_2O on Mo_xS_y nanoparticles

In this section, we summarize our calculated results for the adsorption energy (E_{ad}) of H_2O_2 and H_2O at both $(10\bar{1}0)$ and $(\bar{1}010)$ edges of Mo_xS_y (where x=27 and y=54 and 48). The E_{ad} was calculated using $E_{ad} = E_{(Adsorbate/MoxSy)} - [E_{(Adsorbate)} + E_{(MoxSy)}]$, where $E_{(Adsorbate/NP)}$, $E_{(Adsorbate)}$ and $E_{(NP)}$ represent the total energies of adsorbate/NP, adsorbate and Mo_xS_y, respectively. Our DFT calculations showed that on both $Mo_{27}S_{54}$ and $Mo_{27}S_{48}$, H_2O_2 adsorbs dissociatively at the $(10\bar{1}0)$ edge, with no activation energy barrier. This spontaneous process yields two hydroxyl (OH) groups at the $(10\bar{1}0)$ edge (Figure 45) of both NPs via the reaction H_2O_2 (g) → OH^*+OH^* (* denotes the adsorbed entity). Their structural parameters are provided in table 7. The calculated adsorption energy of dissociated H_2O_2 on $Mo_{27}S_{54}$ with respect to its gas phase is -6.77 eV, whereas that on $Mo_{27}S_{48}$ it is -6.54 eV. In contrast, H_2O_2 binds weakly at the $(\bar{1}010)$ edge of both $Mo_{27}S_{54}$ and $Mo_{27}S_{48}$ with adsorption energy of -0.19 eV and -0.35 eV, respectively. The Mo-O distance for H_2O_2 at the $(\bar{1}010)$ edge of $Mo_{27}S_{54}$ is 3.702 Å, and that at the same edge of $Mo_{27}S_{48}$ it is 3.689 Å, allowing us to conclude that H_2O_2 does not chemisorb at the $(\bar{1}010)$ edge. These results indicate that H_2O_2 adsorbs dissociatively only at the $(10\bar{1}0)$ edge of both NPs.

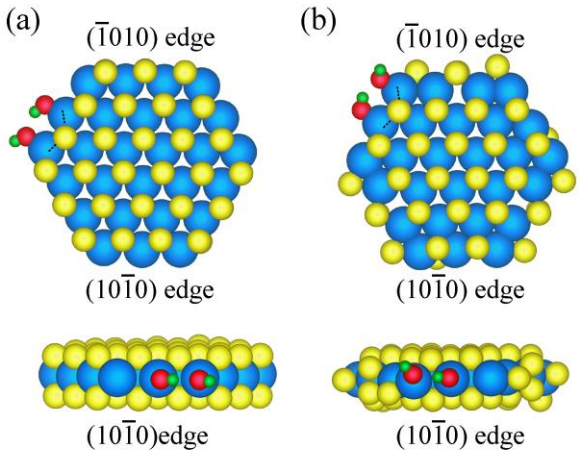

Figure 45: Schematic representation of adsorbed structures of two hydroxyl radicals (OH^*) formed from dissociative adsorption of H_2O_2 on (a) $Mo_{27}S_{54}$, and (b) $Mo_{27}S_{48}$. The blue, yellow, red, and green balls represent the Mo, S, O, and H atoms, respectively.

Next, we compare the adsorption characteristics of OH on both $Mo_{27}S_{54}$ and $Mo_{27}S_{48}$. On $Mo_{27}S_{54}$, OH prefers to adsorb at the bridge site of Mo atoms at the $(10\bar{1}0)$ edge, whereas two OH prefer the top of the Mo atoms (figure 45) of the same edge. The preference of aligning by two OH^*, in which the hydrogen atom of one OH^* points towards the oxygen atom on the other OH^*, is associated with an attractive interaction between them. The adsorption energy of single OH^* is -5.49 eV at the $(10\bar{1}0)$ edge and -2.68 eV at the $(\bar{1}010)$ edge. On $Mo_{27}S_{48}$, however, single OH prefers to adsorb at the Mo atom of the $(10\bar{1}0)$ edge as do two OH^*. The adsorption energy of single OH^* at the $(10\bar{1}0)$ edge is -5.99 eV and -3.77 eV at the $(\bar{1}010)$ edge. Interestingly, in the adsorption of $2OH^*$ on $Mo_{27}S_{54}$ and $Mo_{27}S_{48}$, the relative orientation of the adsorbed OH is different in the two cases: in the former, both OH^* align in the same direction whereas in the later they do not (see Figure 45, side view). The above results indicate that the presence of S vacancies leads to enhanced adsorption energy of OH at the edges. Now, we turn to the adsorption

of H_2O on a Mo atom of both edges of the two NPs. On $Mo_{27}S_{54}$, H_2O adsorbs at the $(10\bar{1}0)$ edge with an energy of -0.95 eV and (weakly) at $(\bar{1}010)$ edge with -0.21 eV. On $Mo_{27}S_{48}$, the adsorption energies of H_2O are larger on both edges, as compared to that on $Mo_{27}S_{54}$. It adsorbs at the $(10\bar{1}0)$ edge with energy of -2.08 eV and at the $(\bar{1}010)$ edge with -1.10 eV. The overall electrocatalysis reaction process is summarized in figure 46. The above findings show that on both NPs, the adsorption of OH and H_2O at $(\bar{1}010)$ edge are weaker than those at $(10\bar{1}0)$ indicating higher reactivity of the $(10\bar{1}0)$ edge than that of the $(\bar{1}010)$ edge for these initial steps in the electro-catalytic process.

Table 7: Bond lengths of selected atoms in various systems. The Mo-Mo and Mo-S, and Mo-O distances are provided for the atoms indicated by dotted lines, in Figure 45.

System	Mo-Mo	Mo-S	Mo-O	O-O	O-H
H_2O_2(g)	--	---	---	1.471	0.979
$Mo_{27}S_{54}$	3.094	2.311	---	----	---
$Mo_{27}S_{48}$	3.183	2.413	---	----	---
$2OH^*/Mo_{27}S_{54}$	3.213	2.313	1.904	2.985	0.983
$2OH^*/Mo_{27}S_{48}$	3.051	2.385	1.935	2.960	0.984

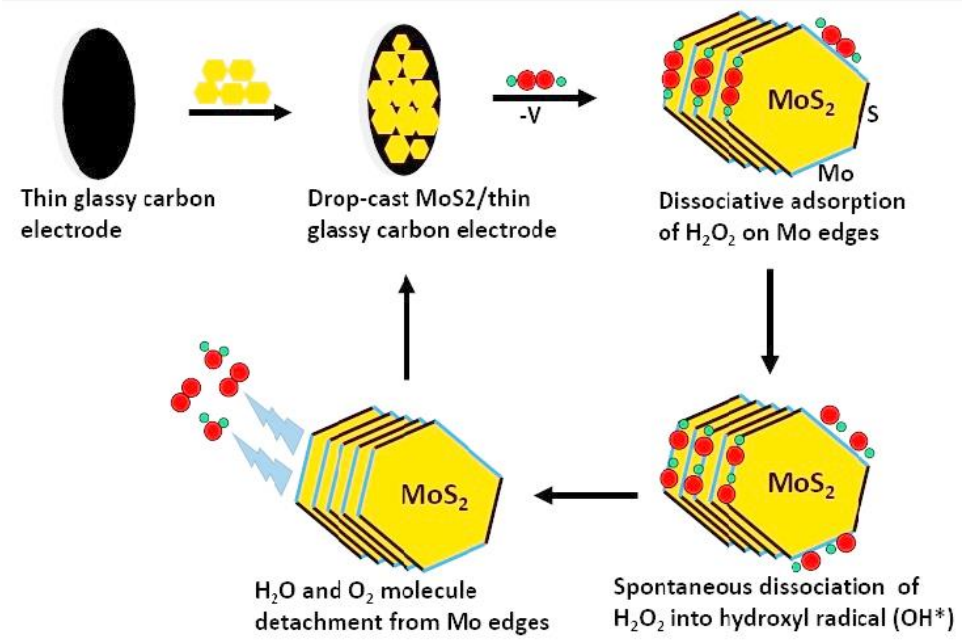

Figure 46: Schematic representation of electrocatalysis of H_2O_2 decomposition at the Mo edge (blue color) of MoS_2 nanoparticle yielding the formation of hydroxyl (OH) radicals, which can further undergo reaction to form intermediates (not shown) and finally form H_2O and O_2.*

4.4 Conclusions

In summary, we report the use of molybdenum disulfide (MoS_2) as an ultra-sensitive multi-role electrochemical platform and its ability to detect therapeutic, pharmaceutical and industrially relevant chemical species; namely: hydrogen peroxide, hypochlorous acid and nitric oxide radicals. 5-7 nm size MoS_2 nanoparticles have shown remarkable, ultra-low sensitivity towards hydrogen peroxide (1 pM), hypochlorous acid (1 nM) and nitric oxide radical (10 nM). These values are lower than the reported values in literature when compared to other detection methods such as electrochemical-based [12, 61, 64], and fluorescent assays [5, 51, 52]. The ultra-low sensing properties of these MoS_2 nanoparticles is a result of higher Mo edge density due to sulfur deficiency, as manifested

from X-ray photoelectron spectroscopy study. DFT-based electronic structure calculations of MoS_2 nanoparticles of several sizes reveal that the sharp, occupied d-state peak near the Fermi level (E_F) tends to smoothen and shift away from E_F with the increase of the size of nanoparticles, indicating larger particles are less catalytically active than the smaller ones. Our DFT calculations further reveal that the spontaneously dissociative adsorption of H_2O_2 occurs at the $(10\bar{1}0)$ edge, and that the adsorption energy of OH^* and H_2O at the $(10\bar{1}0)$ (Mo) edge are higher than those at $(\bar{1}010)$ (S) edge, suggesting Mo edges are electrocatalytically more active than the S-edges. The DFT results also point to the enhancement of chemical activity on the nanoparticle with S-vacancies. Therefore, both S-deficiency and a high density of Mo-edges in small MoS_2 particles contribute to the pico-/nano molar level detection of various chemical species relevant in biology.

CHAPTER FIVE: CONCLUSIONS

This dissertation successfully exhibit the unique bio-catalytic and sensing properties of doped cerium oxide nanoparticles (d-CNPs), cerium oxide thin films (CeO_x) and molybdenum disulfide (MoS_2) nanoparticles. The surface and edge contributions of redox-active materials (d-CNPs, CeO_x and MoS_2) on ROS scavenging and detection have been studied in detail to develop more potent antioxidant and ultra-sensitive sensor platform. Improvement in bio-catalytic and sensing properties is attributed to modification in surface chemistry of functional nanomaterials by introducing defect state in the lattice.

Frist, rare earth element (La, Sm and Er) doped CNPs of 4-7 nm size were prepared via sustainable one-step green synthesis method at room temperature. Synthesized d-CNPs were crystalline in nature and coated with dextran polymer. Energy filtered transmission electron microscopy (EFTEM) study showed the uniform distribution of doping element in cerium oxide lattice. Improvement in Ce^{3+} oxidation state in d-CNPs compared to Dextran-CNPs analyzed using x-ray photoelectron spectroscopy (XPS) indicated the introduction of oxygen vacancies in cerium lattice by trivalent dopants. Enhanced superoxide dismutase (SOD) of d-CNPs tested in both, acidic and basic environment, in comparison to Dextran-CNPs demonstrated that higher Ce^{3+}/Ce^{4+} oxidation state CNPs can efficiently mitigate the effect of ROS. *In vitro* studies revealed that high d-CNPs having higher Ce^{3+}/Ce^{4+} can effectively scavenge intercellular ROS during physiological processes. No cell mortality of healthy non-cancerous HUVAC cells was observed when treated with up to 50 µM concentration of d-CNPs. This finding indicates the specificity of synthesized nanoparticles towards cancerous cells. Thus, combining this synthesis method and appropriate selection of doping element, CNPs of

desired surface chemistry can be designed for specific biological applications. Applications such as a coating on orthopedic implants and implantable biosensors require continuous integrated film of redox–active material due to the bio-corrosion. Also, friction of implant, which can dislodge particles from the implant surface. Therefore, controlled and continuous cerium oxide thin films have been deposited and their thickness dependent surface chemistry have been studied

Cerium oxide thin films (CeO_x) were deposited by atomic layer deposition (ALD) at 275 °C. Thickness of CeO_x films was varied by increasing the ALD deposition cycles from 50 to 1000. The CeO_x growth rate was 0.34 Å/cycle for two consecutive pulses of $Ce(iPrCp)_3$ of 2.5 s followed one pulse of 50 ms of H_2O. Thickness of CeOx films were 2 , 7, 17 and 33 nm for 50, 200, 500 and 1000 cycles, respectively, measured by x-ray reflectivity. A linear relationship between film thickness and number of deposition cycles showed the self-limiting character of CeO_x film. Phase analysis of CeO_x films revealed the presence of Ce_2O_3 in 2 nm films, whereas higher order thickness films consisted of CeO_2. The presence of organic residue in CeOx films can be attributed to the incomplete ALD cycle at the end of the deposition process. The ratio of Ce^{3+} to Ce^{4+} measured from deconvoluted Ce (3d) spectra was 1 for 2 nm film, whereas it varied from 0.30-0.37 for higher thickness films. Improved catalase activity of films with increasing thickness support that catalase activity is a function of the surface [Ce^{4+}] and films rich in Ce^{4+} are more catalase active. Furthermore, sensitivity of 200 cycles ALD CeO_x film for H_2O_2 detection is 9.04 A•L/g•cm^2•s. This study opens the avenue for CeO_x coatings in a number of potential applications in bioimplants (prosthetics), sensors and downturn hazardous chemicals such as methyl orange for environmental remedy. However, presence of

ascorbic acid interfere in the H_2O_2 detection. Thus, selectivity becomes an issue for cerium oxide based sensors.

To improve the selectivity of sensors, MoS_2 nanoparticle-based ultra-sensitive electrochemical sensor platform was developed for ROS detection is ultra-low concentration. Concentrations as low as 1 pM have been detected utilizing liquid exfoliated 5-7 nm MoS_2 particles as transducing layer. We have successfully detected H_2O_2, HOCl and NO*. No interference from ascorbic acid have been observed during H_2O_2 detection which is highly important for sensor development. High sensitivity and low concentration of therapeutic, pharmaceutical and industrially relevant chemical species have been attributed to S-deficiency at the layered MoS_2 edges. S to Mo ratio of 1.83 have been analyzed from XPS study. Furthermore, density functional theory (DFT) have revealed that nano-size particles are more catalytically active than larger particles because occupied d-state peak near fermi level become flat for larger size particles. Furthermore, DFT calculation reveals that Mo-edges are preferred site for H_2O_2 adsorption than S-edges and spontaneous dissociation of H_2O_2 occur at Mo-edges. Due to higher adsorption energy of OH* and H_2O at Mo-edges, molecules does not poison catalytically active sites.

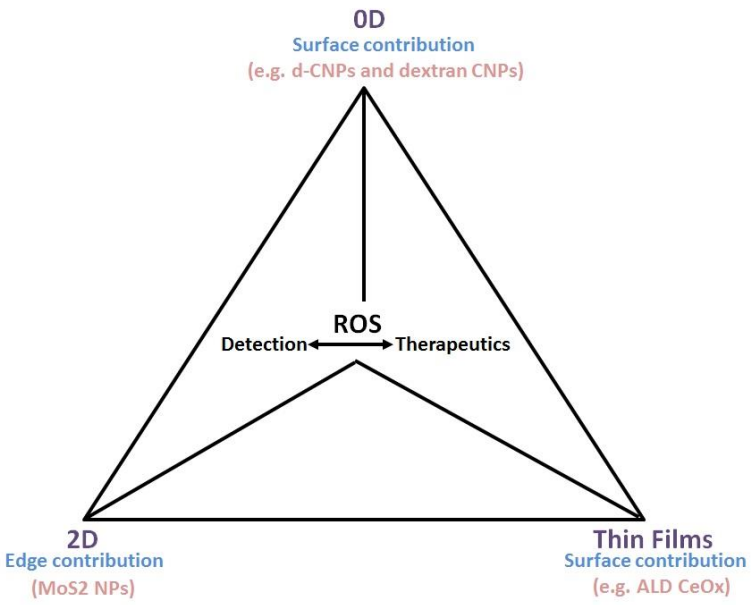

Figure 47: Schematic diagram showing the contribution of different studies on early ROS detection and their scavenging.

In summary, surface contributions of d-CNPs (0D) and ALD CeO_x (thin films) and edge contributions of MoS_2 NPs (2D) on ROS detection and scavenging (Figure 47) have been studied. It is clearly evident from the above-mentioned findings that lattice defects in materials at the nanometer scale give rise to unique properties, and open new frontiers for scientists to cut across traditional materials and venture into nanotechnology to develop therapeutic nanomedicine and advanced detection platform for pharmaceutical, environmental and industrially relevant chemical species.

FUTURE SCOPE

Following studies can be carried out to further extend the scope of this dissertation.

1. *In vivo* study in mice model simulating melanoma and ovarian cancer condition to understand the efficacy of polymer coated doped CNPs in comparison to dextran-coated and bare CNPs

2. Development of electrochemical and colorimetric sensor by immobilizing polymer coated doped CNPs on high aspect ratio surfaces

3. Growth kinetics and process optimization of atomic layer deposition of rare earth element doped CeO_x. Successful doping of rare earth elements in ALD CeO_x thin films will allow to effectively control the surface chemistry of CeO_x for their potential applications in bio-sensing

4. Fabrication of CeO_x transducing layer based electrochemical transistor integrated with microfluidic channel for continuous *in vivo* monitoring of ROS in blood and plasma

5. Molecular modeling of MoS_2-H_2O_2 interaction to understand the reaction mechanism and intermediate products

6. Immobilization of 5-7 nm size MoS_2 particles on high aspect ratio surfaces such as nanopillars to achieve femtomolar detection

APPENDIX A: PUBLICATIONS DURING THIS DISSERTATION

Journal of
Materials Chemistry B

PAPER

View Article Online
View Journal

CrossMark

Cite this: DOI: 10.1039/c6tb00396f

Controlling the surface chemistry of cerium oxide nanoparticles for biological applications†

Ankur Gupta,[a] Soumen Das,[a] Craig J. Neal[a] and Sudipta Seal*[ab]

Received 16th February 2016,
Accepted 15th March 2016

DOI: 10.1039/c6tb00396f

www.rsc.org/MaterialsB

The catalytic activity of cerium oxide nanoparticles (CNPs) depends on the surface Ce^{3+}/Ce^{4+} oxidation state. CNPs with a higher Ce^{3+} to Ce^{4+} ratio, oxygen vacancies and higher superoxide dismutase (SOD) mimetic activity are more effective against diseases associated with oxidative stress or inflammation. CNPs with a lower Ce^{3+}/Ce^{4+} ratio show higher catalase mimetic activity and possess anticancer/antibacterial activity. However, different synthesis methods of CNPs and capping agents/surface coatings result in various Ce^{3+}/Ce^{4+} oxidation states, thus limiting the use of particular CNPs for specific biological applications. In this study, we have shown that by selecting an appropriate doping method we can control the surface Ce^{3+}/Ce^{4+} oxidation state to tune the catalytic activity and biological response. Importantly, superior SOD mimetic activity and efficient reactive oxygen species scavenging capability of one-step synthesized CNPs are linked to a uniform distribution of dopants in the CNP lattice and changes in the surface Ce^{3+}/Ce^{4+} oxidation state.

Introduction

Cerium oxide is the most abundant lanthanide metal oxide. It is widely used in oxygen sensors,[1,2] catalytic converters[3,4] and solid oxide fuel cells.[5] The discovery of the redox-active nature (low redox potential) of cerium ions (Ce^{3+} and Ce^{4+}) present at the surface of cerium oxide nanoparticles (CNPs) has opened up new avenues for biomedical applications,[6–11] electrochemical bio-sensors,[12] radiation protection,[13] corrosion-resistant coatings,[14] *etc.* Researchers have also demonstrated the unique regenerative antioxidant properties of CNPs through *in vitro* model systems; in particular, the ability of the CNPs to scavenge superoxide, hydrogen peroxide radicals, and reactive nitrogen species such as nitric oxide and peroxynitrite has been demonstrated.[15–17] Dowding *et al.*[18] have reported in a detailed study that CNPs inhibit the production of endogenous peroxynitrite and prevent Aβ-induced mitochondrial fragmentation and neuronal cell death by neuronal internalization. This is followed by CNPs accumulation in the proximity of the mitochondrial and plasma membranes. The concentration of protein tyrosine nitration and reactive nitrogen species in neurons exposed to peroxynitrite decreases with an increase in the concentration of CNPs having a higher Ce^{4+} oxidation state, thus preventing mitochondrial dysfunction and neuronal cell death is suggestive of a potential treatment for neurodegeneration disease.[7,18] Citrate/EDTA coated CNPs (size 3 nm) have also demonstrated their effectiveness in targeting affected brain tissues in an experimental autoimmune encephalomyelitis (EAE) induced rat model of multiple sclerosis by passing through the blood–brain barrier which results in the decrease of reactive oxygen species (ROS).[7,19] The results of the *in vivo* study of ischemic shock (caused by ROS) induced rats treated with 3–4 nm phospholipid PEGylated CNPs show an increased concentration of CNPs in the brain as compared to liver and kidneys; thus revealing the therapeutic protection towards the ischemic brain tissue due to a mixed oxidation state (Ce^{3+} and Ce^{4+}).[7,20]

However, the antioxidant properties of CNPs are highly dependent on the particle size as well as surface coating.[21] It is clearly evident from the above mentioned studies that the scavenging ability of CNPs and their enzyme-mimetic activities towards different radicals are dependent on their surface oxidation state. Radiation treatment,[22] doping[23,24] and high temperature treatment[25] are common methods used for tuning the surface oxidation state or catalytic activity of CNPs. Kumar *et al.*[22] irradiated (2 MeV helium ions) single and polycrystalline cerium oxide films grown by molecular beam epitaxy and reported a 13% and 19% increase in trivalent cerium concentrations, respectively. Another study reported by Kumar *et al.*[23] showed that Eu doping in the cerium oxide lattice by a co-precipitation method results in a Ce^{3+} oxidation state (18.3% to 23.5% for 1 mole% Eu-CNPs and 30 mole% Eu-CNPs, respectively) and when subjected to high temperature annealing treatment, the Ce^{3+} oxidation state concentration decreased to 14.0%. The defect concentration

[a] Advanced Materials Processing and Analysis Center, NanoScience Technology Center and Department of Materials Science and Engineering, University of Central Florida, Orlando, FL-32816, USA. E-mail: Sudipta.Seal@ucf.edu; Tel: +1-4078230565
[b] College of Medicine, University of Central Florida, Orlando, FL-32816, USA
† Electronic supplementary information (ESI) available. See DOI: 10.1039/c6tb00396f

Progress in Materials Science 73 (2015) 44–126

Contents lists available at ScienceDirect

Progress in Materials Science

journal homepage: www.elsevier.com/locate/pmatsci

Recent development in 2D materials beyond graphene

Ankur Gupta [a,b,c,1], Tamilselvan Sakthivel [a,b,c,1], Sudipta Seal [a,b,c,d,*]

[a] Advanced Materials Processing and Analysis Center, University of Central Florida, Orlando, FL 32816, USA
[b] Nanoscience Technology Center, University of Central Florida, Orlando, FL 32816, USA
[c] Department of Materials Science and Engineering, University of Central Florida, Orlando, FL 32816, USA
[d] College of Medicine, University of Central Florida, Orlando, FL 32816, USA

ARTICLE INFO

Article history:
Received 16 January 2014
Received in revised form 18 February 2015
Accepted 24 February 2015
Available online 14 March 2015

Keywords:
Materials beyond graphene
2D layers importance/uniqueness
TMD layers
h-BN
Silicene and germanene
Oxides and hydroxides
Group IV and III-V elements
Kaolinite

ABSTRACT

Discovery of graphene and its astonishing properties have given birth to a new class of materials known as "2D materials". Motivated by the success of graphene, alternative layered and non-layered 2D materials have become the focus of intense research due to their unique physical and chemical properties. Origin of these properties ascribed to the dimensionality effect and modulation in their band structure. This review highlights the recent progress of the state-of-the-art research on synthesis, characterization and isolation of single and few layer nanosheets and their assembly. Electronic, magnetic, optical and mechanical properties of 2D materials have also been reviewed for their emerging applications in the area of catalysis, electronic, optoelectronic and spintronic devices; sensors, high performance electrodes and nanocomposites. Finally this review concludes with a future prospective to guide this fast evolving class of 2D materials in next generation materials science.

Contents

* Corresponding author at: Advanced Materials Processing and Analysis Center, University of Central Florida, Orlando, FL 32816, USA. Tel.: +1 4075928565.
E-mail address: Sudipta.Seal@ucf.edu (S. Seal).
[1] Ankur Gupta and Tamilselvan Sakthivel have contributed equally in this review article.

http://dx.doi.org/10.1016/j.pmatsci.2015.02.002
0079-6425/© 2015 Published by Elsevier Ltd.

Research Highlights

For reprint orders, please contact: reprints@futuremedicine.com

Nanomedicine

Redox-active nanoparticles in combating neurodegeneration

Ankur Gupta[1], Soumen Das*[1] & Sudipta Seal[1,2]

[1]Advanced Material Processing & Analysis Center, Nanoscience Technology Center & Department of Materials Science & Engineering, University of Central Florida, Orlando, FL 32816, USA
[2]College of Medicine, University of Central Florida, Orlando, FL 32816, USA
*Author for correspondence: soumen.das@ucf.edu

Effect of size & surface coating on redox/antioxidant property of cerium oxide nanoparticle

Evaluation of: Lee SS, Song W, Cho M *et al.* Antioxidant properties of cerium oxide nanocrystals as a function of nanocrystal diameter and surface coating. *ACS Nano* 7, 9693–9703 (2013).

Over 10 years, cerium oxide nanoparticles (CNPs) have been studied as an antioxidant for neuroprotection, radiation protection, biosensor, bio-imaging due to its dual valence states (Ce^{3+} and Ce^{4+}) and defect structure at the nanoscale. Despite the bright prospects of CNPs in nanomedicine [1–4], one fundamental question has always remained unanswered: "Redox mechanism and its stoichiometry in the presence of hydrogen peroxide." Fenton Habor/Weiss reaction has been proposed as redox mechanism for scavenging peroxide radicals using different polymer coated (Oleic acid, poly(acrylic acid)-octylamine [PAA-OA], polymaleican-hybride-1-octade-cene [PMAO] and polyethyleneimine [PEI]) CNPs of size 4–8 nm. The characteristic 2:1:1 ratio of H_2O_2 to Ce^{3+} to O_2 supports the Fenton-type reaction over direct reduction of peroxides in the biological environment reported in the literature [5]. The ultra-small-size CNPs have been proposed for better peroxide-scavenging activity with higher Ce^{3+} on the particle surface of the CNPs. In contrary, some literature has shown that CNPs with higher Ce^{4+} can scavenge H_2O_2 more efficiently than CNPs with higher Ce^{3+} whereas higher Ce^{3+} concentration imparts superoxide dismutase activity [6]. CNPs are often coated with biocompatible polymers to obtain the stability of the suspension, biodistribution and pharmacokinetics for *in vivo* applications; therefore, choice of polymer coating is particularly important from a nanomedicine design point of view. The CNPs with oleic acid coating showed nine-times higher antioxidant performance than Trolox (a water soluble analog of vitamin E). Interestingly, CNPs coated with PMAO had decrease in the catalytic activity compared with oleic acid coated CNPs, therefore, eliciting that choice of polymer and thickness of polymer coating are very important for CNPs antioxidant capacity. It can be concluded that synthesis procedure (surface chemistry, especially Ce^{3+}/Ce^{4+} ratio), particle morphology, careful selection of coating polymer and optimization of coating thickness are important factors for designing the CNP-based antioxidants [7–9].

Shielding brain toward autoimmune degenerative disease

Evaluation of: Heckman KL, DeCoteau W, Estevez A *et al.* Custom cerium oxide nanoparticles protect against a free radical mediated autoimmune degenerative disease in the brain. *ACS Nano* 7, 10582–10596 (2013).

Generation and accumulation of reactive oxygen species (ROS) and reactive nitrogen species (RNS) are responsible for oxidizing proteins, lipids and DNA and result in disease such as neurodegeneration, atherosclerosis and cancer, among others. Cerium oxide nanoparticles (CNPs) have established themselves as antioxidant in therapeutic applications because of targeting ROS and RNS in *in vitro* and *in vivo* studies [10,11]. Current research focus is to explore if CNPs can scavenge ROS in different neurodegenerative

Future Medicine part of fsg

Carbon 105 (2016) 529–543

Contents lists available at ScienceDirect

Carbon

journal homepage: www.elsevier.com/locate/carbon

Functional NiAl-graphene oxide composite as a model coating for aerospace component repair

David Ward [a, 1], Ankur Gupta [a, 1], Shashank Saraf [a], Cheng Zhang [b], Tamil Selvan Sakthivel [a], Swetha Barkam [a], Arvind Agarwal [b], Sudipta Seal [a, *]

[a] Advanced Materials Processing and Analysis Center, Nanoscience Technology Center, Department of Materials Science and Engineering, University of Central Florida, Orlando, FL 32816, USA

[b] Advanced Materials Engineering Research Institute, Department of Mechanical and Materials Engineering, Florida International University, Miami, FL 33174, USA

ARTICLE INFO

Article history:
Received 15 January 2016
Received in revised form
5 April 2016
Accepted 11 April 2016
Available online 29 April 2016

ABSTRACT

Metallic plasma sprayed coatings are widely used in the aerospace industry to repair engine components. However, the inherent defects in coatings limit such repairs and reduce the service life of the parts. In this study, to improve the serviceability and mechanical properties of plasma sprayed coatings, multi-layered graphene oxide (GO) have been introduced as a reinforcement. The novelty of this work lies in the processing of the plasma sprayed, GO-reinforced metallic composite coatings. Commercially available Ni–Al powders were used with GO reinforcement, resulting in an increase in the mechanical properties. Retention of the GO was made successful by installing a customized inert argon shroud to prevent the combustion of GO. The HRTEM image confirms a homogeneous distribution of GO within the metallic matrix. We report an improvement in hardness and tensile adhesion strength, and a reduction in residual strain and the coefficient of friction. The results presented in this article prove that GO can successfully be retained as an additive in thermal spray coatings and provide opportunities for low-cost manufacturing or repair.

1. Introduction

Coatings are widely used in the aerospace, automotive, and shipbuilding industries to enhance the surface properties of new components and in the repair of worn components [1,2]. Certain metallic, ceramic, and polymeric coatings provide excellent resistance to wear, heat, or corrosion [1,3]. Mostly, plasma spray coatings are used for unique repairs on parts that were originally cast or rolled or other pre-fabricated components [1–3]. For example, many depot level repairs on gas turbine components require restoring worn metal back to original dimension, which can cost several billion dollars per year. Several methods such as electroplating, welding and plasma spraying, followed by machining are done to obtain the required dimension [3]. However, each process has its benefits and drawbacks. For instance, electroplated coatings are smooth but brittle in nature. Welding is certainly a better option from a chemical waste standpoint and this method produces the strongest and thickest possible build-up. However, the required heating of the base metal usually changes the material's microstructure and can affect mechanical properties [4]. Compared to electroplating and welding, plasma spraying is a cost-effective and versatile method for producing an even and a machinable coating on large areas. However, residual stresses develop as the coating thickness increases, limiting the maximum thickness [3,5]. It is thus clear that each process has many limitations. Further, some repairs cannot be done by any process; these require replacement with a new, expensive part. There is a great incentive for limiting the inherent weaknesses of plasma spray coatings to allow for more parts to be repaired. Special attention has been paid to substrate preparation, process parameters, and powder composition in order to optimize the properties of plasma spray coatings. Specifically, stand-off distance (SD), plasma power, current, voltage, carrier gas flow rate, primary and secondary gas flow rate have been investigated [3,6–8]. An ideal plasma spray coating should fulfill the application requirement. Therefore, optimization of parameters is always necessary. Optimum processing parameters of plasma spray

* Corresponding author.
E-mail address: Sudipta.Seal@ucf.edu (S. Seal).
[1] David Ward and Ankur Gupta have contributed equally to this paper.

http://dx.doi.org/10.1016/j.carbon.2016.04.025
0008-6223/© 2016 Published by Elsevier Ltd.

Acta Materialia 126 (2017) 124–13

Contents lists available at ScienceDirect

Acta Materialia

journal homepage: www.elsevier.com/locate/actamat

Full length article

Reactive wetting and filling of boron nitride nanotubes by molten aluminum during equilibrium solidification

Pranjal Nautiyal [a], Ankur Gupta [b], Sudipta Seal [b], Benjamin Boesl [a], Arvind Agarwal [a, *]

[a] Plasma Forming Laboratory, Department of Mechanical and Materials Engineering, Florida International University, Miami, FL 33174, USA
[b] AMPAC and Nanoscience Technology Center, Department of Materials Science and Engineering, University of Central Florida, Orlando, FL 32816, USA

ARTICLE INFO

Article history:
Received 6 November 2016
Received in revised form
14 December 2016
Accepted 14 December 2016

Keywords:
Boron nitride nanotube (BNNT)
Aluminum
Interface wetting
Capillarity
Solidification

ABSTRACT

Interactions between long boron nitride nanotube (BNNT) fibrils and molten aluminum (Al) pool are probed in this study to assess the feasibility of fabricating composite materials by solidification route. BNNTs were found to survive high temperature and reactive conditions present in molten aluminum. Very limited interfacial reaction was observed, resulting in the formation of AlN, AlB_2 and AlB_{10} in trace amounts. AlN was the principal reaction product, resulting in improved interfacial wetting. Calculations based on surface energies revealed improved work of interfacial adhesion due to AlN formation. BNNTs were found to be well integrated in the aluminum matrix, signifying AlN induced excellent wetting. We also report capillarity-induced high temperature filling of BNNT by molten Al. The filling was promoted by AlN formation. In addition, formation of B-rich AlB_{10} phase inside the nanotube was observed. Nanotube filling by metal and subsequent reaction to form nano-ceramic phases is expected to alter mechanical properties of the cast Aluminum–BNNT composites. This study establishes the suitability of solidification route for developing high strength Al-BNNT composites in future.

1. Introduction

Aluminum (Al) and its alloys are undisputedly the most widely used material system for automotive and aerospace applications due to their light weight and superior specific mechanical properties. Al alloys with reasonable strength have been engineered; however, their load bearing capability still falls short for applicability in critical structural components. As a result, steel and costlier Ti alloys have to be employed, resulting in increased weight, more fuel consumption and higher cost of operation. To mitigate this, considerable research efforts have been undertaken lately to develop high strength and light weight Al composites [1,2]. Carbon Nanotube (CNT) reinforced Al composites have been actively researched in past two decades due to strengthening effect of nanotubes [3–14]. Despite their excellent mechanical properties, integration of CNTs in Al matrix is a major challenge due to their poor dispersion [3,4]. Moreover, CNTs are reported to undergo oxidation at temperatures exceeding 400 °C [15,16]. Therefore, most of the high temperature processing techniques, like casting, hot rolling and forging cannot be easily employed without damaging CNTs. Boron Nitride Nanotube (BNNT), a structural analogue of CNT with alternate B and N atoms has as attractive mechanical properties as CNT [17–19]. They are reported to exhibit highly impressive elastic modulus of ~1 TPa and a tensile strength of ~61 GPa [20–22]. In addition, BNNT is resistant to oxidation at temperatures as high as 1000 °C [15,16,23]. Since the melting point of Al is ~660 °C, this opens up the possibility of manufacturing BNNT reinforced Al composites by casting. Conventionally, casting has been at the center stage of the metallurgical processes due to its capability of fabricating complex shapes easily and economically. High temperature oxidation resistance of BNNT gives it an edge over CNT as a reinforcement candidate for Al composites synthesized by casting route.

BNNT based Al composites have been fabricated by powder metallurgical techniques such as pressureless sintering [24], spark plasma sintering [25–27], high pressure torsion technique [27,28] and cold rolling [25,26], as well as physical vapor deposition processes, such as magnetron sputtering [29] and ion implantation [30]. It is noteworthy that molten route fabrication of Al-BNNT composites has not received much attention by researchers. Yamaguchi et al. reported Al-BNNT ribbons by melt spinning in an Ar atmosphere [31]. The composite ribbons with varying BNNT fractions (0.5–3.0 wt%) were fabricated by pelletizing Al-BNNT

* Corresponding author.
E-mail address: agarwala@fiu.edu (A. Agarwal).

http://dx.doi.org/10.1016/j.actamat.2016.12.034
1359-6454/

Received: 28 August 2016 | Accepted: 3 January 2017
DOI: 10.1111/jace.14778

ORIGINAL ARTICLE

Journal of the American Ceramic Society

Solid solution synthesis of tantalum carbide-hafnium carbide by spark plasma sintering

Cheng Zhang[1] | Ankur Gupta[2] | Sudipta Seal[2] | Benjamin Boesl[1] | Arvind Agarwal[1]

[1]Plasma Forming Laboratory, Department of Mechanical and Materials Engineering, Florida International University, Miami, Florida, USA
[2]AMPAC, NSTC, University of Central Florida, Orlando, Florida, USA

Correspondence
Arvind Agarwal, Plasma Forming Laboratory, Department of Mechanical and Materials Engineering, Florida International University, Miami, FL, USA.
Email: agarwala@fiu.edu

Abstract

Solid solutions of Tantalum carbide (TaC) and Hafnium carbide (HfC) were synthesized by spark plasma sintering. Five different compositions (pure HfC, HfC- 20 vol% TaC, HfC- 50 vol% TaC, HfC- 80 vol% TaC, and pure TaC) were sintered at 1850 °C, 60 MPa pressure and a holding time of 10 min without any sintering aids. Near-full density was achieved for all samples, especially in the HfC-contained samples. The porosity in pure TaC samples was caused by the oxygen contamination (Ta_2O_5) on the starting powder surface. The addition of HfC increased the overall densification by transferring the oxygen contamination from TaC surface and forming ultrafine HfO_2 and Hf-O-C grains. With the increasing HfC concentration, the overall grain size was reduced by 50% from HfC- 80 vol % TaC to HfC-20 vol% TaC sample. The solid solution formation required extra energy, which restricted the grain growth. The lattice parameters for the solid solution samples were obtained using X-ray diffraction which had an excellent match with the theoretical values computed using Vegard's Law. The mechanical properties of the solid solution samples outperformed the pure TaC and HfC carbides samples due to the increased densification and smaller grain size.

KEYWORDS
HfC, solid solution, spark plasma sintering, TaC, Vegard's law

1 | INTRODUCTION

Tantalum carbide and hafnium carbide belong to the group of ultrahigh temperature ceramics, which possess high melting points, high densities, high hardness, high elastic moduli, and low fracture toughness. Hence, they can be utilized under extreme conditions for applications such as rocket thrust lining materials or leading edges of hypersonic vehicles where temperatures can exceed 2000°C.[1-3] TaC and HfC have been extensively studied, and these studies were mainly focused on processing parameters and oxidation resistance of the individual compositions. Sintering aids are almost inevitable in synthesis of TaC and HfC due to the low self-diffusivity and strong covalent bonding of these two ceramics. In previous studies, sintering aids like carbon allotropes, disilicides, and carbides are used in TaC or HfC synthesis.[4-10] Sintering aids will not only improve the material's densification, but also introduce new secondary phases. Although secondary phases may not necessarily jeopardize the material properties, they increase the complexity of the system, limiting the true understanding of the intrinsic properties. Oxidation resistance is another concern for these two carbides. TaC has a relatively poor oxidation behavior, it fully oxidized at around 850°C after 5 hour in pure oxygen and formed tantalum pentoxide.[11] The melting point of Ta_2O_5 is ~1872°C,[12] which liquefies in high-temperature oxygen-rich environments. However, when TaC is used in oxygen deficient environment, such as aluminized propellant solid rocket motor applications, TaC has been identified as the best performing ceramic lining material.[13] On the other hand, HfC has outstanding high-temperature oxidation resistance in oxygen-rich environments. Hafnium

ADVANCED SCIENCE NEWS
www.advancedsciencenews.com

small

Magnetic Nanoparticles

High-Throughput, Protein-Targeted Biomolecular Detection Using Frequency-Domain Faraday Rotation Spectroscopy

Richard J. Murdock, Shawn A. Putnam, Soumen Das, Ankur Gupta, Elyse D. Z. Chase, and Sudipta Seal*

A clinically relevant magneto-optical technique (fd-FRS, frequency-domain Faraday rotation spectroscopy) for characterizing proteins using antibody-functionalized magnetic nanoparticles (MNPs) is demonstrated. This technique distinguishes between the Faraday rotation of the solvent, iron oxide core, and functionalization layers of polyethylene glycol polymers (spacer) and model antibody–antigen complexes (anti-BSA/BSA, bovine serum albumin). A detection sensitivity of ≈10 pg mL^{-1} and broad detection range of 10 pg mL^{-1} $\lesssim c_{BSA} \lesssim$ 100 µg mL^{-1} are observed. Combining this technique with predictive analyte binding models quantifies (within an order of magnitude) the number of active binding sites on functionalized MNPs. Comparative enzyme-linked immunosorbent assay (ELISA) studies are conducted, reproducing the manufacturer advertised BSA ELISA detection limits from 1 ng mL^{-1} $\lesssim c_{BSA} \lesssim$ 500 ng mL^{-1}. In addition to the increased sensitivity, broader detection range, and similar specificity, fd-FRS can be conducted in less than ≈30 min, compared to ≈4 h with ELISA. Thus, fd-FRS is shown to be a sensitive optical technique with potential to become an efficient diagnostic in the chemical and biomolecular sciences.

1. Introduction

Biomarker detection, molecular recognition, and quantification of the density and activity of binding sites are critical to a wide variety of applications, including the engineering of ultrasensitive chemical sensors for national security,[1,2] electrochemical reactions in energy technologies,[3] and molecular detection with high specificity in biomedical research.[4] High-throughput diagnostics are critical in many fields of science and engineering, especially those that can be extended

R. J. Murdock
Health Sciences and Technology (HST)
Institute for Medical Engineering and Science (IMES)
Massachusetts Institute of Technology and Harvard University
77 Massachusetts Avenue
76-679, Cambridge, MA 02139, USA
Prof. S. A. Putnam
Department of Mechanical and Aerospace Engineering
University of Central Florida
P.O. Box, 162450, ENGR 1, Rm. 213, Orlando, FL 32816, USA
E-mail: Shawn.Putnam@ucf.edu

Dr. S. Das, A. Gupta, Prof. S. Seal
Department of Materials Science and Engineering
Advanced Materials Processing and Analysis Center, (AMPAC)
Nanoscience Technology Center (NSTC)
University of Central Florida
P.O. Box 162455, ENGR 1, Rm. 207, Orlando, FL 32816, USA
E. D. Z. Chase
Department of Mechanical Engineering and Applied Mechanics
University of Pennsylvania
229, Towne Building, 220 South 33rd Street
Philadelphia, PA 19104, USA

DOI: 10.1002/smll.201602862

Advanced Review

Adjuvants in micro- to nanoscale: current state and future direction

Ankur Gupta,[1] Soumen Das,[1] Brian Schanen[2] and Sudipta Seal[1,3]*

Adjuvants have been used in vaccines for over 70 years to promote long-lived and sterilizing immunity. Since then, various adjuvant systems were developed by combining nanotechnology with natural and/or synthetic immunomodulatory molecules. These systems are biocompatible, immunogenic, and possess higher antigen carrying capacity. This article showcases advancements made in the adjuvant systems formulations, their synthesis routes, and the improvement of these adjuvants have brought in response to combat against ongoing global health threats such as malaria, hepatitis C, universal influenza, and human immunodeficiency virus. This review also highlights the interaction of adjuvants with the delivery of antigens to cells and unfolds mechanism of actions. In addition, this review discusses the physicochemical factors responsible for the efficient interaction of nanoadjuvants with antigen receptors to develop more effective, less reactogenic, and multifunctional systems for the next generation vaccines.

How to cite this article:
WIREs Nanomed Nanobiotechnol 2015. doi: 10.1002/wnan.1354

INTRODUCTION

Since the discovery of conferred immunity/vaccines in the early 1870s, millions of human and animal lives have been saved. Vaccines continue to be the safest, most cost effective, and reliable tool to combat or even eradicate infectious diseases such as polio, smallpox, diphtheria, yellow fever, and influenza. However, antigens alone are often unable to provide the required immune potency. Therefore, adjuvants have been used in vaccines for over 70 years to promote long-lived and sterilizing immunity. Recently, adjuvant formulations have seen innovation by utilizing nanotechnology to drive specific immunomodulatory programs, and to enhance immunogenicity through higher antigen carrying capacity. Adjuvants are often described as nonimmunogenic substances necessary to promote the appropriate protective and antigen-specific immune response to a vaccine antigen.[1,2] Thus, adjuvants are added in vaccines to enhance their efficacy. Currently, over 100 vaccine adjuvants have been cataloged in the Vaxjo database, many of which have been critical to the efficacy of over 380 vaccines formulated to combat over 81 pathogens, cancers, or allergies. Adjuvants are classified based on size, chemistry (mineral or organic), and synthesis method. However, classification of adjuvants based on generation was considered the most meaningful.[3] Aluminum salts (alum), Freund's incomplete adjuvant (water-in-oil emulsion, W/O), MF59 (oil-in-water emulsion, O/W), liposomes (lipid vesicles), and flagellin have been classified as classical and generation 1 adjuvants.[3,4] Examples of generation 2 adjuvants are AS01, AS02, AS03, and AS04 immunostimulating complex (ISCOM); CpG [a DNA motif found in viral DNA and acknowledged by toll-like receptor 9 (TLR9)], to name a few. These adjuvants represent combinations of classical/conventional adjuvants and immunomodulatory molecules [monophosphoryl lipid A (MPL A), saponin-type detergent QS21, etc.].[3] However, the addition of small-molecule immune potentiators into conventional adjuvants adds to the complexity and prolongs

*Correspondence to: Sudipta.Seal@ucf.edu

[1]Advanced Materials Processing and Analysis Center, NanoScience Technology Center and Department of Materials Science and Engineering, University of Central Florida, Orlando, FL, USA

[2]Sanofi Pasteur, VaxDesign Campus, Orlando, FL, USA

[3]College of Medicine, University of Central Florida, Orlando, FL, USA

Conflict of interest: The authors have declared no conflicts of interest for this article.

APPENDIX B: COPYRIGHT PERMISSION TO REUSE PUBLISHED LITERATURE

Ankur Gupta

From: CONTRACTS-COPYRIGHT (shared) <Contracts-Copyright@rsc.org>
Sent: Friday, March 10, 2017 8:39 AM
To: Ankur Gupta
Subject: RE: Re-use permission for article J. Mater. Chem. B, 2016,4, 3195-3202 DOI: 10.1039/C6TB00396F

Dear Ankur,

The Royal Society of Chemistry (RSC) hereby grants permission for the use of your paper(s) specified below in the printed and microfilm version of your thesis. You may also make available the PDF version of your paper(s) that the RSC sent to the corresponding author(s) of your paper(s) upon publication of the paper(s) in the following ways: in your thesis via any website that your university may have for the deposition of theses, via your university's intranet or via your own personal website. We are however unable to grant you permission to include the PDF version of the paper(s) on its own in your institutional repository. The Royal Society of Chemistry is a signatory to the STM Guidelines on Permissions (available on request).

Please note that if the material specified below or any part of it appears with credit or acknowledgement to a third party then you must also secure permission from that third party before reproducing that material.

Please ensure that the thesis states the following:

Reproduced by permission of The Royal Society of Chemistry

and include a link to the paper on the Royal Society of Chemistry's website.

Please ensure that your co-authors are aware that you are including the paper in your thesis.

Regards,

Antonella

Antonella Tesoro
Customer Sales Support
Contracts & Copyright
Royal Society of Chemistry
Thomas Graham House,
Science Park, Milton Road,
Cambridge CB4 0WF
Tel. +44 (0) 1223 432 675
tesoro a@rsc.org

Main Reception Tel. +44 (0) 1223 42 0066
www.rsc.org

Winner of The Queen's Awards for Enterprise, International Trade 2013

- **What does IOP Publishing consider a "Personal Website" to be?** IOP Publishing considers a '**Personal Website**' to be a "website and/or blog relating to the author and their work, the content of which is controlled by them and (i) may be on their personal page on their institution or department's website or (ii) may be hosted by them at a separate IP address or mobile site altogether, which could be linked directly to their institution's or department's website. It does not include their institution's subject or department pages, an institutional or subject repository or a page on a Scientific Social Network or any form of commercial site."

- **May I post the Author's Original and/or the Accepted Manuscript on my institution's/employer's website?** You may post the Author's Original on your institution's/employer's website at any time after acceptance of your article.Following expiry of the Embargo Period, you may post the Accepted Manuscript on your institution's/employer's website, but not under any form of open access or Creative Commons Licence and only where any copyright notice is not deleted or modified.Once the Final Published Version has been published, you should add citation details, a link to the Version of Record and the following statement of provenance: "This is an author-created, un-copyedited version of an article accepted for publication/published in [insert name of journal]. IOP Publishing Ltd is not responsible for any errors or omissions in this version of the manuscript or any version derived from it. The Version of Record is available online at [insert DOI]." You may not post the Final Published Version on any website, unless it has been published on a gold open access basis after payment of an article publication charge.

- **May I post to another publisher's website or commercial third party websites?** You may not post the Accepted Manuscript, Final Published Version or Version of Record to any other publisher website or commercial third party websites.

Abstracts – Subscription Articles

- **May I re-use the abstract of an article?** Yes, article abstracts can be re-used freely. However, no changes may be made to the abstract. Any links, brands, trademarks, or copyright notices embedded in the abstract must remain intact. The abstract should provide a link, via DOI, back to the Version of Record on IOPscience.

- **May I post the abstract to a non-commercial website?** You may post the abstract at any time after publication of the Final Published Version, on any non-commercial third party website but not on the websites of other publishers, provided in all cases that you include a link via DOI to the abstract page of the article on IOPscience, and no changes are made to the abstract.

ADDITIONAL AUTHOR RIGHTS AFTER PUBLICATION – SUBSCRIPTION ARTICLES

Final Published Version and Version of Record – Subscription Articles Authors are generally granted back certain rights to make limited use of the Final Published Version of an article published under the subscription model, as expressly set out in the copyright form. For further information, please see the copyright form for the article and the questions and answers below.

- **After the copyright in the article has transferred to IOP Publishing, may I still use the article for teaching?** Yes - upon transfer of copyright, IOP Publishing and/or the copyright owner grants back to authors a number of rights. These include the right to copy the Final Published Version of the article for teaching purposes. Please include citation details and, for online use, a link to the Version of Record.

- **After the copyright in the article has transferred to IOP Publishing, may I still use the article in a thesis or dissertation?** Yes - upon transfer of copyright, IOP Publishing and/or the copyright owner grants back to authors a number of rights. These include the right to include the Final Published Version of the article in research theses or dissertations. Please include citation details and, for online use, a link to the Version of Record.IOP Publishing's permission will be required for commercial use of an article published as part of your thesis.Please note that you may need to obtain separate permission from the copyright owner for any third party content you include within the article.Please also contact IOP Publishing to request permission, at permissions@iop.org (mailto:permissions@iop.org), if you intend to submit your dissertation via ProQuest. IOP Publishing does not allow ProQuest to publish or sell the article as part of your dissertation.

- **After the copyright in the article has transferred to IOP Publishing, may I still use the article for lecturing and/or at conferences?** Yes, you may make oral presentations of the article and, subject to adequate citation, include a summary and/or highlights of it in papers distributed at presentations or in conference proceedings. You may not submit an article which is substantially similar to one published in an IOP Publishing journal for inclusion in conference proceedings.

- **As the author of an article published by IOP Publishing, may I provide a pdf of it to a colleague?** Authors may send the Final Published Version of an article to colleagues on specific request provided no fee is charged and it is not done systematically through, for example, mass-mailings, posting on listservs or other open websites or through Scientific Social Networks.

- **May I post to another publisher's website or commercial third party websites?** You may not post the Accepted Manuscript, Final Published Version or Version of Record to any other publisher website or commercial third party websites.

ADDITIONAL AUTHOR RIGHTS AFTER PUBLICATION – VIDEO ABSTRACTS AND SUPPLEMENTARY MATERIAL/DATA

ELSEVIER LICENSE
TERMS AND CONDITIONS

Apr 19, 2017

This Agreement between Ankur Gupta ("You") and Elsevier ("Elsevier") consists of your license details and the terms and conditions provided by Elsevier and Copyright Clearance Center.

License Number	4092550618105
License date	Apr 19, 2017
Licensed Content Publisher	Elsevier
Licensed Content Publication	Biosensors and Bioelectronics
Licensed Content Title	A nanoceria–platinum–graphene nanocomposite for electrochemical biosensing
Licensed Content Author	P. Chaturvedi,D.C. Vanegas,M. Taguchi,S.L. Burrs,P. Sharma,E.S. McLamore
Licensed Content Date	15 August 2014
Licensed Content Volume	58
Licensed Content Issue	n/a
Licensed Content Pages	7
Start Page	179
End Page	185
Type of Use	reuse in a thesis/dissertation
Portion	figures/tables/illustrations
Number of figures/tables/illustrations	1
Format	both print and electronic
Are you the author of this Elsevier article?	No
Will you be translating?	No
Order reference number	
Original figure numbers	4a
Title of your thesis/dissertation	Redox-Active Solid State Materials and its Biomedical and Biosensing Applications
Expected completion date	May 2017
Estimated size (number of pages)	150
Elsevier VAT number	GB 494 6272 12
Requestor Location	Ankur Gupta 12030 Pasteur Drive Apt #415 ORLANDO, FL 32826 United States Attn: Ankur Gupta
Publisher Tax ID	98-0397604

ROYAL SOCIETY OF CHEMISTRY LICENSE TERMS AND CONDITIONS

Apr 19, 2017

This Agreement between Ankur Gupta ("You") and Royal Society of Chemistry ("Royal Society of Chemistry") consists of your license details and the terms and conditions provided by Royal Society of Chemistry and Copyright Clearance Center.

License Number	4092560017750
License date	Apr 19, 2017
Licensed Content Publisher	Royal Society of Chemistry
Licensed Content Publication	Chemical Communications (Cambridge)
Licensed Content Title	Fluorescence turn-on detection of hypochlorous acid via HOCl-promoted dihydrofluorescein-ether oxidation and its application in vivo
Licensed Content Author	Yi Zhou,Ju-Ying Li,Kai-Hui Chu,Ke Liu,Cheng Yao,Jing-Yun Li
Licensed Content Date	Feb 17, 2012
Licensed Content Volume	48
Licensed Content Issue	39
Type of Use	Thesis/Dissertation
Requestor type	academic/educational
Portion	figures/tables/images
Number of figures/tables/images	1
Format	print and electronic
Distribution quantity	10000
Will you be translating?	no
Order reference number	
Title of the thesis/dissertation	Redox-Active Solid State Materials and its Biomedical and Biosensing Applications
Expected completion date	May 2017
Estimated size	150
Requestor Location	Ankur Gupta 12030 Pasteur Drive Apt #415 ORLANDO, FL 32826 United States Attn: Ankur Gupta
Billing Type	Invoice
Billing Address	Ankur Gupta 12030 Pasteur Drive Apt #415 ORLANDO, FL 32826 United States Attn: Ankur Gupta

ROYAL SOCIETY OF CHEMISTRY LICENSE TERMS AND CONDITIONS

Apr 19, 2017

This Agreement between Ankur Gupta ("You") and Royal Society of Chemistry ("Royal Society of Chemistry") consists of your license details and the terms and conditions provided by Royal Society of Chemistry and Copyright Clearance Center.

License Number	4092560216572
License date	Apr 19, 2017
Licensed Content Publisher	Royal Society of Chemistry
Licensed Content Publication	New Journal of Chemistry
Licensed Content Title	A specific and rapid "on-off" acenaphthenequinone-based probe for HOCl detection and imaging in living cells
Licensed Content Author	Jie Zhao,Hongjuan Li,Kui Yang,Shiguo Sun,Aiping Lu,Yongqian Xu
Licensed Content Date	May 22, 2014
Licensed Content Volume	38
Licensed Content Issue	8
Type of Use	Thesis/Dissertation
Requestor type	academic/educational
Portion	figures/tables/images
Number of figures/tables/images	3
Format	print and electronic
Distribution quantity	10000
Will you be translating?	no
Order reference number	
Title of the thesis/dissertation	Redox-Active Solid State Materials and its Biomedical and Biosensing Applications
Expected completion date	May 2017
Estimated size	150
Requestor Location	Ankur Gupta 12030 Pasteur Drive Apt #415 ORLANDO, FL 32826 United States Attn: Ankur Gupta
Billing Type	Invoice
Billing Address	Ankur Gupta 12030 Pasteur Drive Apt #415 ORLANDO, FL 32826 United States Attn: Ankur Gupta
Total	0.00 USD

Title: Direct Synthesis of Nanoceria in Aqueous Polyhydroxyl Solutions

Author: A. S. Karakoti, Satyanarayana V. N. T. Kuchibhatla, K. Suresh Babu, et al

Publication: The Journal of Physical Chemistry C

Publisher: American Chemical Society

Date: Nov 1, 2007

Logged in as: Ankur Gupta
Account #: 3000276460
LOGOUT

PERMISSION/LICENSE IS GRANTED FOR YOUR ORDER AT NO CHARGE

This type of permission/license, instead of the standard Terms & Conditions, is sent to you because no fee is being charged for your order. Please note the following:

- Permission is granted for your request in both print and electronic formats, and translations.
- If figures and/or tables were requested, they may be adapted or used in part.
- Please print this page for your records and send a copy of it to your publisher/graduate school.
- Appropriate credit for the requested material should be given as follows: "Reprinted (adapted) with permission from (COMPLETE REFERENCE CITATION). Copyright (YEAR) American Chemical Society." Insert appropriate information in place of the capitalized words.
- One-time permission is granted only for the use specified in your request. No additional uses are granted (such as derivative works or other editions). For any other uses, please submit a new request.

If credit is given to another source for the material you requested, permission must be obtained from that source.

BACK CLOSE WINDOW

Title: PEGylated Nanoceria as Radical Scavenger with Tunable Redox Chemistry

Author: Ajay S. Karakoti, Sanjay Singh, Amit Kumar, et al

Publication: Journal of the American Chemical Society

Publisher: American Chemical Society

Date: Oct 1, 2009

Logged in as:
Ankur Gupta
Account #:
3000276460

LOGOUT

PERMISSION/LICENSE IS GRANTED FOR YOUR ORDER AT NO CHARGE

This type of permission/license, instead of the standard Terms & Conditions, is sent to you because no fee is being charged for your order. Please note the following:

- Permission is granted for your request in both print and electronic formats, and translations.
- If figures and/or tables were requested, they may be adapted or used in part.
- Please print this page for your records and send a copy of it to your publisher/graduate school.
- Appropriate credit for the requested material should be given as follows: "Reprinted (adapted) with permission from (COMPLETE REFERENCE CITATION). Copyright (YEAR) American Chemical Society." Insert appropriate information in place of the capitalized words.
- One-time permission is granted only for the use specified in your request. No additional uses are granted (such as derivative works or other editions). For any other uses, please submit a new request.

If credit is given to another source for the material you requested, permission must be obtained from that source.

BACK CLOSE WINDOW

Title:	Nanomedicine	Logged in as: Ankur Gupta
Article ID:	To be determined	Account #: 3000276460
Publication:	Publication1	LOGOUT
Publisher:	CCC Republication	
Date:	Jan 1, 2006	

Order Completed

Thank you for your order.

This Agreement between Ankur Gupta ("You") and Future Medicine Ltd ("Future Medicine Ltd") consists of your order details and the terms and conditions provided by Future Medicine Ltd and Copyright Clearance Center.

License number	Reference confirmation email for license number
License date	Apr, 21 2017
Licensed content publisher	Future Medicine Ltd
Licensed content title	Nanomedicine
Licensed content date	Jan 1, 2006
Type of use	Thesis/Dissertation
Requestor type	Academic institution
Format	Print, Electronic
Portion	chart/graph/table/figure
Number of charts/graphs/tables/figures	1
Title or numeric reference of the portion(s)	Table 2. Catalytic activity and correlation with physiochemical properties.
Title of the article or chapter the portion is from	Cerium oxide nanoparticles: applications and prospects in nanomedicine
Editor of portion(s)	NA
Author of portion(s)	Soumen Das, Janet M Dowding, Kathryn E Klump, James F McGinnis, William Self and Sudipta Seal
Volume of serial or monograph	8
Issue, if republishing an article from a serial	9
Page range of portion	Table 2
Publication date of portion	Feb 1, 2013
Rights for	Main product
Duration of use	Life of current edition
Creation of copies for the disabled	no
With minor editing privileges	yes
For distribution to	Worldwide
In the following language(s)	Original language of publication
With incidental promotional use	no
Lifetime unit quantity of new product	Up to 19,999
Made available in the following markets	Education
Specified additional information	Minor editing previlages
The requesting person/organization	Ankur Gupta
Order reference number	

REFERENCES

[1] G. Bartosz. *Generation of Reactive Oxygen Species in Biological Systems*, Comments on Toxicology 9 (2003) 5-21.

[2] K. Krumova, G. Cosa. *Chapter 1 Overview of Reactive Oxygen Species. Singlet Oxygen: Applications in Biosciences and Nanosciences*, Volume 1, vol. 1. The Royal Society of Chemistry (2016) p1-21.

[3] S. Das, J. Dowding, K. Klump, J. McGinnis, W. Self, S. Seal. *Cerium oxide nanoparticles: applications and prospects in nanomedicine*, Nanomedicine (London, U. K.) 8 (2013) 1483-1508.

[4] J. Dowding, W. Song, K. Bossy, A. Karakoti, A. Kumar, A. Kim, B. Bossy, S. Seal, M. Ellisman, G. Perkins, W. Self, E Bossy-Wetzel. *Cerium oxide nanoparticles protect against Aβ-induced mitochondrial fragmentation and neuronal cell death*, Cell Death & Differentiation 21 (2014) 1622-1632.

[5] S. Hutson. *Experts urge a more measured look at antioxidants*, Nature Medicine 14 (2008) 795-795.

[6] K. Rezai-Zadeh, R.D. Shytle, Y. Bai, J. Tian, H. Hou, T. Mori, J. Zeng, D. Obregon, T. Town, J. Tan. *Flavonoid-mediated presenilin-1 phosphorylation reduces Alzheimer's disease β-amyloid production*, Journal of Cellular and Molecular Medicine 13 (2009) 574-588.

[7] M.J. Stampfer, C.H. Hennekens, J.E. Manson G.A. Colditz, B. Rosner, W.C. Willett. *Vitamin E consumption and the risk of coronary disease in women*, New England Journal of Medicine 328 (1993) 1444-1449.

[8] S. He, W. Shi, X. Zhang, J. Li, Y. Huang. β−*cyclodextrins-based inclusion complexes of* $CoFe_2O_4$ *magnetic nanoparticles as catalyst for the luminol chemiluminescence system and their applications in hydrogen peroxide detection*, Talanta 82 (2010) 377-383.

[9] Q. Xu, K.A. Lee, S. Lee, K.M. Lee, W.J. Lee, J. Yoon. A *highly specific fluorescent probe for hypochlorous acid and its application in imaging microbe-induced HOCl production*, Journal of the American Chemical Society 135 (2013) 9944-9949.

[10] M. Sun, H. Yu, H. Zhu, F. Ma, S. Zhang, D. Huang, S. Wang. *Oxidative cleavage-based near-infrared fluorescent probe for hypochlorous acid detection and myeloperoxidase activity evaluation*, Analytical Chemistry 86 (2014) 671-677.

[11] E. Pick, Y. Keisari. *A simple colorimetric method for the measurement of hydrogen peroxide produced by cells in culture*, Journal of Immunological Methods 38 (1980) 161-170.

[12] Z.S. Wu, S.B. Zhang, M.M. Guo, C.R. Chen, G.L. Shen, R.Q. Yu. *Homogeneous, unmodified gold nanoparticle-based colorimetric assay of hydrogen peroxide*, Analytica Chimica Acta 584 (2007) 122-128.

[13] H. Lu, S. Yu, Y. Fan, C. Yang, D. Xu. *Nonenzymatic hydrogen peroxide electrochemical sensor based on carbon-coated* SnO_2 *supported Pt nanoparticles*, Colloids and Surfaces B: Biointerfaces 101 (2013) 106-110.

[14] Q. He, D. Zheng, S. Hu. *Development and application of a nano-alumina based nitric oxide sensor*, Microchimica Acta 164 (2009) 459-464.

[15] L. Dong, V. Spagnolo, R. Lewicki, F.K. Tittel. *Ppb-level detection of nitric oxide using an external cavity quantum cascade laser based QEPAS sensor*, Optics Express 19 (2011) 24037-24045.

[16] J. Pang, C. Fan, X. Liu, T. Chen, G. Li. *A nitric oxide biosensor based on the multi-assembly of hemoglobin/montmorillonite/polyvinyl alcohol at a pyrolytic graphite electrode*, Biosensors and Bioelectronics 19 (2003) 441-445.

[17] E. Topoglidis, Y. Astuti, F. Duriaux, M. Grätzel, J.R. Durrant. *Direct electrochemistry and nitric oxide interaction of heme proteins adsorbed on nanocrystalline tin oxide electrodes*, Langmuir 19 (2003) 6894-6900.

[18] P. Chaturvedi, D.C. Vanegas, M. Taguchi, S.L. Burrs, P. Sharma, E.S. McLamore. *A nanoceria–platinum–graphene nanocomposite for electrochemical biosensing*, Biosensors and Bioelectronics 58 (2014) 179-185.

[19] S.P. Stewart, S.E.J. Bell, D. McAuley, I. Baird, S.J. Speers, G. Kee. *Determination of hydrogen peroxide concentration using a handheld Raman spectrometer: Detection of an explosives precursor*, Forensic Science International 216 (2012) e5-e8.

[20] D. Srikun, A.E. Albers, C.I. Nam, A.T. Iavarone, C.J. Chang. *Organelle-targetable fluorescent probes for imaging hydrogen peroxide in living cells via SNAP-tag protein labeling*, Journal of the American Chemical Society 132 (2010) 4455-4465.

[21] H. Yin, L. Xu, N.A. Porter. *Free radical lipid peroxidation: mechanisms and analysis*, Chemical Reviews 111 (2011) 5944-5972.

[22] L.I. Leichert, F. Gehrke, H.V. Gudiseva, T. Blackwell, M. Ilbert, A.K. Walker, J.R. Strahler, P.C. Andrews, U. Jakob. *Quantifying changes in the thiol redox proteome upon oxidative stress in vivo*, Proceedings of the National Academy of Sciences USA 105 (2008) 8197-8202.

[23] J. Cadet, T. Douki, D. Gasparutto, J.L. Ravanat. *Oxidative damage to DNA: formation, measurement and biochemical features*, Mutation Research/Fundamental and Molecular Mechanisms of Mutagenesis 531 (2003) 5-23.

[24] Y. Shi, Z. Liu, B. Zhao, Y. Sun, F. Xu, Y. Zhang, Z. Wen, H. Yang, Z. Li. *Carbon nanotube decorated with silver nanoparticles via noncovalent interaction for a novel nonenzymatic sensor towards hydrogen peroxide reduction*, Journal of Electroanalytical Chemistry 656 (2011) 29-33.

[25] X. Deng, F. Wang, Z. Chen. *A novel electrochemical sensor based on nano-structured film electrode for monitoring nitric oxide in living tissues*, Talanta 82 (2010) 1218-1224.

[26] T. Wang, H. Zhu, J. Zhuo, Z. Zhu, P. Papakonstantinou, G. Lubarsky, J. Lin, M. Li. *Biosensor based on ultrasmall MoS_2 nanoparticles for electrochemical detection of H_2O_2 released by cells at the nanomolar level*, Analytical Chemistry 85 (2013) 10289-10295.

[27] K. Fumihiro, U. Minoru, Y. Akifumi. Detection of hypochlorous acid using reduction wave during anodic cyclic voltammetry, Japanese Journal of Applied Physics 44 (2005) L718.

[28] F.J.D. Campo, O. Ordeig, F.J. Muñoz. *Improved free chlorine amperometric sensor chip for drinking water applications*, Analytica Chimica Acta 554 (2005) 98-104.

[29] R. Olivé-Monllau, J. Orozco, C. Fernández-Sánchez, M. Baeza, J. Bartrolí, C. Jimenez-Jorquera, F. Céspedes. *Flow injection analysis system based on amperometric thin-film transducers for free chlorine detection in swimming pool waters*, Talanta 77 (2009) 1739-1744.

[30] Y. Zhou, J.Y. Li, K.H. Chu, K. Liu, C. Yao, J.Y. Li. *Fluorescence turn-on detection of hypochlorous acid via HOCl-promoted dihydrofluorescein-ether oxidation and its application in vivo*, Chemical Communications 48 (2012) 4677-4679.

[31] J. Zhao, H. Li, K. Yang, S. Sun, A. Lu, Y. Xu. *A specific and rapid "on-off" acenaphthenequinone-based probe for HOCl detection and imaging in living cells*, New Journal of Chemistry 38 (2014) 3371-3374.

[32] P. Chaturvedi, D.C. Vanegas, M. Taguchi, S.L. Burrs, P. Sharma, E.S. McLamore. *A nanoceria–platinum–graphene nanocomposite for electrochemical biosensing*, Biosensors and Bioelectronics 58 (2014) 179-185.

[33] A.S. Karakoti, S. Singh, A. Kumar, M. Malinska, S.V.N.T. Kuchibhatla, K. Wozniak, W.T. Self, S. Seal. *PEGylated nanoceria as radical scavenger with tunable redox chemistry*, Journal of the American Chemical Society 131 (2009) 14144-14145.

[34] S. Barkam, S. Das, S. Saraf, R. McCormack, D. Richardson, L. Atencio, V. Moosavifazel, S. Seal. *The change in antioxidant properties of dextran-coated redox active nanoparticles due to synergetic photoreduction–oxidation*, Chemistry-A European Journal 21 (2015) 12646-12656.

[35] B.C. Schanen, S. Das, C.M. Reilly, W.L. Warren, W.T. Self, S. Seal, D.R. Drake. *Immunomodulation and T helper TH_1/TH_2 response polarization by CeO_2 and TiO_2 nanoparticles*, PLoS One 8 (2013) e62816.

[36] A.A. Vernekar, D. Sinha, S. Srivastava, P.U. Paramasivam, P. D'Silva, G. Mugesh. *An antioxidant nanozyme that uncovers the cytoprotective potential of vanadia nanowires*, Nature Communications 5 (2014) 5301.

[37] R.Z. Zand, K. Verbeken, A. Adriaens. *Evaluation of the corrosion inhibition performance of silane coatings filled with cerium salt-activated nanoparticles on hot-dip galvanized steel substrates*, International Journal of Electrochemical Science 8 (2013) 4924-4940.

[38] T.X. Sayle, M. Cantoni, U.M. Bhatta, S.C. Parker, S.R. Hall, G. Möbus, M. Molinari, D. Reid, S. Seal, D.C. Sayle. *Strain and architecture-tuned reactivity in ceria nanostructures; enhanced catalytic oxidation of CO to CO_2*, Chemistry of Materials 24 (2012) 1811-1821.

[39] A. Karakoti, J. King, A. Vincent, S. Seal. *Synthesis dependent core level binding energy shift in the oxidation state of platinum coated on ceria–titania and its effect on catalytic decomposition of methanol*, Applied Catalysis A: general 388 (2010) 262-271.

[40] N. Mahato, A. Banerjee, A. Gupta, S. Omar, K. Balani. progress in material selection for solid oxide fuel cell technology: a review, Progress in Materials Science 72 (2015) 141-337.

[41] I. Shitanda, S. Mori, M. Itagaki. *Screen-printed dissolved oxygen sensor based on cerium oxide-supported silver catalyst and polydimethylsiloxane film*, Analytical Science 27 (2011) 1049-1052.

[42] N. Izu, W. Shin, I. Matsubara, N. Murayama. *Kinetic behavior of resistive oxygen sensor using cerium oxide*, Sensors and Actuators B: Chemical 100 (2004) 411-416.

[43] J.M. Dowding, S. Das, A. Kumar, T. Dosani, R. McCormack, A. Gupta, T.X.T. Sayle, D.C. Sayle, L.v. Kalm, S. Seal, W.T. Self. *Cellular interaction and toxicity depend on physicochemical properties and surface modification of redox-active nanomaterials*, ACS Nano 7 (2013) 4855–4868.

[44] A. Gupta, S. Das, S. Seal. *Redox-active nanoparticles in combating neurodegeneration*, Nanomedicine (London, U. K.) 9 (2014) 2725-2728.

[45] L. Alili, M. Sack, A. Karakoti, S. Teuber, K. Puschmann, S. Hirst, C. Reilly, K. Zanger, W. Stahl, S. Das, S. Seal, P. Brenneisen. *Combined cytotoxic and anti-invasive properties of redox-active nanoparticles in tumor–stroma interactions*, Biomaterials 32 (2011) 2918-2929.

[46] C. Xu, Z. Liu, L. Wu, J. Ren, X. Qu. *Nucleoside triphosphates as promoters to enhance nanoceria enzyme-like activity and for single-nucleotide polymorphism typing*, Advanced Functional Materials 24 (2014) 1624-1630.

[47] C. Xu, X. Qu. Cerium oxide nanoparticle: a remarkably versatile rare earth nanomaterial for biological applications, NPG Asia Materials 6 (2014) e90.

[48] H.J. Kwon, M.Y. Cha, D. Kim, D.K. Kim, M. Soh, K. Shin, T. Hyeon, I. Mook-Jung. *Mitochondria-targeting ceria nanoparticles as antioxidants for alzheimer's disease*, ACS Nano 10 (2016) 2860-2870.

[49] S.S. Lee, W. Song, M. Cho, H.L. Puppala, P. Nguyen, H. Zhu, L. Segatori, V.L. Colvin. *Antioxidant Properties of cerium oxide nanocrystals as a function of nanocrystal diameter and surface coating*, ACS Nano 7 (2013) 9693-9703.

[50] A.S. Karakoti, S. Das, S. Thevuthasan, S. Seal. *PEGylated inorganic nanoparticles*, Angewandte Chemie International Edition 50 (2011) 1980-1994.

[51] A. Gupta, S. Das, B. Schanen, S. Seal. *Adjuvants in micro- to nanoscale: current state and future direction*, Wiley Interdisciplinary Reviews: Nanomedicine and Nanobiotechnology 8 (2016) 61-84.

[52] A.B. Sifontes, G. Gonzalez, J.L. Ochoa, L.M. Tovar, T. Zoltan, E. Cañizales. *Chitosan as template for the synthesis of ceria nanoparticles*, Materials Research Bulletin 46 (2011) 1794-1799.

[53] E.E. Connor, J. Mwamuka, A. Gole, C.J. Murphy, M.D. Wyatt. Gold nanoparticles are taken up by human cells but do not cause acute cytotoxicity, Small 1 (2005) 325-327.

[54] S.H. Brewer, W.R. Glomm, M.C. Johnson, M.K. Knag, S. Franzen. *Probing BSA binding to citrate-coated gold nanoparticles and surfaces*, Langmuir 21 (2005) 9303-9307.

[55] R.J. Murdock, S.A. Putnam, S. Das, A. Gupta, E.D.Z. Chase, S. Seal. *High-throughput, protein-targeted biomolecular detection using frequency-domain faraday rotation spectroscopy*, Small 13 (2017) 1602862.

[56] C.J. Neal, S. Das, S. Saraf, L. Tetard, S. Seal. *Self-assembly of peg-coated ceria nanoparticles shows dependence on PEG molecular weight and ageing*, ChemPlusChem 80 (2015) 1680-1690.

[57] S. Saraf, C.J. Neal, S. Das, S. Barkam, R. McCormack, S. Seal. *Understanding the adsorption interface of polyelectrolyte coating on redox active nanoparticles using soft particle electrokinetics and its biological activity*, ACS Applied Materials & Interfaces 6 (2014) 5472-5482.

[58] A.S. Karakoti, S.V.N.T. Kuchibhatla, K.S. Babu, S. Seal. *Direct synthesis of nanoceria in aqueous polyhydroxyl solutions*, The Journal of Physical Chemistry C 111 (2007) 17232-17240.

[59] C. Korsvik, S. Patil, S. Seal, W.T. Self. *Superoxide dismutase mimetic properties exhibited by vacancy engineered ceria nanoparticles*, Chemical Communications (2007) 1056-1058.

[60] J.M. Dowding, T. Dosani, A. Kumar, S. Seal, W.T. Self. *Cerium oxide nanoparticles scavenge nitric oxide radical (*NO)*, Chemical Communications 48 (2012) 4896-4898.

[61] L. Alili, M. Sack, C. von Montfort, S. Giri, S. Das, K.S. Carroll, K. Zanger, S. Seal, P. Brenneisen. *Downregulation of tumor growth and invasion by redox-active nanoparticles*, Antioxidants & Redox Signaling 19 (2013) 765-778.

[62] J. Colon, L. Herrera, J. Smith, S. Patil, C. Komanski, P. Kupelian, S. Seal, D.W. Jenkins, C.H. Baker. *Protection from radiation-induced pneumonitis using cerium oxide nanoparticles*, Nanomedicine: Nanotechnology. Biology and Medicine 5 (2009) 225-231.

[63] J. Dowding, T. Dosani, A. Kumar, S. Seal, W. Self. *Cerium oxide nanoparticles scavenge nitric oxide radical (˙NO)*, Chemical Communications 48 (2012) 4896-4898.

[64] C. Korsvik, S. Patil, S. Seal, W. Self. *Superoxide dismutase mimetic properties exhibited by vacancy engineered ceria nanoparticles*, Chemical Communications (2007) 1056-1058.

[65] J. Chen, S. Patil, S. Seal, J. McGinnis. Rare earth nanoparticles prevent retinal degeneration induced by intracellular peroxides, Nature Nanotechnology 1 (2006) 142-150.

[66] K.L. Heckman, W. DeCoteau, A. Estevez, K.J. Reed, W. Costanzo, D. Sanford, J.C. Leiter, J. Clauss, K. Knapp, C. Gomez, P. Mullen, E. Rathbun, K. Prime, J. Marini, J. Patchefsky, A.S. Patchefsky, R.K. Hailstone, J.S. Erlichman. *Custom cerium oxide nanoparticles protect against a free radical mediated autoimmune degenerative disease in the brain*, ACS Nano 7 (2013) 10582–10596.

[67] C.K. Kim, T. Kim, I.Y. Choi, M. Soh, D. Kim, Y.J. Kim, H. Jang, H.S. Yang, J.Y. Kim, H.K. Park, S.P. Park, S. Park, T. Yu, BW. Yoon, S.H. Lee, T. Hyeon. *Ceria Nanoparticles that can Protect against Ischemic Stroke*, Angewandte Chemie International Edition 51 (2012) 11039 –11043.

[68] A. Kumar, R. Devanathan, V. Shutthanandan, S.V.N.T. Kuchibhatla, A.S. Karakoti, Y. Yong, S. Thevuthasan, S. Seal. *Radiation-induced reduction of ceria in single and polycrystalline thin films*, Journal of Physical Chemistry C 116 (2012) 361-366.

[69] A. Kumar, S. Babu, A.S. Karakoti, A. Schulte, S. Seal. *luminescence properties of europium-doped cerium oxide nanoparticles: role of vacancy and oxidation states*, Langmuir 25 (2009) 10998-11007.

[70] S. Babu, R. Thanneeru, T. Inerbaev, R. Day, A.E. Masunov, A. Schulte, S. Seal. *Dopant-mediated oxygen vacancy tuning in ceria nanoparticles*, Nanotechnology 20 (2009) 085713.

[71] S. Babu, J.-H. Cho, J.M. Dowding, E. Heckert, C. Komanski, S. Das, J. Colon, C.H. Baker, M. Bass, W.T. Self, S. Seal. *Multicolored redox active upconverter cerium oxide nanoparticle for bio-imaging and therapeutics*, Chemical Communications 46 (2010) 6915–6917.

[72] S. Babu, A. Schulte, S. Seal. *Defects and symmetry influence on visible emission of Eu doped nanoceria*, Applied Physics Letters 92 (2008) 123112.

[73] J.-H. Cho, M. Bass, S. Babu, J.M. Dowding, W. Self, S. Seal. *Up conversion luminescence of Yb^{3+}–Er^{3+} codoped CeO_2 nanocrystals with imaging applications*, Journal of Luminescence 132 (2012) 743–749.

[74] S. Das, S. Singh, V. Singh, D. Joung, J.M. Dowding, D. Reid, J. Anderson, L. Zhai, S.I. Khondaker, W.T. Self, S. Seal. Oxygenated *functional group density on graphene oxide: its effect on cell toxicity*, Partical & Particle Systems Characterizations 30 (2013) 148-157.

[75] D. Eder, M. Motta, A.H. Windle. *Iron-doped Pt–TiO_2 nanotubes for photo-catalytic water splitting*, Nanotechnology 20 (2009) 055602.

[76] O.I. Lebedev, R. Erni, G.V. Tendeloo. *Structure and composition of dilute Co-doped BaTiO3 nanoparticles* in: Richter S, Schwedt A, (Eds.). EMC 2008 14th European Microscopy Congress, vol. 2. Springer, Aachen, Germany (2008) p231-232.

[77] C.P. Liu, C.B. Boothroyd, C.J. Humphreys. *Energy-filtered transmission electron microscopy of multilayers in semiconductors*, Journal of Microscopy 194 (1999) 58-70.

[78] S.Y. Kuo, W.C. Chen, F.I. Lai, C.P. Cheng, H.C. Kuo, S.C. Wang, W.F. Hsieh. *Effects of doping concentration and annealing temperature on properties of highly-oriented Al-doped ZnO films*, Journal of Crystal Growth 287 (2006) 78-84.

[79] M. Werner, H. Mehrer, H.D. Hochheimer. *Effect of hydrostatic pressure, temperature, and doping on self-diffusion in germanium*, Physical Review B: Condens Matter Materials Physics 32 (1985) 3930-3937.

[80] S. Deshpande, S. Patil, S.V. Kuchibhatla, S. Seal. *Size dependency variation in lattice parameter and valency states in nanocrystalline cerium oxide*, Applied Physics Letters 87 (2005) 133113.

[81] R.K. Samal, S.C. Satrusallya, P.K. Sahoo, S.S. Ray, S.N. Nayak. *Reaction of water soluble polymers with oxidising agents: reaction of dextran with tetravalent cerium*, Colloid and Polymer Science 262 (1984) 939-947.

[82] N. Shehata, K. Meehan, M. Hudait, N. Jain, S. Gaballah. *Study of optical and structural characteristics of ceria nanoparticles doped with negative and positive association lanthanide elements*, Journal of Nanomaterials 2014 (2014) 401498.

[83] D. Andersson, S. Simak, N. Skorodumova, I. Abrikosov, B. Johansson. *Optimization of ionic conductivity in doped ceria*, Proceedings of the National Academy of Sciences USA 103 (2006) 3518–3352.

[84] X. Wei, W. Pan, L. Cheng, B. Li. *Atomistic calculation of association energy in doped ceria*, Solid State Ionics 180 (2009) 13-17.

[85] A.R. Asati. *Synthesis of biocompatible antioxidant polymer coated cerium dioxide nanoparticles, its oxidase like behavior and cellular uptake studies*. Chemistry, PhD Thesis. University of Central Florida (2009) 81 Orlando, FL USA.

[86] B. D'Angelo, S. Santucci, E. Benedetti, S.D. Loreto, R.A. Phani, S. Falone, F. Amicarelli, M.P. Ceru, A. Cimini. *Cerium Oxide Nanoparticles Trigger Neuronal Survival in a Human Alzheimer Disease Model by Modulating BDNF Pathway*, Current Nanoscience 5 (2009) 167-176.

[87] P.F. Wahid, K.B. Sundaram, P.J. Sisk. *Cerium dioxide thin film optical waveguides*, Optics & Laser Technology 24 (1992) 263-266.

[88] J. Qiao, C.Y. Yang. *High-Tc superconductors on buffered silicon: materials properties and device applications*, Materials Science and Engineering: R: Reports 14 (1995) 157-201.

[89] F. Wang, R. Wördenweber. *Large-area epitaxial CeO_2 buffer layers on sapphire substrates for the growth of high quality $YBa_2Cu_3O_7$ films*, Thin Solid Films 227 (1993) 200-204.

[90] W.H. Kim, M.K. Kim, W.J. Maeng, J. Gatineau, V. Pallem, C. Dussarrat, A. Noori, D. Thompson, S. Chu, H. Kim. *Growth characteristics and film properties of cerium dioxide prepared by plasma-enhanced atomic layer deposition*, Journal of The Electrochemical Society 158 (2011) G169-G172.

[91] C.H. Chen, I.Y.-K. Chang, J.Y.-M. Lee, F.C. Chiu. *Electrical characterization of CeO2/Si interface properties of metal-oxide-semiconductor field-effect transistors with CeO_2 gate dielectric*, Applied Physics Letters 92 (2008) 043507.

[92] S. Guo, H. Arwin, S.N. Jacobsen, K. Järrendahl, U. Helmersson. *A spectroscopic ellipsometry study of cerium dioxide thin films grown on sapphire by rf magnetron sputtering*, Journal of Applied Physics 77 (1995) 5369-5376.

[93] R.R. Essex, J.I. Ressero, G.M. Jursich, C.G. Takoudis. *Atomic layer deposition of cerium oxide for potential use in solid oxide fuel cells*, Journal of Undergraduate Research 6 (2013) 37-41.

[94] J. Paivasaari, M. Putkonen, L. Niinisto. *Cerium dioxide buffer layers at low temperature by atomic layer deposition*, Journal of Materials Chemistry 12 (2002) 1828-1832.

[95] L. Kim, J. Kim, D. Jung, C.Y. Park, C.W. Yang, Y. Roh. *Effects of deposition parameters on the crystallinity of CeO_2 thin films deposited on Si(100) substrates by R.F.-magnetron sputtering*, Thin Solid Films 360 (2000) 154-158.

[96] N.P. Sardesai, D. Andreescu, S. Andreescu. *Electroanalytical evaluation of antioxidant activity of cerium oxide nanoparticles by nanoparticle collisions at microelectrodes*, Journal of the American Chemical Society 135 (2013) 16770-16773.

[97] C.J. Neal, A. Gupta, S. Barkam, S. Saraf, S. Das, H.J. Cho, S. Seal. *Picomolar detection of hydrogen peroxide using enzyme-free inorganic nanoparticle-based sensor*, Scientific Reports (2017) *Accepted manuscript*.

[98] A. Gupta, S. Das, C.J. Neal, S. Seal. *Controlling the surface chemistry of cerium oxide nanoparticles for biological applications*, Journal of Materials Chemistry B 4 (2016) 3195-3202.

[99] J.M. Dowding, S. Seal, W.T. Self. *Cerium oxide nanoparticles accelerate the decay of peroxynitrite ($ONOO^-$)*, Drug Delivery and Translational Research 3 (2013) 375-379.

[100] A. Gupta, S. Das, S. Seal. *Redox-active nanoparticles in combating neurodegeneration*, Nanomedicine 9 (2014) 2725-2728.

[101] J. Chen, S. Patil, S. Seal, J.F. McGinnis. *Rare earth nanoparticles prevent retinal degeneration induced by intracellular peroxides*, Nature Nanotechnology 1 (2006) 142-150.

[102] S. Wu, Z. Zeng, Q. He, Z. Wang, S.J. Wang, Y. Du, Z. Yin, X. Sun, W. Chen, H. Zhang. *Electrochemically reduced single-layer MoS_2 nanosheets: characterization, properties, and sensing applications*, Small 8 (2012) 2264-2270.

[103] A. Gupta, T. Sakthivel, S. Seal. *Recent development in 2D materials beyond graphene*, Progress in Materials Science 73 (2015) 44-126.

[104] K. Kalantar-zadeh, J.Z. Ou. *Biosensors based on two-dimensional MoS_2*, ACS Sensors 1 (2016) 5-16.

[105] D. Sarkar, W. Liu, X. Xie, A.C. Anselmo, S. Mitragotri, K. Banerjee. *MoS_2 field-effect transistor for next-generation label-free biosensors*, ACS Nano 8 (2014) 3992-4003.

[106] J. Lee, P. Dak, Y. Lee, H. Park, W. Choi, M.A. Alam, S. Kim. *Two-dimensional layered MoS_2 biosensors enable highly sensitive detection of biomolecules*, Scientific Reports 4 (2014) 7352.

[107] D.W. Lee, J. Lee, I.Y. Sohn, B.Y. Kim, Y.M. Son, H. Bark, J. Jung, M. Choi, T.H. Kim, C. Lee, N.E. Lee. *Field-effect transistor with a chemically synthesized mos2 sensing channel for label-free and highly sensitive electrical detection of DNA hybridization*, Nano Research 8 (2015) 2340-2350.

[108] A.H. Loo, A. Bonanni, Z. Sofer, M. Pumera. *Transitional metal/chalcogen dependant interactions of hairpin DNA with transition metal dichalcogenides, MX_2*, ChemPhysChem 16 (2015) 2304-2306.

[109] A.H. Loo, A. Bonanni, A. Ambrosi, M. Pumera. *Molybdenum disulfide (MoS_2) nanoflakes as inherently electroactive labels for DNA hybridization detection*, Nanoscale 6 (2014) 11971-11975.

[110] H.L. Shuai, K.J. Huang, Y.X. Chen, L.X. Fang, M.P. Jia. *Au nanoparticles/hollow molybdenum disulfide microcubes based biosensor for microRNA-21 detection coupled*

with duplex-specific nuclease and enzyme signal amplification, Biosensors and Bioelectronics 89, Part 2 (2017) 989-997.

[111] K.J. Huang, L. Wang, J.Z. Zhang, L.L. Wang, Y.P. Mo. *One-step preparation of layered molybdenum disulfide/multi-walled carbon nanotube composites for enhanced performance supercapacitor*, Energy 67 (2014) 234-240.

[112] X. Liu, J.Z. Zhang, K.J. Huang, P. Hao. *Net-like molybdenum selenide–acetylene black supported on Ni foam for high-performance supercapacitor electrodes and hydrogen evolution reaction*, Chemical Engineering Journal 302 (2016) 437-445.

[113] S. Jain, A. Sharma, B. Basu. *Vertical electric field stimulated neural cell functionality on porous amorphous carbon electrodes*, Biomaterials 34 (2013) 9252-9263.

[114] S. Jain, A. Sharma, B. Basu. *Vertical electric field induced bacterial growth inactivation on amorphous carbon electrodes*, Carbon 81 (2015) 193–202.

[115] J.N. Coleman, M. Lotya, A. O'Neill, S.D. Bergin, P.J. King, U. Khan, K. Young, A. Gaucher, S. De, R.J. Smith, I.V. Shvets, S.K. Arora, G. Stanton, H.Y. Kim, K. Lee, G.T. Kim, G.S. Duesberg, T. Hallam, J.J. Boland, J.J. Wang, J.F. Donegan, J.C. Grunlan, G. Moriarty, A. Shmeliov, R.J. Nicholls, J.M. Perkins, E.M. Grieveson, K. Theuwissen, D.W. McComb, P.D. Nellist, V. Nicolosi. *Two-dimensional nanosheets produced by liquid exfoliation of layered materials*, Science 331 (2011) 568-571.

[116] G. Kresse, J. Furthmüller. *Efficiency of ab-initio total energy calculations for metals and semiconductors using a plane-wave basis set*, Computational Materials Science 6 (1996) 15-50.

[117] G. Kresse, J. Hafner. *Ab initio molecular dynamics for liquid metals*, Physical Review B 47 (1993) 558-561.

[118] P.E. Blöchl. *Projector augmented-wave method*, Physical Review B 50 (1994) 17953-17979.

[119] G. Kresse, D. Joubert. *From ultrasoft pseudopotentials to the projector augmented-wave method*, Physical Review B 59 (1999) 1758-1775.

[120] J.P. Perdew, K. Burke, M. Ernzerhof. *Generalized Gradient Approximation Made Simple*, Physical Review Letters 77 (1996) 3865-3868.

[121] S. Grimme, J. Antony, S. Ehrlich, H. Krieg. *A consistent and accurate ab initio parametrization of density functional dispersion correction (DFT-D) for the 94 elements H-Pu*, The Journal of Chemical Physics 132 (2010) 154104.

[122] T. Böker, R. Severin, A. Müller, C. Janowitz, R. Manzke, D. Voß, P. Krüger, A. Mazur, J. Pollmann. *Band structure of MoS_2, $MoSe_2$, alpha-$MoTe_2$: Angle-resolved photoelectron spectroscopy and ab initio calculations*, Physical Review B 64 (2001) 235305.

[123] W.H. Press, S.A. Teukolsky, W.T. Vetterling, B.P. Flannery. *Numerical Recipes* Cambridge University Press: New York (2007).

[124] E. Polak. *Computational Methods in Optimization*, Academic Press: New York (1971).

[125] P.K. Chu, L. Li. *Characterization of amorphous and nanocrystalline carbon films*, Materials Chemistry and Physics 96 (2006) 253-277.

[126] T.H. Ko, C.Y. Chen. *Raman spectroscopic study of the microstructure of carbon films developed from cobalt chloride-modified polyacrylonitrile*, Journal of Applied Polymer Science 71 (1999) 2219-2225.

[127] A. Sadezky, H. Muckenhuber, H. Grothe, R. Niessner, U. Pöschl. *Raman microspectroscopy of soot and related carbonaceous materials: Spectral analysis and structural information*, Carbon 43 (2005) 1731-1742.

[128] S. Jain, A. Sharma, B. Basu. *In vitro cytocompatibility assessment of amorphous carbon structures using neuroblastoma and Schwann cells*, Journal of Biomedical Materials Research B: Applied Biomaterials 101 (2013) 520-531.

[129] M.S.A. Rahaman, A.F. Ismail, A. Mustafa. *A review of heat treatment on polyacrylonitrile fiber*, Polymer Degradation and Stability 92 (2007) 1421-1432.

[130] S.C. Das, A. Majumdar, R. Hippler. *Electronic and chemical property of amorphous carbon, hydrocarbon, hydrogenated / hydrogen free carbon nitride: spectroscopic study*, International Journal of Innovation and Scientific Research 12 (2014) 148-156.

[131] G. Ilangovan, K.C. Pillai. *Electrochemical and XPS characterization of glassy carbon electrode surface effects on the preparation of a monomeric molybdate(vi)-modified electrode*, Langmuir 13 (1997) 566-575.

[132] V. Penmatsa, H. Kawarada, Y. Song, C. Wang. *Comparison of different oxidation techniques for biofunctionalization of pyrolyzed carbon*, Material Science Research India 11 (2014) 1-8.

[133] H. Li, Q. Zhang, C.C.R. Yap, B.K. Tay, T.H.T. Edwin, A. Olivier, D. Baillargeat. *From bulk to monolayer mos$_2$: evolution of raman scattering*, Advanced Functional Materials 22 (2012) 1385-1390.

[134] C. Lee, H. Yan, L.E. Brus, T.F. Heinz, J. Hone, S. Ryu. *Anomalous lattice vibrations of single- and few-layer MoS_2*, ACS Nano 4 (2010) 2695-2700.

[135] H. Hou, L. Li, Y. Cho, P.d. Figueiredo, A. Han. *Microfabricated microbial fuel cell arrays reveal electrochemically active microbes*, PLoS ONE 4 (2009) e6570.

[136] T. Wang, L. Liu, Z. Zhu, P. Papakonstantinou, J. Hu, H. Liu, M. Li. *Enhanced electrocatalytic activity for hydrogen evolution reaction from self-assembled monodispersed molybdenum sulfide nanoparticles on an Au electrode*, Energy & Environmental Science 6 (2013) 625-633.

[137] Y. Li, H. Wang, L. Xie, Y. Liang, G. Hong, H. Dai. *MoS_2 nanoparticles grown on graphene: an advanced catalyst for the hydrogen evolution reaction*, Journal of the American Chemical Society 133 (2011) 7296-7299.

[138] A.A. Karyakin, E.E. Karyakina. *Prussian blue-based `artificial peroxidase' as a transducer for hydrogen peroxide detection. application to biosensors*, Sensors and Actuators B: Chemical 57 (1999) 268-273.

[139] S.A.G. Evans, J.M. Elliott, L.M. Andrews, P.N. Bartlett, P.J. Doyle, G. Denuault. *Detection of hydrogen peroxide at mesoporous platinum microelectrodes*, Analytical Chemistry 74 (2002) 1322-1326.

[140] M.W. Shao, Y.Y. Shan, N.B. Wong, S.T. Lee. *Silicon nanowire sensors for bioanalytical applications: glucose and hydrogen peroxide detection*, Advanced Functional Materials 15 (2005) 1478-1482.

[141] L. Campanella, L. Persi, M. Tomassetti. *A new tool for superoxide and nitric oxide radicals determination using suitable enzymatic sensors*, Sensors and Actuators B 68 (2000) 351-359.

[142] X. Zhang, L. Cardosa, M. Broderick, H. Fein, I.R. Davies. Novel calibration method for nitric oxide microsensors by stoichiometrical generation of nitric oxide from SNAP, Electroanalysis 12 (2000) 425-428.

[143] H. Wang, Y. Li, Y. Chen, L. Li, T. Fang, Z. Tang. *Development of a conjugated polymer-based fluorescent probe for selective detection of HOCl*, Journal of Materials Chemistry C 3 (2015) 5136-5140.

[144] Z. Zhang, Y. Zheng, W. Hang, X. Yan, Y. Zhao. *Sensitive and selective off–on rhodamine hydrazide fluorescent chemosensor for hypochlorous acid detection and bioimaging*, Talanta 85 (2011) 779-786.

[145] A.A. Abdelwahab, W.C.A. Koh, H.B. Noh, Y.B. Shim. *A selective nitric oxide nanocomposite biosensor based on direct electron transfer of microperoxidase: Removal of interferences by co-immobilized enzymes*, Biosensors and Bioelectronics 26 (2010) 1080-1086.

[146] Y.A. Bakhirkin, A.A. Kosterev, R.F. Curl, F.K. Tittel, D.A. Yarekha, L. Hvozdara, M. Giovannini, J. Faist. *Sub-ppbv nitric oxide concentration measurements using cw thermoelectrically cooled quantum cascade laser-based integrated cavity output spectroscopy*, Applied Physics B 82 (2006) 149-154.

[147] S. Amemori, M. Matsusaki, M. Akashi. Biocompatible *and highly sensitive nitric oxide sensor particles prepared by layer-by-layer asse*mbly, Chemistry Letters 39 (2010) 42-43.

[148] Y. Wang, S. Hu. *Fluorinated xerogel-derived microelectrodes for amperometric nitric oxide sensing*, Bioelectrochemistry 74 (2009) 301-305.

[149] J.H. Shin, B.J. Privett, J.M. Kita, R.M. Wightman, M.H. Schoenfisch. *Fluorinated Xerogel-Derived Microelectrodes for Amperometric Nitric Oxide Sensing*, Analytical Chemistry 80 (2008) 6850-6859.

[150] C.M. Li, J. Zang, D. Zhan, W. Chen, C.Q. Sun, A.L. Teo, Y.T. Chua, V.S. Lee, S.M. Moochhala. *Electrochemical detection of nitric oxide on a SWCNT/RTIL composite gel microelectrode*, Electroanalysis 18 (2006) 713-718.

[151] C. Fan, X. Liu, J. Pang, G. Li, H. Scheer. *Highly sensitive voltammetric biosensor for nitric oxide based on its high affinity with hemoglobin*, Analytica Chimica Acta 523 (2004) 225-228.

[152] C.X. Guo, S.R. Ng, S.Y. Khoo, X. Zheng, P. Chen, C.M. Li. *RGD-peptide functionalized graphene biomimetic live-cell sensor for real-time detection of nitric oxide molecules*, ACS Nano 6 (2012) 6944-6951.

[153] F.H. Wu, G.C. Zhao, X.W. Wei. *Electrocatalytic oxidation of nitric oxide at multi-walled carbon nanotubes modified electrode*, Electrochemistry Communications 4 (2002) 690-694.

[154] Y.L. Huang, Y. Chen, W. Zhang, S.Y. Quek, C.H. Chen, L.J. Li, W.T. Hsu, W.H. Chang, Y.J. Zheng, W. Chen, A.T.S. Wee. *Bandgap tunability at single-layer molybdenum disulphide grain boundaries*, Nature Communications 6 (2015) 6298.

[155] A.V. Krivosheeva, V.L. Shaposhnikov, V.E. Borisenko, J.L. Lazzari, C. Waileong, J. Gusakova, B.K. Tay. *Theoretical study of defect impact on two-dimensional MoS_2*, Journal of Semiconductors 36 (2015) 122002.

[156] H.-P. Komsa, A.V. Krasheninnikov. *Native defects in bulk and monolayer MoS_2 from first principles*, Physical Review B 91 (2015) 125304.

[157] M.R. Islam, N. Kang, U. Bhanu, H.P. Paudel, M. Erementchouk, L. Tetard, M.N. Leuenberger, S.I. Khondaker. *Tuning the electrical property via defect engineering of single layer MoS_2 by oxygen plasma*, Nanoscale 6 (2014) 10033-10039.

[158] W.M. Parkin, A. Balan, L. Liang, P.M. Das, M. Lamparski, C.H. Naylor, J.A. Rodríguez-Manzo, A.T.C. Johnson, V. Meunier, M. Drndic. *Raman shifts in electron-irradiated monolayer MoS_2*, ACS Nano 10 (2016) 4134-4142.

[159] Z. Lin, B.R. Carvalho, E. Kahn, R. Lv, R. Rao, H. Terrones, M.A. Pimenta, M. Terrones. *Defect engineering of two-dimensional transition metal dichalcogenides*, 2D Materials 3 (2016) 022002.

[160] D. Wu, X. Li, L. Luan, X. Wu, W. Li, M.N. Yogeesh, R. Ghosh, Z. Chu, D. Akinwandeb, Q. Niu, K. Lai. *Uncovering edge states and electrical inhomogeneity in MoS2 field-effect transistors*, Proceedings of the National Academy of Sciences USA 113 (2016) 8583-8588.

[161] Z. Yu, Y. Pan, Y. Shen, Z. Wang, Z.-Y. Ong, T. Xu, R. Xin, L. Pan, B. Wang, L. Sun, J. Wang, G. Zhang, Y.W. Zhang, Y. Shi, X. Wang. *Towards intrinsic charge transport in monolayer molybdenum disulfide by defect and interface engineering*, Nature Communications 5 (2014) 5290.

[162] D. Gopalakrishnan, D. Damien, B. Li, H. Gullappalli, V.K. Pillai, P.M. Ajayan, M.M. Shaijumon. *Electrochemical synthesis of luminescent MoS_2 quantum dots*, Chemical Communications 51 (2015) 6293-6296.

[163] M.V. Bollinger, K.W. Jacobsen, J.K. Nørskov. *Atomic and electronic structure of MoS_2 nanoparticles*, Physical Review B 67 (2003) 085410.

[164] T. Li, G. Galli. *Electronic properties of MoS_2 nanoparticle*, Journal of Physical Chemistry C 111 (2007) 16192-16196.

[165] X. Li, L. Zhang, X. Zang, X. Li, H. Zhu. *Photo-promoted platinum nanoparticles decorated MoS_2@Graphene woven fabric catalyst for efficient hydrogen generation*, ACS Applied Materials & Interfaces 8 (2016) 10866-10873.

[166] G. Zhang, H. Liu, J. Qu, J. Li. *Two-dimensional layered MoS_2: rational design, properties and electrochemical applications*, Energy & Environmental Science 9 (2016) 1190-1209.

[167] D. Le, T.B. Rawal, T.S. Rahman. *Single-layer MoS_2 with sulfur vacancies: structure and catalytic application*, Journal of Physical Chemistry C 118 (2014) 5346-5351.

[168] W.K. Burton, N. Cabrera, F.C. Frank. *The growth of crystals and the equilibrium structure of their surfaces*, Philosophical Transactions of the Royal Society London A: Mathematical, Physical and Engineering Sciences 243 (1951) 299-358.

[169] J.V. Lauritsen, M.V. Bollinger, E. Laegsgaard, K.W. Jacobsen, J.K. Norskov, B.S. Clausen, H. Topsoe, F. Besenbacher. *Atomic-scale insight into structure and morphology changes of MoS_2 nanoclusters in hydrotreating catalysts*, Journal of Catalysis 221 (2004) 510-522.

[170] H.I. Karunadasa, E. Montalvo, Y. Sun, M. Majda, J.R. Long, C.J. Chang. *A molecular MoS_2 edge site mimic for catalytic hydrogen generation*, Science 335 (2012) 698-702.

[171] K.K. Ghuman, S. Yadav, C.V. Singh. *Adsorption and dissociation of H_2O on monolayerd MoS_2 edges: energetics and mechanism from ab initio siulations*, Journal of Physical Chemistry. C 119 (2015) 6518-6529.

[172] J. Kibsgaard, Z. Chen, B.N. Reinecke, T.F. Jaramillo. *Engineering the surface structure of MoS_2 to preferentially active edge sites for electrocatalysis*, Nature Materials 11 (2012) 963-969.

[173] N. Kumar, J.M. Seminario. *Computational chemistry analysis of hydrodesulfurization reactions catalyzed by molybdenum disulfide nanoparticles*, Journal of Physical Chemistry C119 (2015) 29157-29170.

[174] J. Kibsgaard, J.V. Lauritsen, E. Lægsgaard, B.S. Clausen, H. Topsøe, F. Besenbacher. *Cluster−support interactions and morphology of MoS_2 nanoclusters in a graphite-supported hydrotreating model catalyst*, Journal of the American Chemical Society 128 (2006) 13950-13958.